Parameterized Energy Efficiency Models in Grinding Machine Tools

By

IAN CLAY GARRETSON

DISSERTATION

Submitted in partial satisfaction of the requirements for the degree of

DOCTOR OF PHILOSOPHY

in

Mechanical And Aerospace Engineering

in the

OFFICE OF GRADUATE STUDIES

of the

UNIVERSITY OF CALIFORNIA

DAVIS

Approved:

_____

Barbara S. Linke, Chair

_____

Soshi Masakazu

_____

Rida T. Farouki

Committee in Charge

2021

Abstract

Industrial energy consumption accounts for 35% of all energy consumed in the United States and energy consumed by machine tools in manufacturing processes contributes a significant portion to the inefficiencies in manufacturing energy consumption. However, there are only few energy efficiency models for machine tools which also include product quality. Therefore, this research investigates the hypothesis that physics-based models of machine tools and processes lead to more energy-efficient machine tool design. Furthermore, the research will focus on abrasive machining, primarily using grinding machines and will highlight the quality aspects of finished workpieces.

The research then addresses the following research tasks. 1) to analyze the energy efficiency of grinding machine tool components. This assessment included applying the axiomatic design methodology to identify those machine tool components, and then creating physics-based models of those components. Use of these models will allow designers to easily calculate energy consumption of a machine tool feed system. 2) To model grinding machine motors for energy consumption in the manufacturing and use phases. This work included performing a literature review of the life cycle inventory models of electric motors, and creating an embodied energy model using the review. This also included performing a study of the energy consumption of a grinding spindle, to identify start-up times for minimum energy consumption and minimum peak power. The two tasks highlighted can be used by machine designers to first determine the embodied energy of their design for energy tradeoff analyses, and second to reduce energy and peak power during the use phase. 3) To investigate the correlation between machine tool energy consumption and workpiece quality. This work included performing a study on energy consumption and resulting surface roughness of grinding steel using cold air for coolant. It was

identified that a correlation does exist, that higher energy consumption is correlated with lower surface roughness.

To my family.

Declaration of Co-authorship and Previous Publication

I hereby declare that this dissertation incorporates materials that are the result of research conducted under the guidance of my advisor Dr. Barbara S. Linke and in collaboration with other researchers. The following sections describe these collaborations in detail.

Chapter 2 Manuscript 1

This work was coauthored with Dr. Barbara Linke, Dr. Eckart Uhlmann, and Dr. Bernd Peukert. Ian Garretson's contributions include authoring the state of the art, identifying possible sustainability axioms, and performing an energy analysis of a ball screw.

Chapter 3 Manuscript 2

This work was coauthored with Dr. Barbara Linke. Ian Garretson's contributions include identifying research direction, performing static analysis, creating an LCA framework to assess energy impacts of electric motors, and creating the example. An edited version of this manuscript had an additional coauthor Qiuhao (Eric) Guo, and can be seen in Appendix A.

Chapter 4. Manuscript 3

This work was coauthored with Dr. Barbara Linke, Dr. Robert Schmitt, Dr. Bjorn Falk, and Henning Voet. Ian Garretson's contributions include developing the experiment design, reading the equipment, recording power measurements, and performing the cost analysis.

Chapter 5. Manuscript 4

This work was coauthored with Dr. Barbara Linke, Dr. Robert Schmitt, and Malte Seibt. Ian Garretson's contributions include creating the design of experiments, readying the equipment, performing experiments, and performing the energy and roughness analysis.

Chapter 6. Manuscript 5

This work was coauthored with Dr. Barbara Linke, Dr. Jörg Seewig, Dr. Matthias Eifler, Dr. Jayanti Das, and Dr. Francois Turner. Ian Garretson's contributions include programming the roughness evaluation parameters and authoring the state of the art section.

I declare that this dissertation includes original manuscripts that have been previously published, are under review, or will be submitted for publication in peer refereed journals and conference proceedings. I certify that I have properly acknowledged the contributions of other researchers to my dissertation.

Acknowledgements

I express appreciation and gratitude to all of those who have helped me along the way to author this book and helped me in my doctoral studies.

My advisor Dr. Barbara Linke

My lab-mates in the MASTeR Laboratory including Dr. Paul Harris, Dr. Jayanti Das, Dr. Destiny Garcia, Farhat Ghadamli, Akshay Kamath, Geng Li, Liam Murphy, Michael Taylor, Fahad Jan, Michael Winterer, Felecia Fashanu, Julianne Jonsson, Xiang Wang, and Alex Georgens

The undergraduate students I mentored including Wilhelmina Figueirdo, Jeih Mienhold, Nicholas Maharaj, Maddison Doutt, Shivam Gupta, Arturo Castaneda Barrios, Walter Parker, Carlos Ortiz, Tremain Sharp, Qiuhao (Eric) Guo, Qingqiao Liu, Gupreet Kaur, Mitchell Gubbins, Maja Beltz, Sebastian Quaisser, Malte Seibt, Taylor Reisinger, Natalia Daraselia, Dzmitrij, Sysou, Mathieu Therberge, Ayan Siddiq, Joshua Kuligowski, and Saul Rameriz

My colleagues that visited from Germany, Brazil and Taiwan including Dr. Bernd Peukert, Dr. Francois Torner, Max Altenhof, Kim Scheffler, Moritz Glatt, Florian Gruss, Andrej Keksel, Gulsum Mert, Henning Voet, Daniella Van der Spiegel, Vardan Vardanyan, Zhibo Zhang Fernando Moreira Bordin, Zhe-Jian (Jerry) Liao, and Hao-Jan (Daniel) Lu

My collaborators in research projects including Dr. Mohamed Hafez, Dr. Lee Martin, Dr. Matthias Eifler, Dr. Jörg Seewig, Dr. Anjali Roeth, Dr. Robert Schmitt, Dr. Bjorn Falk, Dr. Eckart Ulhmann, and Manuel Lopez

Table of Contents

List of Figures

List of Tables

List of Appendices

Chapter 1: Introduction

According to Lawrence Livermore National Laboratory (LLNL and DOE, 2018), industrial energy consumption accounts for 35% of all energy consumed in the United States and is second to transportation at 37%. Industrial Energy can be subdivided into process and non-process energy; wherein process energy accounts for 88% of energy expenditures and is only 58% efficient (DOE, 2010). Process energy can be subdivided again and includes machine drive energy (19%), which is 6.1% of all US energy consumption (4.3 Quadrillion BTUs), and is only 35% efficient, making it 3.9% (2.8 Quads) of all US energy losses not including generation and transmission losses. Thus, energy consumption in machine drives, one aspect being machine tools, needs to be researched to reduce energy waste in the United States. Design analysis tools that enable engineers to understand and improve energy consumption in machine tools need to be created. Besides energy, further environmental and social impacts of manufacturing are increasingly important to academia and industry, which are captured in sustainability analysis.

1.1 Background in sustainability and lifecycle assessments

Sustainability metrics are categorized into economic, environmental, and social aspects (Brundtland, 1987). In manufacturing, environmental impacts have a causal link to processes, but social impacts have a causal link to company conduct (Jørgensen et al., 2007). Different processes at a single company could have similar social impacts but different environmental impacts, whereas similar processes at different companies would have different social impacts but similar environmental impacts. Additionally, Jorgensen et al. (2007) noted that selecting appropriate social impacts for life cycle assessment (LCA) remains an open question, and will likely be

influenced by the type of decisions to be made and the manufacturing system being studied. The complexity of selecting good indicators is further exacerbated by the quantity of indicators, notably the NIST Sustainable Manufacturing Indicator Repository has over 400 indicators from 5 categories (DOC, 2013). But, energy consumption and energy efficiency is identified as a focus area in sustainable manufacturing (Duflou et al., 2012; Haapala et al., 2013). Additionally, processes that rely heavily on electricity for input energy, as opposed to natural gas for example, and have no significant direct emissions will have emissions impacts directly correlated with their electricity supply. Thus, the research proposed herein focuses on energy consumption primarily and other environmental indicators secondarily.

Relatively few tools have been developed to address the needs of design engineers during product development. Ramani et al. (2010a) classified eco-design tools into three categories: checklists, LCA based, and quality-function- deployment (QFD) based. They claimed that all of these tools have limitations, current LCA tools are not design oriented, checklist tools provide guidelines rather than solutions, and QFD tools are too reliant on the designer's knowledge (Ramani et al., 2010a). Thus, tools are needed that provide sustainable design solutions that educate designers without requiring perquisite sustainability knowledge.

The most detailed and widely developed sustainability assessment tool is life cycle assessment (LCA). LCAs, make use of energy or material flow analysis, termed life-cycle inventories (LCIs), and contain generalized process data and information (Kellens et al., 2012a). LCA methods and tools – such as GaBi, SimaPro, Quantis, and Earth Smart – enable engineers and supplier managers to make better, environmentally sound decisions; but they do not yet provide detail to support

robust engineering decisions. Perhaps the most appropriate use of LCA is for reporting environmental impacts of a finished product. Also LCA has significant pitfalls which include cost, complexity, time, multiple standards, and subjectivity, which make LCA studies opaque (Jensen et al., 1997; Reap et al., 2008). Thus, there is ample opportunity to create additional tools for designers to use to assess environmental sustainability.

Typically, a lifecycle assessment or a sustainability analysis will assess metrics from the three pillars of sustainability, being economic, environmental, and social. These three sustainability aspects can be attributed in origin to the Brundtland report (Brundtland, 1987) and provide a framework to development that seeks to meet the needs to today and future generations. The aspects seek to provide balance to developing in our society and to avoid creating a society that sacrifices a single aspect for another. Another aspect of sustainable development is to enable long-term thinking and create societies that work and last for many generations; not just the current generation. This work will focus on energy consumption; for reference example metrics for economic, environmental, and societal impacts for manufacturing environments are shown below (Haapala et al., 2013):

- Economic
    - Cost
- Environmental
    - Energy Consumption
    - Materials Consumption
    - Waste Management
- Societal
    - Worker Safety
    - Worker Health

1.2 Background information on unit manufacturing processes

Unit manufacturing process (UMP) modeling can be traced back to the call for research by the U.S. National Research Council (NRC) in 1995 (NRC, 1995). Initial UMP models developed in the early 2000s investigated specific processes using ad hoc methods, e.g., (Choi et al., 1997; Dahmus and Gutowski, 2004; Jiménez-González et al., 2001, 2000). More recent methods have attempted to standardize the specific modeling aspects, i.e., boundary criteria and evaluation criteria, and include UPLCI (Duflou et al., 2011; Overcash et al., 2009) and CO2PE! (Kellens et al., 2012a, p. 1, 2012b, p. 2). Researchers at the U.S. National Institute of Standards and Technology (NIST) have developed information models usable for UMPs (Mani et al., 2014; Valivullah et al., 2014). Finally, the Gutowski method utilizes exergy analysis for characterizing the energy consumption in manufacturing processes (Gutowski et al., 2009); additionally Gutowski et al. (2009) created a highly cited curve comparing specific energy and the volumetric processing rate for a wide variety of manufacturing processes, but this analysis failed to include quality. There are not many UMPs developed for generic use; most are applicable for the specific machines or processes that they are modeled after. Furthermore, there is a need to include quality in UMP models especially for finishing processes.

1.3 Sustainability in grinding

Many previous research studies performed on the sustainability of grinding have focused on optimizing the processing parameters to improve sustainability performance. Aurich et al. (2013) for instance investigated grind hardening to identify the optimal parameters for processing low carbon steel. Denkena et al. (2005) analyzed high carbon steel to compare energy consumption of various machine loads. Murray et al. (2012) performed a similar study for grinding a cobalt-

chromium alloy knee implant. Both Denkena et al. (2005) and Murray et al. (2012) used results to inform on highest impact reduction through control of the machine tool. Winter et al. (2014) developed a multi-objective optimization model for reducing impact of grinding processes; the model provides guidelines for machine parameter control for opposed objectives. Wegener (2017) identified that power measurements of many grinding machine tools show that components were oversized due to unknown process needs and the belief of more is better. Linke and Overcash (2017) identified that a majority of energy data is estimated from manufacturer data or single measurements, rather than being from analytical models. More research is needed and is a motivation for this dissertation.

1.4 Energy consumption in machine tools

Filippi and Ippolito (1981) performed an early investigation into machine tool energy efficiency, finding that NC machines had a mean energy efficiency of 64%. Diaz et al. (2010) performed a life cycle assessment on machine tool design comparing a Bridgeport Manual Mill to a Mori Seiki DuraVertical 5060 resulting in 600kJ/part and 1,000kJ/part; the early investigation does not provide much insight into design-based energy efficiency improvements. Avram and Xirouchakis (2011) developed an energy consumption model for spindle power and feed axes power for a milling machine tool, and utilized this model to compare various tool paths. Zein (2012) performed a thorough review on energy-efficiency of grinding tools, but does not include analytical models or microscopic models. Bohner et al. (2014) identified that the design phase of a machine lacks use phase data causing energy losses and implemented an optimization tool for reducing energy consumption utilizing the machine controller. Finally, Zhou et al. (2016) reviewed energy efficiency in machine tools, and identified types of energy decompositions: by system, by

operational status; by energy attribute; by main components; and by functional movement. Models were divided into: material removal rate (MRR) type; parameter-correlation type; and process-movement-oriented type. Finally, they identify that energy consumption models are trending toward: real-time energy data; kinematics-based consumption; NC code simulations; and integration of additional factors (e.g., tool wear). In summary, physics-based energy efficiency models for the grinding process and grinding machine tool are needed.

1.5 Research Objectives

From the needs identified in the literature, the research hypothesis of this dissertation is *that physics-based models of grinding machine tools and abrasive processes lead to more energy-efficient machine tool design.* Grinding machine tools are commonly utilized to produce high-quality finishes and highly accurate geometry, or process highly brittle materials. The research questions that lead from this hypothesis are:

Question 1: What are the components of grinding machine tools that affect energy efficiency?

Question 2: How can the machine tool systems be modeled to guide energy efficient design?

Question 3: How is quality correlated with high energy consumption in machine tools?

The research questions will seek to address, manufacturing-phase energy consumption (Q1), use-phase energy consumption (Q2), and the impacts on reducing energy consumption on product workpieces (Q3).

1.6 Research Tasks

The following research tasks arise from the research questions:

Task 1: To analyze the energy efficiency of grinding machine tool components while regarding accuracy. Subtasks include, identifying the components of the machine tool using axiomatic design. Apply physics-based models to estimate the energy consumption of operating the machine tool components. Create a streamlined energy model of a coolant pump system.

Task 2: To model grinding machine motors for energy consumption in the manufacturing phase and use phase. Subtasks include performing a literature review of the electric motor life cycle inventories. Creating regression models to motor sizing data to determine motor mass. Create a model of energy consumption for manufacturing phase life cycle impacts. Perform a study of the energy consumption of a spindle motor. Identify optimization for energy consumption and peak power during the use phase of life cycle impacts.

Task 3: To investigate the correlation between machine tool energy consumption and workpiece surface roughness. Subtasks include coding surface roughness parameter calculations and were applied to an example using a vibratory finishing study. Perform a literature review to determine which areal roughness parameters were found to correlate with finishing steel surfaces. Perform a study on the energy consumption and resulting surface roughness of grinding hardened 440 C stainless steel.

Chapter Two: Hypothetical Sustainability Axioms for Axiomatic Design with an Application in Grinding Machine Design

By

Ian C. Garretson, Bernd Peukert, Barbara S. Linke, Eckart Uhlmann

Accepted and presented at *Proceedings of the ASME 2017 International Manufacturing Science and Engineering Conference*

https://asmedigitalcollection.asme.org/MSEC/MSEC2017/volume/

Chapter 2: Hypothetical Sustainability Axioms for Axiomatic Design with an Application in Grinding Machine Design

2.1 Abstract

The design of a high precision machine tool presents one main goal for an engineer: to maximize productivity while minimizing resource inputs and wasted outputs. Incorporating additional design requirements to improve the sustainability of the machine tool presents challenges to design engineers. Should productivity be sacrificed for resource efficiency improvements? Previous tools used for incorporating sustainability principles into design provide guidance but lack necessary detail for making informed decisions, or the tools rely on the engineer's previously developed knowledge in sustainable design. Axiomatic design, being an already accepted system design framework, provides an opportunity to incorporate sustainability considerations into the core of design activities rather than having sustainability be a side activity. A methodology for designing sustainable machine tools using axiomatic design is presented, and a case study on a grinding machine is investigated. A list of hypothetical sustainability axioms are proposed, similar to how the original axioms of axiomatic design were proposed. The axioms are then discussed using the example of a grinding machine tool.

2.2 Introduction

Sustainability in manufacturing is becoming more pertinent to being competitive in modern corporate culture (Lozano, 2012). Sustainability is not only a marking advantage for inclined businesses, but also provides businesses with indirect cost savings through increased efficiency and technical aptitude to better understand the impacts and the capabilities of their manufacturing

system (Jovane et al., 2008). Non-renewable resources are being depleted, and for example, in the US domestic bauxite annual consumption is estimated to be 9.0 million tons and domestic resources of bauxite are inadequate to meet long term demands (USGS, 2016). Fortunately, alternative sources of aluminum are available in the US (USGS, 2016), but depletion of natural deposits proposes a risk because not all commodities are inexhaustible and the transition from a mining-based to an alternative-source supply chain poses serious risks and costs for businesses (Hallstedt et al., 2013).

First proposed by Pacala and Socolow (2004) as stabilization wedges, and later by Dornfeld and Wright (2007) as technology wedges, the idea conceptualizes the overarching method that improvements are made in modern technology in regards to sustainability. The underlying idea between both sets of authors is that incremental improvements need to be utilized to make any significant improvement to sustainability in society. Pacala and Socolow (2004) identified improvements to reduce carbon dioxide emissions, whereas Dornfeld and Wright (2007) identified that the concept can be used across a broad range of industries and technologies in the manufacturing sector.

Improvements can be made at different perspective levels of manufacturing, one grouping being processes, systems, and supply chain levels (Haapala et al., 2013). Improvements at the process level can be development of new and novel machines, optimization of current process parameters, and redesign of machines. This paper addresses the design of a grinding machine tool, for a process that is widely used in many industries. Finally, Vallet et al. (2013) evaluated the performance of eco-design experts in redesigning a consumer product and found that experts rely on experience

and previous knowledge rather than the eco-design tools for initial impact assessments and design strategy definition. The goal of this paper is to incorporate additional sustainability into axiomatic design with the example of a grinding machine, thus possibly reducing required expertise for sustainable design.

Following this Introduction, a Background is discussed covering both sustainable design, grinding machines, and axiomatic design, furthermore a review is provided that identifies previous methodologies that incorporated sustainability into axiomatic design. Next there is a section on Axiomatic Design Concepts to provide an overview of the method. Following, is a section on Incorporating Sustainability into Axiomatic Design that presents the hypothetical sustainability axioms. Then, an Application section with an example on ball screw selection for a grinding machine. And finally, the Conclusion section reviewers the future work needed for the method.

2.3 Background

The background section will address three topics: 1) Sustainable design methods, 2) sustainability in grinding, 3) axiomatic design of machine tools, and 4) sustainability in axiomatic design. These four topics encompass this paper, as the purpose is to provide a sustainable design method using axiomatic design for a grinding machine tool.

2.3.1 Sustainable Design Methods

Sustainable design methods, termed eco-design tools, have been organized by Ramani et al. (2010b) into three categories being: lifecycle assessment (LCA)-based, checklist-based, and quality function deployment (QFD)-based. They identified that all categories of current tools all

have qualities that make their use either challenging or fail to provide solutions, and that integrating more lifecycle information into design methodologies is needed. Chiu and Kremer (2011) organized Design for X (DfX) concepts as either (1) design for efficiency or (2) green design. While the authors stated that the two concepts are complementary for design practices the concepts are not mutually exclusive either, product design methods that consider green or sustainable principles do not need to be classified as making a system or design less efficient. However, they identified that future research should be invested for integrating DfX concepts into a framework. Chiu and Chu (2012) identified that while environmental impacts are commonly evaluated in eco-design studies, social impacts and long term impacts are less studied and methods are needed to account for impacts in a broader context.

Sy and Mascle (2011) proposed a method for sustainable product design using lifecycle features; which are, "geometric, technological, or functional information assigned to a face, part, or subassembly that is inherent to the manufacturing, assembly, maintenance, recycling, or disposal processes." The focus of design using this method is thus shifted to non-use phase. A similar idea is presented in this paper such that the design process should incorporate the entire product lifecycle. Azapagic (2006) identified alternative sustainable designs by: identifying non-conventional designs, identifying environmental and social issues at an early stage, targeting *hot-spots*, and avoiding economic costs. While these ideas are applied to plant design, similar concepts can be applied to product design. Lewandowska and Kurczewski (2010) presented the ISO/TR 14062:2002 standard (ISO, 2002) for integrating environmental aspects into product design and development. They identified that the tool is not simple, requires knowledge from the practitioner,

but does not omit any lifecycle stages. Thus, a simpler tool could be beneficial to designers to incorporate lifecycle and sustainable thinking.

Luttropp and Lagerstedt (2006) developed their 10 golden rules for integrating eco-design into product development. As a method, the rules have to be adapted to each design and then can provide guidance for design decision. But the authors identify that while useful they can be contradictory, and it is important to note here that sustainable design incorporates additional design criteria. Sustainable design is then a multi-objective process that will likely have multiple solutions without a best answer. Bovea and Perez-Belis (2012) created a taxonomy for eco-design tools and created a tool selection guide to aid designers in selecting a tool that incorporates both the desired evaluation criteria (e.g. safety, legal) and the method (e.g. QFD, FMEA). But the authors note that companies often do not apply such tools because the tools are too complex and time investment and lack of environmental knowledge. The authors identify three key factors of an eco-design tool: 1) early integration of sustainability into design process, 2) lifecycle approach incorporating various product stages, and 3) a multi-criteria approach.

2.3.2 Sustainability in Grinding

Gutowski et al. (2009) performed an analysis of energy consumption per unit volume of material processed in manufacturing processes, and found that more precise processes use more energy per unit volume across a broad range of manufacturing processes. In addition, for traditional machining processes, grinding is at the higher end of energy consumption. This comparison however does not take product quality into account. Li et al. (2011a) investigated energy consumption of various conventional machining processes. The authors classified energy

consumption into systems and the components in those systems. This classification method is useful and a similar method can be applied in axiomatic decomposition.

Many previous research studies performed on the sustainability of grinding has focused on optimizing the processing parameters to improve sustainability performance. Aurich et al. (2013) for instance investigated grind hardening to identify the best parameters for processing low carbon steel. Denkena et al. (2005) analyzed high carbon steel to compare energy consumption of various machine loads. Murray et al. (Murray et al., 2012) performed a similar study for grinding a cobalt-chromium alloy knee implant. Both Denkena et al. (2005) and Murray et al. (2012) used results to inform on best impact reduction through control of the machine. Winter et al. (2014) developed a multi-objective optimization model for reducing impact of grinding processes; the model provides guidelines for machine parameter control for opposed objectives.

2.3.3 Axiomatic Design of Machine Tools

Axiomatic design has been used to both design and improve machine tools. Melvin et al. (2001) performed an axiomatic decomposition of a chemical-mechanical planarization (CMP) machine, used to manufacture integrated circuits for microprocessors, in chapter 8.6 of the book. The decomposition identifies the *top-level* functional requirement (FR) and design parameter (DP), sometimes indicated as (FR0) and (DP0):

- FR0: to maximize return on investment (ROI).
- DP0: the CMP machine design.

The top-level FR and DP and then each decomposed into 5 *highest level* FRs and corresponding DPs; and the decomposition continued with a total of 9 levels. While specific to ROI of a CMP machine, the higher-level sections of the decomposition can provide guidelines for analysis of other machines. Lee and Suh (2006) performed an analysis of various composite machine elements using axiomatic decomposition as a guiding method. Each example in the chapter uses at most three FRs and DPs to analyze the tradeoffs between stiffness, inertia, and damping of the composite machine tool. Thus, examples from both Melvin et al. (2001) and Lee and Suh (2006) showed that meaningful results can be obtained using axiomatic design by either performing a highly detailed decomposition or using the method for problem formulation respectively.

Zein et al. (2011) performed a decomposition on a grinding machine to analyze the energy consumption of the electrical components. The top level:

- FR0: to minimize energy demand of a machining cycle.
- DP0: energy efficient machine tool decomposition.

An excerpt from the decomposition is (Zein et al., 2011):

- FR2: reuse energy
- FR21: ensure energy feed back
- FR211: reuse kinetic energy to power machine tool

Thus, the approach to reduce machine tool energy consumption is generic and could be applied to non-grinding tools. Thus, the axiomatic decomposition is developed from the systems level in a top-down approach. Linke and Dornfeld (2012) similarly performed an axiomatic decomposition of a grinding tool wheel, with their top level:

- FR0: that material has to be removed.
- DP0: material separation.

A section of the decomposition then includes:

- FR1: generate main effect
- FR11: generate force
- FR12: provide cutting edges
- FR111: control workpiece surface profile depth

The decomposition is specific to grinding machines and could not be applied to other machine tool types, which shows a systematic analysis of the machine tool from the process perspective or being a bottom-up approach. Thus, minimization of environmental impact can be performed by taking either a top-down or bottom-up approach.

2.3.4 Sustainability in Axiomatic Design

In addition to Zein et al. (2011) and Linke and Dornfeld (2012), the following authors have utilized sustainability principles with axiomatic design.

Wallace and Suh (1993) first utilized AD to incorporate environmental metric into design. They identified that MCSA comparisons using weighting factors are inadequate because the weighting factors are usually selected arbitrarily are difficult to establish. They claim that using information content (probability of fulfilling design requirements) eliminates bias of arbitrary weight factors, but note that the authors simply sum their information metric across design factors and minimize

that total information calculation; doing so is a MCDA method using weights equal to one. But the authors did incorporate sustainability criteria as proposed goals (CRs), product attributes (CRs), design goals (FRs), constraints (CSs), and design strategies (DPs). But the authors did not discuss how they organized their various criteria into these categories.

Stiassnie and Shpitalni (2007) incorporated lifecycle considerations into axiomatic design but utilized the same top level functional requirement (FR0) as Melvin et al. (2001). The authors incorporated environmental impact through compliance to legislation and avoidance of economic penalties to account for the lifecycle:

- FR4: decrease economic environmental penalties
- DP4: design a manufacturing system that complies with legislation standards.

Thus, environmental impact is accounted for with monetary units. But the authors make a good point that the higher a FR is incorporated into the hierarchical level the more emphasis and importance is placed on it. The authors then use a standard sum-product weighting scheme to minimize the sum of environmental information and non-environmental information.

Kahraman et al. (2009) utilized a multi criteria decision analysis method (MCDA) to inform policy on more sustainable power generation alternatives (wind, solar, etc.). The authors combined fuzzy analytical hierarchy process (AHP) and the axiomatic design (AD) concept of information minimization to select the best alternative energy plant using 18 criteria. They calculated the information content for each criteria for using triangular fuzzy numbers (TFN) using Eq. (2.1) from AD (Kahraman et al., 2009):

$$I_{criteria} = log_2\left(\frac{TFN\ of\ system\ design}{Common\ area}\right) \quad (2.1)$$

Where $I_{criteria}$ is the information content of each criteria of each energy alternative. Thus, the authors utilized the information content calculation to find the best solution to a selection of alternative energies problem, omitting other AD principles. The method is one of selection rather than ideation.

Shin et al. (2011) and later Morrison et al. (2013) created a method that integrates cost engineering with AD, arguing that lifecycle engineering is similar to cost engineering. The authors identify that selection of ecological design parameters is non-trivial. They created a list of *eco-factors,* and incorporated eco-factors into the design matrix (as additional rows) and indicate eco-based AD concepts as *eFR*, *eDP*, etc. The authors identify that if a need can't be made to be independent it has to be classified from an FR to another concept, perhaps as a CS, or an optimization criteria (OC). The authors give the example of "minimal LCA value" as being similar to optimizing cost and are either a CS or an OC. The authors classified eFRs as goals, and eDPs as methods, and industry regulations as eCSs. The authors provide 24 eFRs that can be integrated into any AD process; they claim the eFRs were derived from external environmental design criteria but mapping from their sources to their eFRs was not performed. Finally, the authors provide an assessment in CO_2 for a material comparison, but fail to compare meaningful ecological impacts for replacing a lithium-ion battery with an ultra-capacitor e.g., CO_2 emitted during manufacturing. Overall, the method is a step in the right direction as it provides a means for designers to incorporate sustainability principles within their process.

2.4 Axiomatic Design Concepts

The design process using axiomatic design, from Kim et al. (1991), is as follows:

1. Establishment of design goals to satisfy a given set of perceived needs.
2. Conceptualization of design solutions.
3. Analysis of the proposed solution.
4. Selection of the best design from among those proposed.
5. Implementation.

The steps above are a framework around which the axiomatic design process is performed. The process is used to map customer requirements (CRs) to functional requirements (FRs), FRs to design parameters (DPs), and DPs to process variables (PVs) as seen in Figure 2.1. This paper will focus on the functional and physical domain.

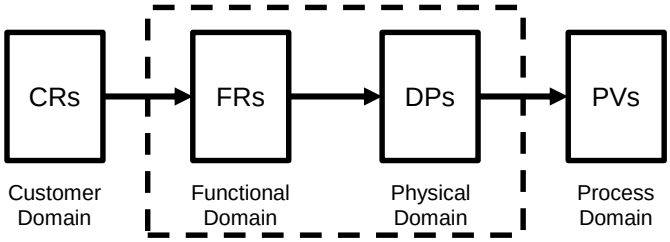

Figure 2.1: Concept of mapping in axiomatic design, adapted from Lee and Suh (Lee and Suh, 2006).

Mapping from one domain to the next is satisfied by considering the domain on the left as constraints and the domain on the right as satisfactory answers or solutions. The axioms are aids for the mapping activity, and are guidelines which must be met to achieve a robust design. A useful list of definitions follows (Lee and Suh, 2006):

- "Constraint: Bounds on acceptable solutions, either imposed by design specifications or by the system in which the product interacts."
- "FR: An independent requirement that characterizes a functional need; in whole the FRs are a minimum set to characterize a functional need for a product." Starts with a verb, independent, and solution neutral.
- "DP: A key physical variable that satisfies a FR and characterizes the design."
- "PV: a key process variable that satisfies a DP and characterizes the process."

2.4.1 The Axioms

The axioms are (Suh, 2001):

- Independence axiom: maintain independence of the FRs.
- Information axiom: minimize information content of the design.

The independence axiom is best explained by the equations used to relate FRs to DPs, where {FR} and {DP} are vectors and [A] is a matrix. Equations (2.2) and (2.3)demonstrate mapping between domains (Lee and Suh, 2006).

$$\{FR\} = [A]\{DP\} \tag{2.2}$$

$$\begin{Bmatrix} FR1 \\ FR2 \end{Bmatrix} = \begin{bmatrix} A11 & A12 \\ A21 & A22 \end{bmatrix} \begin{Bmatrix} DP1 \\ DP2 \end{Bmatrix} \tag{2.3}$$

Where independence is obtained when [A] is a diagonal matrix (terms Aij = 0 and Aii ≠ 0), or is a lower triangular matrix (Aij = 0 where i < j). See Eq. (2.4) and (2.5) (Lee and Suh, 2006).

$$\begin{Bmatrix} FR1 \\ FR2 \end{Bmatrix} = \begin{bmatrix} A11 & 0 \\ 0 & A22 \end{bmatrix} \begin{Bmatrix} DP1 \\ DP2 \end{Bmatrix} \tag{2.4}$$

$$\begin{Bmatrix} FR1 \\ FR2 \end{Bmatrix} = \begin{bmatrix} A11 & 0 \\ A21 & A22 \end{bmatrix} \begin{Bmatrix} DP1 \\ DP2 \end{Bmatrix} \quad (2.5)$$

The information axiom is used in terms of the information content of the design, which is the probability of successfully achieving all FRs (Lee and Suh, 2006). The probability of a successful design is said to increase e.g., as design range, i.e., goals or FRs, widen and when the system capabilities, i.e., DPs, widen as well. For example, if the goal of the machine is to polish an optical lens to within $\pm 0.1\mu m$ flatness, but we only have calipers to measure the thickness; our designed system capabilities to measure falls outside of the design range. Another example, we need to press and hold a device at $100N \pm 0.01N$, but we only have a hand jack for a car; the likelihood of completing the action is small, widening the tolerances to $100 \pm 10N$ would improve the probability of success. Improved probability of design success is then achieved when the overlap between the FR tolerance and the system capability increases, see Figure 2.2. The information axiom is thus satisfied when the difference between the target value for an FR and the system capability (resulting design) is zero, this difference is termed bias. When multiple DPs affect a single FR and is a triangular matrix, e.g., in Eq. (2.4), bias can be eliminated as well. When bias is eliminated, the information content is said to be zero.

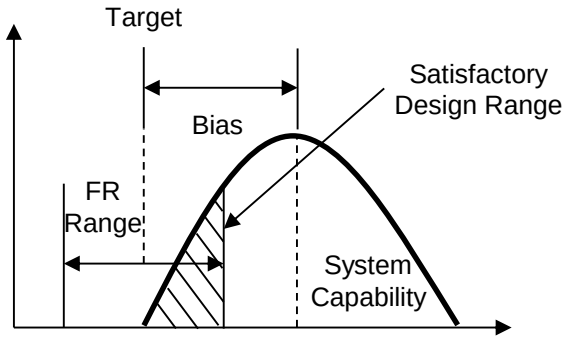

Figure 2.2: Bias is the difference between the FR range and the system capability, adapted from Lee and Suh (2006).

Furthermore, information content is reduced by minimizing variance in the design and can be done so in four ways (Lee and Suh, 2006). First through minimization of *stiffness*, this is the magnitude of the Aij's in Eqs 2-4. Reducing stiffness in a linear design increases the allowable DP range and decreases sensitivity to change, but the stiffness cannot be at or near zero. Second, reduction in variation of Aij's reduces design variance, as Aij's are the coefficients that relate FRs to DPs, see Eq. (2.6).

$$FR2 = A21(DP1)+A22(DP2) \quad (2.6)$$

Third, reduce information content, in a multi-FR design, by identifying important DPs and fixing values for un-important DPs (Lee and Suh, 2006). For example, fixing the value of DP3 or setting the value of A13 to zero in Eq. (2.7). Performing either task would reduce the equation to the triangular matrix seen in Eq. (2.5).

$$\begin{Bmatrix} FR1 \\ FR2 \end{Bmatrix} = \begin{bmatrix} A11 & 0 & A13 \\ A21 & A22 & 0 \end{bmatrix} \begin{Bmatrix} DP1 \\ DP2 \\ DP3 \end{Bmatrix} \quad (2.7)$$

Fourth, reduce information content by eliminating the variance and covariance of DPs (Lee and Suh, 2006). Covariance is present in DPs that are not independent.

Three additional methods can be used to reduce information content. First, in the case that a redundant DP cannot be eliminated through the third method above, the DP with the largest Aij coefficient is selected as the dominating DP, termed DP1. If ΔFR is the allowable random variation of the FR, then the DP can be compensated using Eq. (2.8) below, where ΔDP is the compensation.

$$\Delta DP1 = [\Delta FR - \Sigma Ai(\delta DPi)]/A1 \quad (2.8)$$

Where A1 is the coefficient and ΔDP1 is the compensation for DP1, and Ai are the coefficients and δDPi are the random variations in the DPi for each $i \neq 1$. Second, reduce information content by increasing the design range, this can increase the overlap of the FR and system range (Lee and Suh, 2006). Finally, reduce information content by integrating DPs into single physical parts and maintain independence of FRs. This integration can occur at lower levels in a decomposition, in the physical domain.

2.5 Incorporating Sustainability into Axiomatic Design

Incorporating sustainability into engineering design frameworks can be classified into categories, such as LCA-based, checklist-based, and QFD-based (Ramani et al., 2010b). Furthermore, Ramani et al. (2010b) identifies that tools either fail to provide design solutions or require too much investment into sustainability knowledge on the part of the designer. Thus, incorporating sustainability into axiomatic design is proposed to both provide design solutions and require designers to need less sustainability knowledge. Sadeghi et al. (2013) and Ghemraoui-Lagord et al. (2011) have proposed methods for incorporating safety objectives into axiomatic design. While the two sets of authors did not define axioms, their methods identified risks which were then mapped to safety requirements, similar to how FRs are mapped to DPs.

Theoretical developments of axiomatic design concepts have made improved methods for solving unique problems, Kulak et al. (2010) identified 14 such works. One such work created three axioms

for information theory to solve problems characterized by FRs outnumbering DPs (Pappalardo and Naddeo, 2005). Suh et al. (1978) identified two requirements that define an axiom:

1. Axioms cannot be proven.
2. Axioms are general truths; no violations or counter-examples can be observed.

Furthermore, Suh et al. (1978) posed how to develop the axioms heuristically. First, pose an initial set of axioms. Second, test the set of axioms in a series of case studies, though trial and evaluation, to determine if the axioms satisfy the requirements. The proposed set of axioms is then modified, shrunk, expanded, or redefined until a comprehensive set of axioms remains. Suh et al. (1978) first proposed 8 axioms before settling on Suh's (2001) proverbial two. Thus, this paper will first propose many axioms that could satisfy incorporating sustainability into the product design process. First a brief background into sustainability to provide some background for the new sustainability axioms.

2.5.1 Sustainability Background

Sustainability can be incorporated into axiomatic design in a number of different ways. This section will discuss background information on sustainability to incorporate it into axiomatic design. First, sustainability must be defined in an engineering perspective; from Mihelcic et al. (2003) sustainable design is:

"the design of human and industrial systems to ensure that humankind's use of natural resources and cycles do not lead to diminished quality of life due either to losses in future economic opportunities or to adverse impacts on social conditions, human health and the environment."

Thus, sustainability addresses economic, social and environmental impacts across a long time period. Hence, a sustainable design tool must provide means to quantify the impacts of the three sustainability pillars while also identifying engineering solutions. Finally, taking some key concepts from LCA methods, sustainability impacts are systemic, meaning that to identify the true sustainability solution to a design problem the problem definition must incorporate the entire system, and that solutions to improve sub-systems may not improve the sustainability performance of the whole. Even more so, the sustainability, as part of lifecycle analysis, needs to be quantified across the product's lifecycle, see Figure 3.4, wherein the product is the system and each lifecycle phase is a sub-system. Axiomatic design poses an methodological approach to optimize an entire system (Suh et al., 1978). Note design is highlighted here, while design is not incorporated in to the lifecycle of the product, the design phase of a product dictates much the product's impacts.

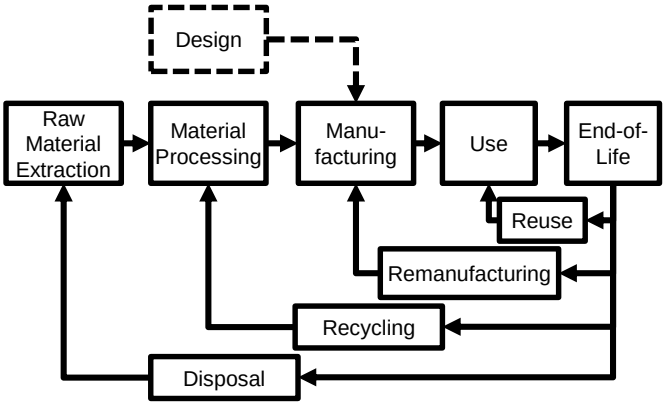

Figure 2.3: The product lifecycle, adapted from Haapala et al. (2008). Solid lines identify material flow and the Dashed line indicates phase outside of the physical product lifecyce.

Finally, quantifying sustainability is done through the use of metrics and indicators (Garretson et al., 2016a), also termed midpoints and endpoints. Haapala et al. (2013) identified six categories of

metrics for measuring sustainability impact for the design and manufacturing of products, these include, consumption, energy, waste, hazardous material, safety, and cost. Ness et al. (2007) categorized indicators as non-integrated, integrated, and regional flows; and notes that an indicator or index is used to represent the state of development in a region. Thus, the metrics will be used for this discussion.

2.5.2 Sustainability Axioms

Then, how can sustainability be incorporated into axiomatic design? Several ideas stemming from sustainability principles can be distilled. One idea is to distill the axioms from sustainability metrics. A second idea is to develop axioms from the phases of the product lifecycle. The first idea will be examined first, that is to identify that various axioms that can be minimized in regards to sustainability metrics. Using metrics identified from Haapala et al. (2013), six hypothetical, *metric-based* sustainability axioms (S. axioms) are proposed, one for each of the metric categories:

- S. Axiom 1 (Consumption): minimize the consumption of resources across the produce lifecycle.
- S. Axiom 2 (Energy): minimize the energy consumption across the product lifecycle.
- S. Axiom 3 (Waste): minimize the output of wastes, emissions, and effluents across the product lifecycle.
- S. Axiom 4 (Hazardous material): minimize the reliance on hazardous materials and chemicals.
- S. Axiom 5 (Safety): minimize the probability of human injury and disease to be caused by the product across the product lifecycle.
- S. Axiom 6 (Cost): minimize the costs of the product across its lifecycle.

The metric-based axioms above provide guidelines similar to those found in checklist-based sustainability design methods (Ramani et al., 2010b). These metric-based axioms are also centered on the concept of minimizing the negative direct and indirect lifecycle impacts of the product. It is then possible to reduce these down to a single axiom but doing so reduces the guidance that they provide. A concern is that S. axiom 6 is an inverse of the top level FR from Melvin et al. (2001) (maximize ROI) whereas here is to minimize cost. All S. Axioms 1-6, being of similar construction, currently fit the definition of a Top-level FR, and thus cannot be axioms. But it still maybe possible that one could replace the information axiom with the hypothetical S. axiom 2, and minimize the energy predicted to be required of product rather than the predicted information to be generated during the design process. Doing so may not lead to the equivalent Suh-based design, but would lead to a more robust lifecycle design.

Note, each of the S. axioms above states that the axiom is applied across the lifecycle, which means the design optimization should include raw material extraction, material processing, manufacturing, use, and end-of-life phases. The entire lifecycle is termed cradle-to-grave (extraction to end-of-life) in the LCA community. LCAs are on occasion performed on a smaller scope, e.g., cradle-to-gate scope which is raw material extraction, material processing, and manufacturing; omitting lifecycle phases is done when limited information about those phases is present. Such omission maybe applicable when new and untested technology is developed, but in instances where industries are already well developed, e.g. automobiles, airplanes, computers, or milling machines, and the end-of-life supply chain is developed, then omission of lifecycle phases should be avoided. However, if the designer is developing new technology without a definite end-of-life, impacts of similar products be substituted for calculations.

An alternative measure is to develop axioms that address the lifecycle and less the impacts and thus encourage designers to think more broadly about their product. These axioms are derived from Fig. 3 and definition for sustainable design from Mihelcic et al. (2003). *Lifecycle-based* axioms we propose are:

- S. Axiom 7 (Lifecycle phases): there must be at least one FR for each phase of the product lifecycle.
- S. Axiom 8 (Lifecycle impact minimization): the impacts of the product must be minimized across the lifecycle of the product.
- S. Axiom 9 (End-of-life): minimize long term impacts of the product by minimizing the end-of-life impacts.
- S. Axiom 10 (Critical phase): a critical phase of product is significantly more impactful than all other phases and impacts of the critical phase should be minimized.
- S. Axiom 11 (Impact through reliability): minimize the probability of the product failing, needing to be replaced, or impact when replaced.

S. axiom 7 is similar to the independence axiom because both apply constraints on the FRs; while the independence axiom in part defines the FRs, the lifecycle phases axiom gives guidance on the generation of FRs. S. axiom 8 is perhaps an axiom, but reads much like a FR. S. axioms 9-11 are not necessarily always true, and are possibilities for carrying out S. axiom 8 for products with high impacts in those respective phases. But S. axioms 8-11 could also be system constraints, if the designer finds that implementing them as top level FRs leads to a non-independent design.

Similarly the ten golden rules developed by Luttropp and Lagerstedt (2006) could be adapted as system constraints into AD.

Because sustainable design is in part planning for the future and is implemented in a vast array of methods, generalization of sustainable design to a single axiom may not be possible. The axioms for sustainability need to provide design guidance toward solution optimization in a similar method that Suh's independence and information axioms do. Two possible axioms to encompass all of the above axioms:

- S. Axiom 12 (Sustainability impacts): minimize negative impacts of the product.
- S. Axiom 13 (Sustainability benefits): maximize positive benefits of the product.

Axioms 12 and 13 do not define the methods for comparison of negative impacts or positive benefits, nor do they identify metrics that would be used to measure these impacts. But these are likely too generalized for useful benefit by a designer. Thus, S. axioms 1-6 could be used as replacement of the information axiom, or S. axiom 7 could be integrated into the AD methodology. And finally, a compendium of FRs and CSs could be generated similar to that by Morrison et al. (2013). Similar to the work by Suh et al. (1978), the application of the hypothetical axioms is left to be defined in later work. And while Suh et al. (1978) had defined their axioms from the design tools used, the axioms here were defined from sustainability principles.

2.6 Application

The examples in this section will explore the different S. axioms identified in Section 3. First the section will address the metric-based axioms, and then it will tend more to the lifecycle-based axioms.

2.6.1 Metric-Based Sustainability Axioms

Utilizing one of the metric-based axioms (S. Axioms 1 – 6) could take several different forms. S. axiom 2 the energy axiom will be addressed. This axiom again is to minimize the energy consumption across a product lifecycle. Let us examine the linear motion of a grinding machine axes. Precise linear motion can be achieved using three methods rack-and-pinion drives, friction drives, lead screw drives (Slocum, 1992). Both rack-and-pinion and friction are not able to provide large mechanical advantage and require larger drives (Slocum, 1992), and common lead screws include ACME and ball screws. Thus, the top-level FR and DP for the linear motion device for the saddle are:

- FR0: move the saddle
- DP0: a part that moves the saddle

According to SPI-SI (SDP-SI, n.d.), the maximum speed (also called critical speed) and maximum load calculations is independent of thread design. Both of these calculations are ratios of diameter to length and correcting using an end support factor, which incorporates the changing dynamics of supported and unsupported ends of the screw. Note, critical speed is a function of vibration frequency, and maximum load is a compressive buckling load. Variation in ball screw and ACME screws in price and desired speed, ACME screws are limited in their permissible speed which is

different than the critical speed (Lipsett, n.d.). Fatigue life is also more predictable in ball screws using the L10 life calculation, whereas ACME screws can require fatigue life tests in the design phase for predicable wear results (Lipsett, n.d.). Following the design guidelines for ACME and ball lead screws (NSK, n.d.; SDP-SI, n.d.; Thompson, n.d.), the decomposition is in Figure 2.4.

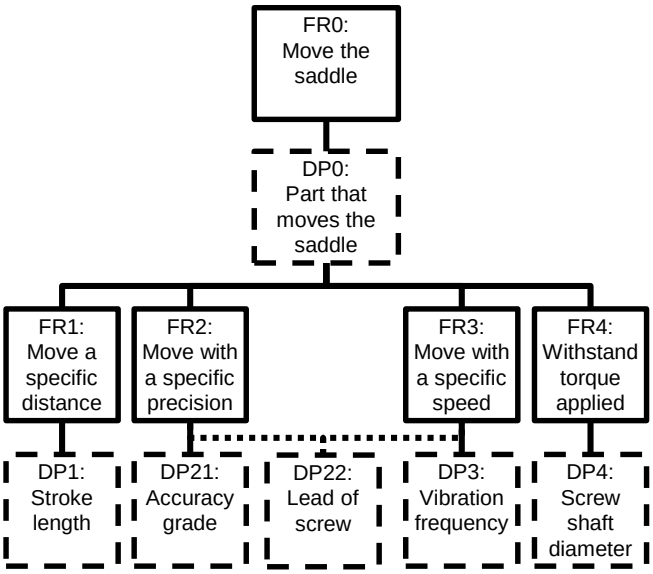

Figure 2.4: decomposition of the lead screw design.

Minimizing the energy content in the selection of a lead screw can then be done by calculating the work requirement. The work required to perform a given duty cycle can then be calculated from the torque as seen in Eq. (2.9).

$$W = \int_{\theta 1}^{\theta 2} T d\theta \quad (2.9)$$

Where θ_1 and θ_2 are the initial and final angles of rotation. As can be seen minimizing the work can be done by minimizing the torque. According to the selection guide for ball and ACME lead screws from SDP-SI (SDP-SI, n.d.), the torque required for turning either screw type is in Eq.

(2.10). Minimizing the torque required to translate the lead screw will decrease the required motor size for the grinding machine tool.

$$T = \frac{F_T \cdot \mathrm{L}}{2\pi \cdot \eta} \quad (2.10)$$

Where F_T is the total force (acceleration, external, and friction), L is the lead, and η is the efficiency (0.9-0.95 for ball screws and 0.3-0.5 for acme screws (SDP-SI, n.d.)). The efficiency for an ACME screw is seen Eq. (2.11) (Thompson, n.d.).

$$\eta = \frac{\tan(\theta_h)}{\tan(\theta_h + \arctan \mu_f)} \quad (2.11)$$

Where θ_h is the helix angle and μ_f is the friction coefficient. The helix angle can be calculated from the lead using Eq. (2.12).

$$\theta_h = \arctan\left(\frac{2\pi r}{\mathrm{l}}\right) \quad (2.12)$$

Where r is the radius of the screw and l is the lead of the screw. The following parameters will be used for the example:

- Lead = 5
- Saddle mass = 150 kg
- Screw length = 620mm
- Shaft diameter = 32mm
- Steel density = 7.8×10^{-3} kg/cm^3
- The operating load is assumed to be 2000 N

- Slide bushing friction coefficient of 0.005
- ACME nut friction coefficient 0.1.

Following the procedure outlined by NSK (NSK, n.d.) (page B63) the required torque is calculated as the sum of the bearing preload torque, the dynamic friction torque, and the operating torque. In the example, the saddle move horizontally and rests on a triad of steel ball bushing bearings (or slide bushings) with a coefficient of friction of 0.005 (Thompson, n.d.). Thus, sliding load seen by the screw is 0.75 N. Furthermore, the preload value is set at one third the axial load resulting in 660 N. The friction coefficient for the ACME nut is assumed to be 0.1. Using Eq. (11), efficiency of the ACME screw is calculated to be 76 percent as compared to the assumed 95 percent of the ball screw.

Assuming a 30TAC62 bearing pair, the starting torque is 0.66 N·m (NSK, n.d.). The dynamic friction torque for the ball screw is calculated to be 0.37 N·m, whereas the same for a lead screw is 1.06 N·m. Using Eq. (10), operating torque for the ball screw is 16.75 N·m, and the operating torque for the acme screw is 20.91 N·m. Thus, the total torque for the ball screw and the ACME screw are 17.78 N·m and 22.62 N·m. Note that additional torque loads are present in the dynamic system of a machine tool, but it is assumed here that the largest load will occur during operation i.e. workpiece grinding-wheel engagement. Thus, the ball screw is selected because the lower torque requirement will result in lower energy consumption over the lifetime of the grinding machine tool and allows for a smaller electric motor to be selected.

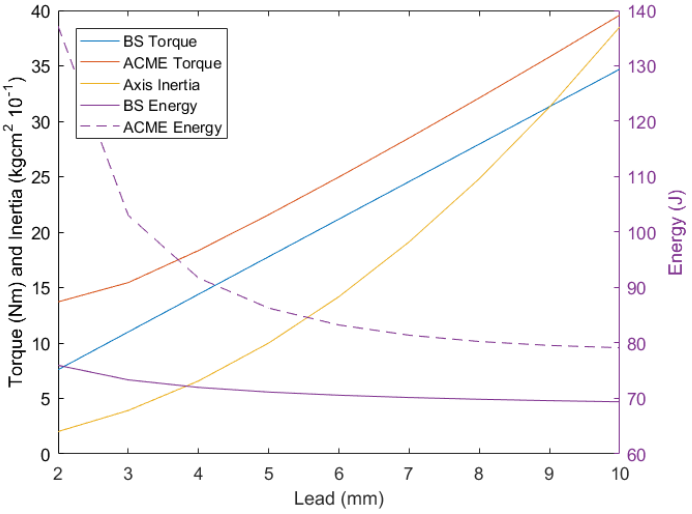

Figure 2.5: Lead Screw Selection Example.

Figure 2.5 provides a theoretical example, wherein an axis servo motor would need to be selected utilizing both the torque and inertia requirements. It is seen that a ball screw (BS) compared with an Acme thread screw (ACME) would allow for a smaller motor as both torque and inertia requirements are lower while requiring less energy to move a load over an example distance of 20 mm. But, it is seen that as the lead gets larger the number of revolutions required to move the example drops, and the energy decreases because energy is a function of torque and revolutions.

2.7 Conclusion

To incorporate sustainability into axiomatic design, thirteen hypothetical sustainability axioms were proposed. The sustainability axioms were organized into metric-based axioms and lifecycle-based axioms. And a discussion was started to narrow down the useful sustainability axioms and those that might be functional requirements or system constraints. And a lead screw selection was performed using sustainability axiom 2 as a demonstration of the usefulness of the method.

Similar to how the axioms of axiomatic design were first proposed, the sustainability axioms here will need to be modified, rewritten, removed and added to until a true set is found. This will be done through application and example problems to identify if it is possible for the presented axioms to be violated or proven false; and the corollary, to prove the axioms true, is not possible. Thus, future work includes applying the various hypothetical sustainability axioms to identify an applicable axiom and eliminate non-axioms. Additional work using the application of sustainable machine tool design is an area for additional research to be performed. Furthermore, nearly all previous work has used axiomatic design to investigate sustainable design considerations but has lacked integrating sustainable concepts into the methodology. Thus, further methodology development to infuse sustainability into axiomatic design is needed.

Chapter Three: A Tool to Assess Embodied Energy of Electric Motors Used in Machine Tools

By

Ian C. Garretson, Barbara S. Linke

To be submitted to *Journal of Manufacturing Science and Engineering*

https://asmedigitalcollection.asme.org/manufacturingscience

Chapter 3: A Tool to Assess Embodied Energy of Electric Motors Used in Machine Tools

3.1 Abstract

Energy consumption in unit manufacturing process and machine tools is of interest. Energy consumption of a process can in part be determined from the energy consumption of the motors. Determining the manufacturing phase energy impacts for a machine tool can be a daunting task, the following work provides a streamlined method to determine the energy impacts of an electric motor. The method allows for embodied energy determination using limited available data, motor power and length. The method is demonstrated using the example of eliminating a pump motor from a machine tool, and replacing that pump with a gravity fed system.

3.2 Motors and Drives

Electric motors, drives, and servos are all related pieces of electro-mechanical machines. Feed drives are made up of some core components, this includes a controller, an electric motor, positional feedback electronics, and the mechanical components. The controller can be something similar to a personal computer, an Arduino, or a programable logic controller (PLC) system; each of these have differing capabilities and can be used in combination depending on the complexity of the machine tool. The positional feedback device can be sophisticated like a glass scale or simple like a linear potentiometer; when a rotary encoder is paired with an electric motor, this is termed a servo motor and combines the two functions. From (Chapman, 1999), electric machinery can be subdivided as either AC or DC machines and as synchronous or asynchronous. Most feed drives will be synchronous machines, as there is a need for positional accuracy, and either AC or DC.

3.3 Theoretical Life Cycle Assessment of an Electric Motor

To determine the trade-off in lifecycle energy consumption of a pump motor and a stand, the following theoretical lifecycle energy estimation is undertaken. This LCA estimates energy consumption to produce the materials to manufacture an electric motor. A majority of the equations described herein are applicable to 3 phase induction motors, and should be assumed unless otherwise noted. Additionally, this section investigates fractional horsepower motors to improve model fitting for these smaller motors, similar steps could be taken for larger motors. The section is as follows, first identifying motor mass from power or torque, second estimating motor losses, and third estimating manufacturing energy requirements based on constituent materials.

3.3.1 Step 1. Estimate Motor Mass from known power or torque:

The goal in this first step is to estimate the motor mass given a known motor power or torque or from or from the motor volume. The reasoning here is not to provide highly detailed calculations for motor sizing, but rather rule of thumb method for individuals that are not electric motor designers.

A prescriptive sizing method exists, which related motor torque to volume and magnetic shear stress and has been presented by several authors, (Miller, 1989) (p.20-32), (Soong, 2008), and (Veltman et al., 2016) (p. 21-23). Following (Veltman et al., 2016), if r is the radius and l is the length of a rotor that holds n wires d thick, F is the resultant force on the rotor, then the torque T_c output by the motor can be seen in Equation (3.1).

$$T_c = rF \approx kBj\pi r^2 l \quad (3.1)$$

Where the rotor volume $V_r = \pi r^2 l$, k is a constant equal to *2d* (in a simplified example), *B* is the magnetic flux density, and $j = \frac{i}{A}$ is the current density, *i* the current, and *A* the wire cross section area. Magnetic flux density *B* is limited to less than 2.0 T in silicon steel due to a change in reulctance which causes magnetic flux saturation. Current density *j* is limited to less than 10 A/mm^2 due to thermal limtations. The rotor volume can be estimated using this relationship, but unless an understanding of general motor specifications this might proove challenging. Another method does provide an option for estimating motor volume using Equation (3.2) from (Miller, 1989) by calculating the rotor volume using the torque to rotor volume (*TRV*); the TRV is typically 1.4-4 kNm/m^3 for fractional TEFT motors, 15-30 kNm/m^3 for integral TEFC motors, and 20-45 kNm/m^3 for high-performance industrial servos.

$$TRV = \frac{T}{V_r} \quad (3.2)$$

The overall size of an electric motor is directly related to stator volume V_s, which is proportional to rotor volume, as seen in Equation (3.3), where *srs* is a constant in the order of 0.6 (Veltman et al., 2016).

$$V_s \approx \frac{V_r}{srs^2} \quad (3.3)$$

This method described does provide an estimate of the motor volume fairly close to real values (Veltman et al., 2016), but the challenge encountered is a lack of understanding of selecting the correct values (*B, j, TRV*, shear stress, etc.) for the previous equations. An alternative method, is

to estimate motor mass from the torque or power using manufacturer data. Motor mass was estimated from motor power by (Mueller and Besant, 1999) in Equation (3.4) and motor mass was estimated from motor torque by (Mueller et al., 2004) in Equation (3.5).

$$M = 0.065 \cdot 0.8^{P} \tag{3.4}$$

$$M = 0.659 + 1.792 \cdot 0.8388^{\tau} \tag{3.5}$$

The equations from (Mueller and Besant, 1999) and (Mueller et al., 2004) provide estimations of motor mass for four pole induction motors; but more accurate estimates can be made by performing the fits ourselves. Using data from (Ferreira et al., 2016), provided from WEG (WEG, 2015), seen in Figure 3.1, Equations (3.6) and (3.7) are fitted from the data below for general purpose 3 phase induction motors. Utilizing a CAD model or disassembling a motor would be more accurate, but this is undertaken assuming that information is not available.

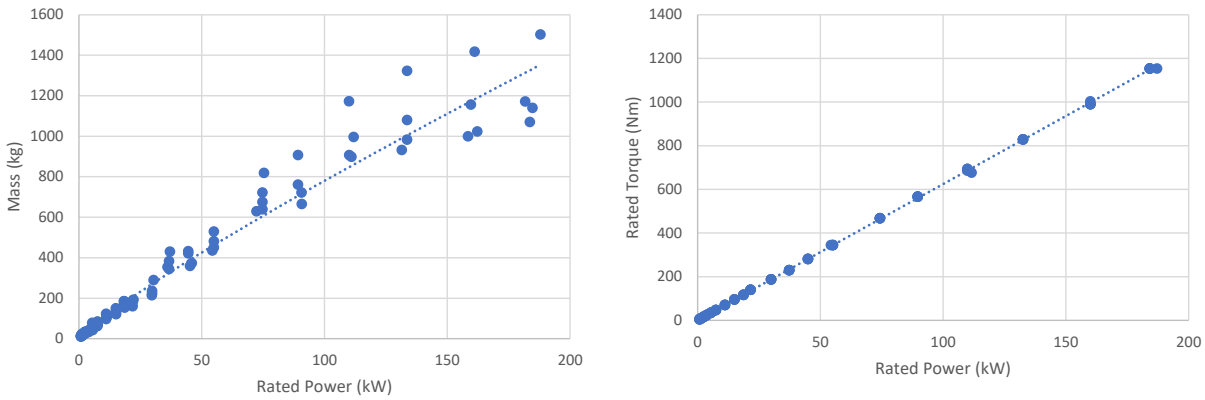

Figure 3.1: Motor mass and motor torque from rated power, data from (Ferreira et al., 2016), and (WEG, 2015)

$$M = 13.98 \cdot 0.87^{P} \qquad R^2 = 0.98 \qquad (3.6)$$

$$T = 6.23P + 1.29 \qquad R^2 = 0.99 \qquad (3.7)$$

A six kilowatt motor can then be estimated to weigh 68.39 kg and 68.83 kg using both (Mueller and Besant, 1999) and (Ferreira et al., 2016) respectively. A question arises, if a LCA practitioner has access to the motor, why not look up motor specification with the manufacturer? The reasons are threefold, first some motors are older and exact specifications are not known, or second manufacturers no longer provide information on older models, or third to reduce time spent researching individual components while performing an LCA.

3.3.1.1 Mass and power of fractional horsepower induction motors

Electric motor companies list motor power and mass data for a wide array of motor types in their catalogues. Equations for fractional horse power general purpose motors, pump motors, and servo motors are fitted here to provide a better estimate of their mass given their power; using data from (ABB, 2018a). Equations (3.8), (3.9), and (3.10) are for fractional horse power (HP) general purpose induction motors.

$$M = 20.3 \cdot P^{0.474} \qquad R^2 = 0.6 \qquad (3.8)$$

$$M = 0.146 \cdot P^{0.208} \cdot C^{1.922} \qquad R^2 = 0.81 \qquad (3.9)$$

$$M = 4.209P + 3.552C - 29.183 \qquad R^2 = 0.79 \qquad (3.10)$$

Where *M* is the mass of the motor in kilograms, *P* is the rated power in kilowatts, and *C* is the total length (including rotor shaft) in inches. It can be seen that incorporating the motor shaft length

greatly increases the coefficient of restitution (R^2) and as seen in Figure 3.2, provide variance in mass given variance in the motor dimensions at a specific rated power.

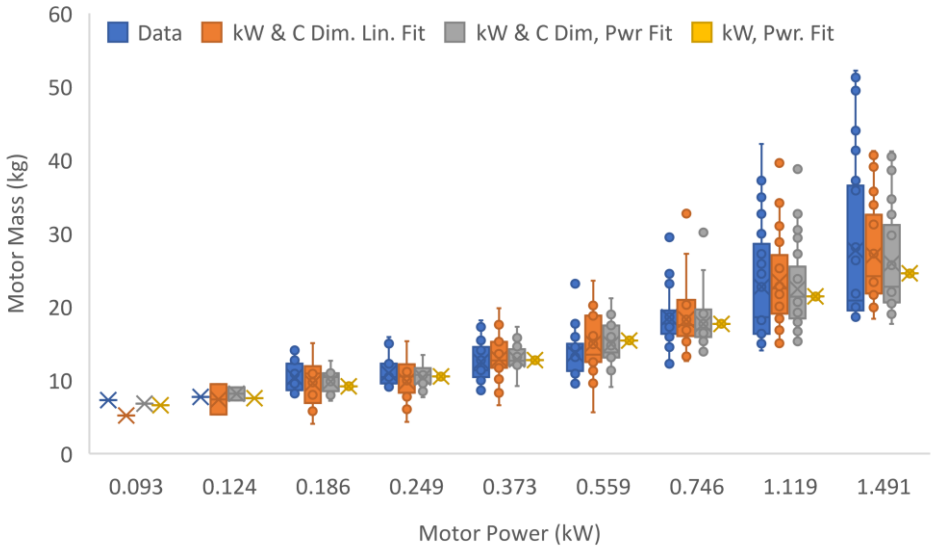

Figure 3.2: Comparison between manufacturer data and fit equations estimating motor mass from KW, fractional HP general purpose 3P motors (ABB, 2018a). Where blue is manufacturer data, yellow is Eq. (3.8), Grey is Eq. (3.9), and Orange is Eq. (3.10).

Variation in motor masses are derivative of motor dimensions, housing types, and mounting types. Housing types include totally enclosed foot mounted, totally enclosed C-face foot mounted, totally enclosed C-face footless, open drip proof (OPD) foot mounted, ODP C-face foot mounted, and ODP C-face footless. Full load amperage was also fitted, but was found to be less correlative to mass. A map of the motor mass given length and power was created using Equation (3.9) and is shown in Figure 3.3. This demonstrates the relative importance of the motor dimensions relative to the motor power for fractional HP motors.

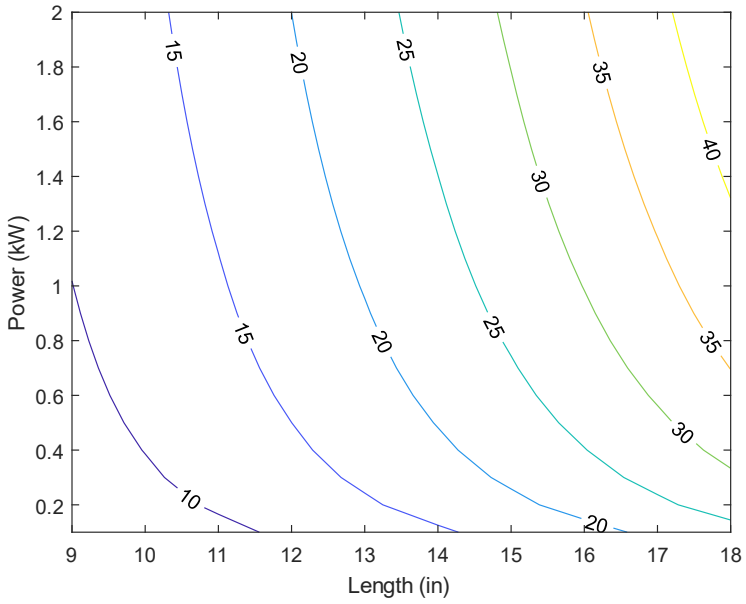

Figure 3.3: Mass (kg) of an IM motor given power and length, plotted using Eq. (3.9)

3.3.1.2 Mass and power of fractional horsepower servo motors

Some manufacturing applications, e.g., machine tools, will use servo motors in place of induction motors for accuracy and control performance benefits over induction motors. Servo motors notably have a feedback control mechanism, a rotational encoder, built into the motor that sends a position and speed signal back to the motor driver. Servo motors are typically either permanent magnet synchronous AC motors (PMSM) or brushless DC motors (BLDC); both PMSM and BLDC exhibit no slip, are highly efficient, and are low maintenance.

In Equation (3.11) mass data was fitted to motor power for BLDC fractional HP servo motors with data from (ABB, 2018b). Note, that the selection of servo motors is smaller than the selection of IM motors. Equation (3.11) was plotted against the motor data in Figure 3.4.

$$M = 4.531 \cdot P^{1.011} \qquad R^2 = 0.95 \qquad (3.11)$$

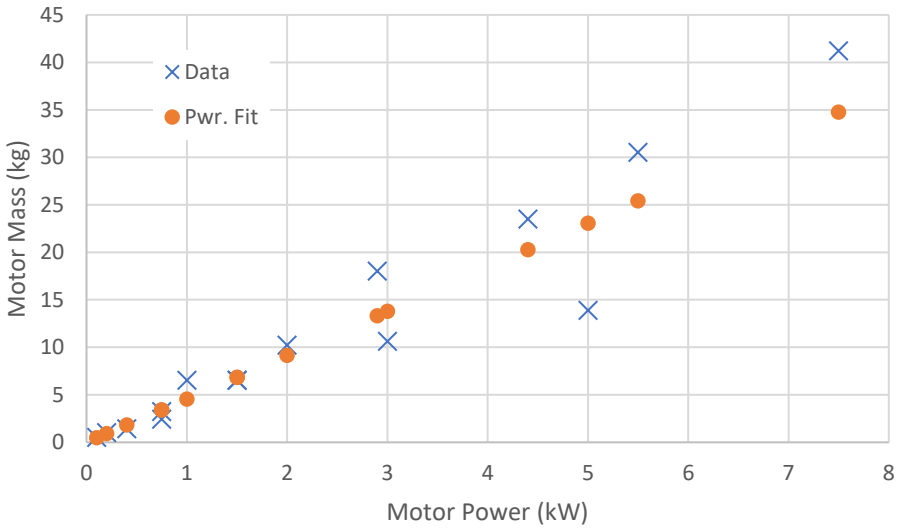

Figure 3.4: BLDC Fraction HP servo motors, data and fitted power equation (3.11). Data from (ABB, 2018b).

In Equation (3.12) motor mass for PMSM servo motors is fitted to both motor power *P* and motor length *C* using a power fit using data from (Yaskawa, 2020). Figure 3.5 shows the fit of the Equation relative to the manufacturer's data. Note in Figure 3.5, the motors can have two different masses for a single motor power rating. This was accounted for by including the length of the motor in Equation (3.12).

$$M = 0.017 \cdot P^{0.592} \cdot C^{1.056} \qquad \text{R2 = 0.98} \qquad (3.12)$$

Both Figure 3.6 and Figure 3.7 show the map of the motor power, length, and mass for PMSM motors from Yaskawa. Figure 3.6 shows the relationship for masses from 10 kg up to 80 kg, while Figure 3.7 shows a range of masses from 50 kg up to 250 kg. These maps would simplify estimation of mass by allows practitioners to read the graph rather than compute the equations.

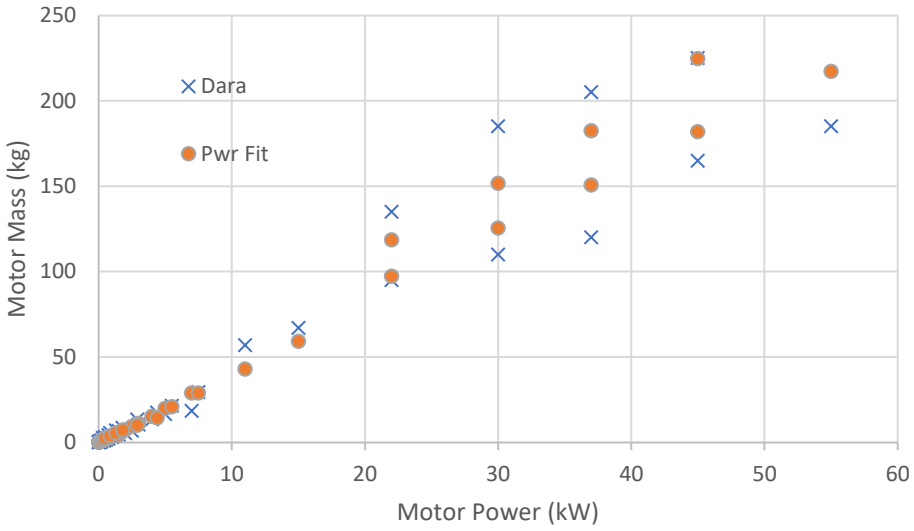

Figure 3.5: PMSM servo motors, data and fitted power equation. Data from (Yaskawa, 2020); Plotted using Equation (3.12)

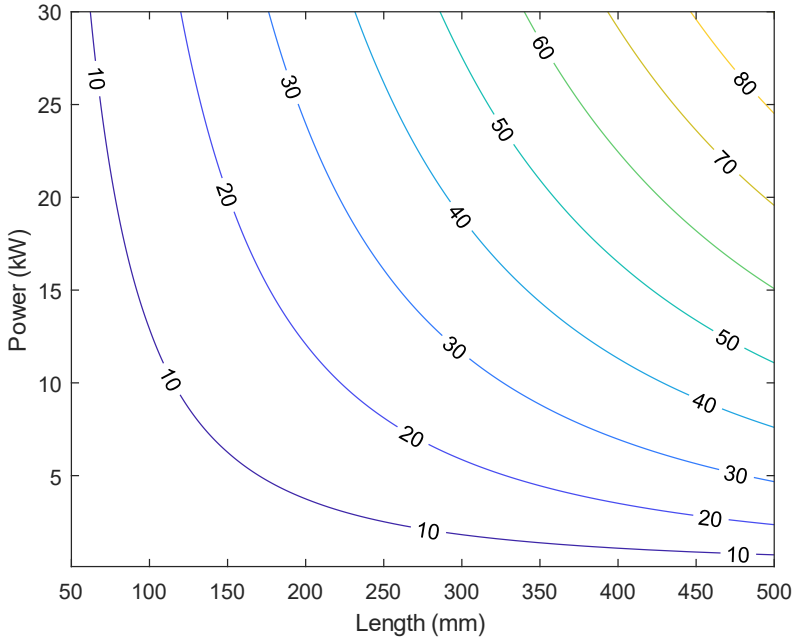

Figure 3.6: Mass (kg) of a servo motor given power and length; plotted using Plotted using Equation (3.12) with power range 0 to 30.

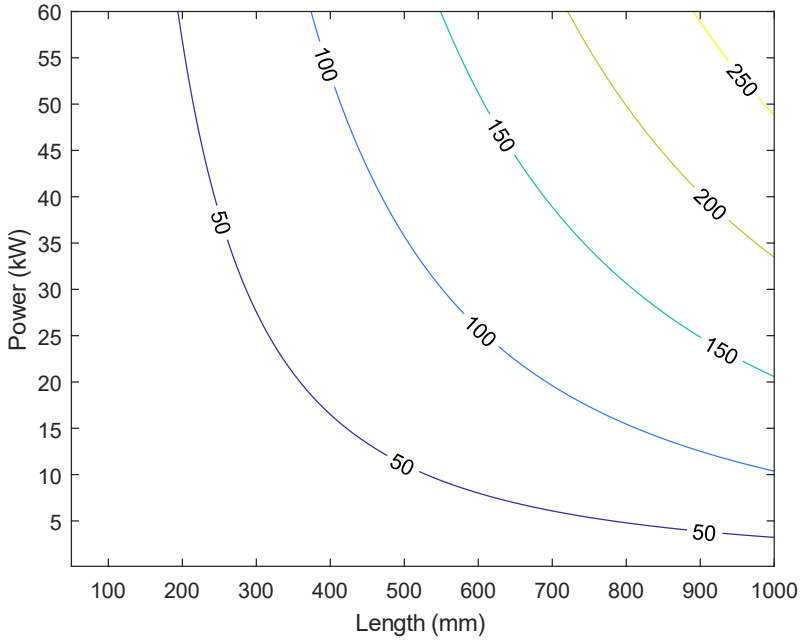

Figure 3.7: Mass (kg) of a servo motor given power and length; plotted using Plotted using Equation (3.12) with power range 0 to 60.

3.3.1.3 Mass and power of Fractional HP jet pump motors

Fractional HP jet pump motor masses M were also fitted to power P and length C for the pump comparison to be seen later in the chapter. While the equations from (Mueller and Besant, 1999), (Mueller et al., 2004) or (Ferreira et al., 2016) could be used for this application, since jet pump motors are AC induction machines, a more accurate estimation of mass is made by focusing on the pump motor data from (ABB, 2018a). Figure 3.8 shows a visual comparison of the fits of Equations (3.13), (3.14), and (3.15).

$$M = 16.61 \cdot P^{0.388} \qquad R^2 = 0.78 \qquad (3.13)$$

$$M = 0.056 \cdot P^{0.184} \cdot C^{2.194} \qquad R^2 = 0.88 \qquad (3.14)$$

$$M = 2.838P + 2.819C - 24.24 \qquad R^2 = 0.85 \qquad (3.15)$$

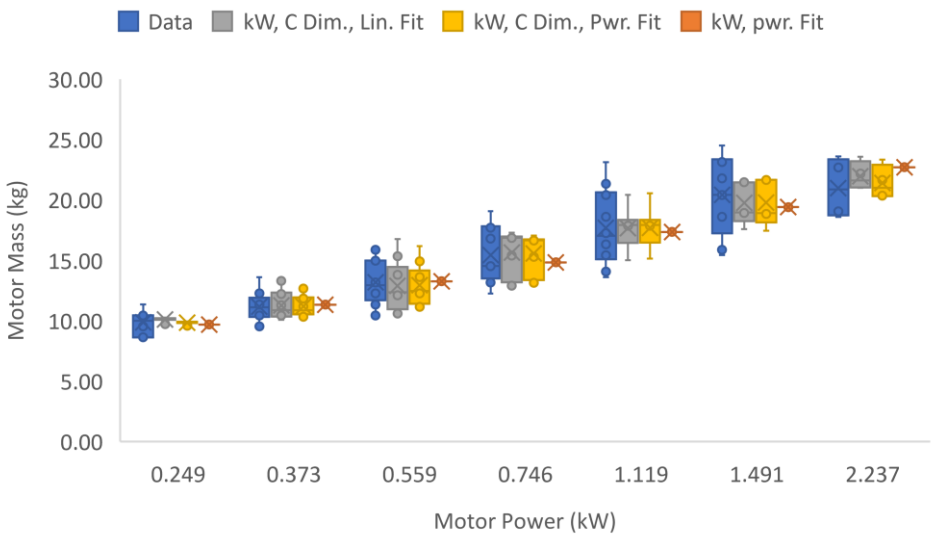

Figure 3.8: Fraction HP jet pump motors, data and fitted equations. Data from (ABB, 2018a). Where orange is Eq. (3.13), yellow is Eq. (3.14), and grey is Eq. (3.15).

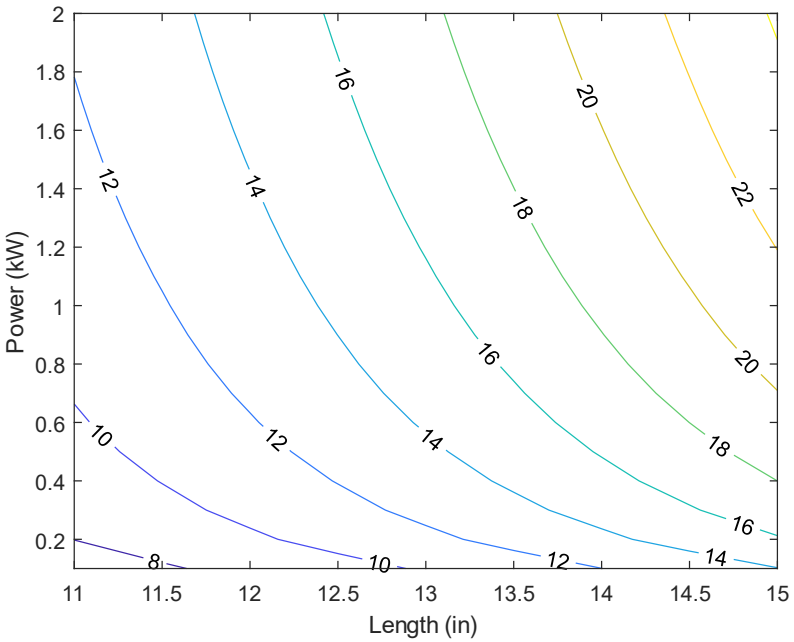

Figure 3.9: Mass (kg) of a pump motor given power and length, plotted using Eq. (3.14).

Figure 3.9 provides a map of the relationship between power, length, and motor mass using Equation (3.14). This type of graph can simplify the investigation of motor mass by an LCA practitioner allowing the use of the graph in place of the equation.

3.3.2 Step 2: Calculate Motor Losses

McCory and Douglass provides a very straight forward method for motor selection (McCoy and Douglass, 2014). They highlight a key misconception of motor sizing – that downsizing an under-loaded a motor will result in efficiency improvements by selecting a motor that will operate closer to one hundred percent load. Efficiency gains are actually made by replacing an older standard class motor with a more efficient (and modern) premium class motor. This can be seen in Figure 3.10.

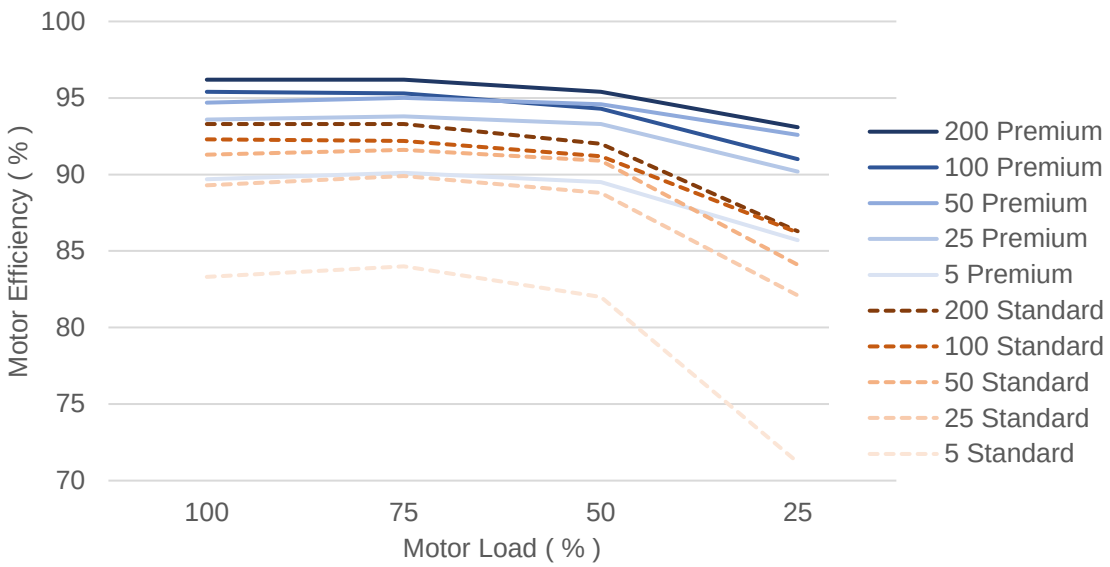

Figure 3.10: Motor efficiency (%), load (%), and power (kW) for standard and premium IM motors; data from (McCoy and Douglass, 2014)

Motor losses in electric machines include stator losses, rotor losses, iron losses, winding losses, friction losses, and additional losses. The cumulation of these losses lead to efficiency reductions up to 30 percent as seen in Figure 3.10. These losses are graphed in Figure 3.11 as a percent of total losses.

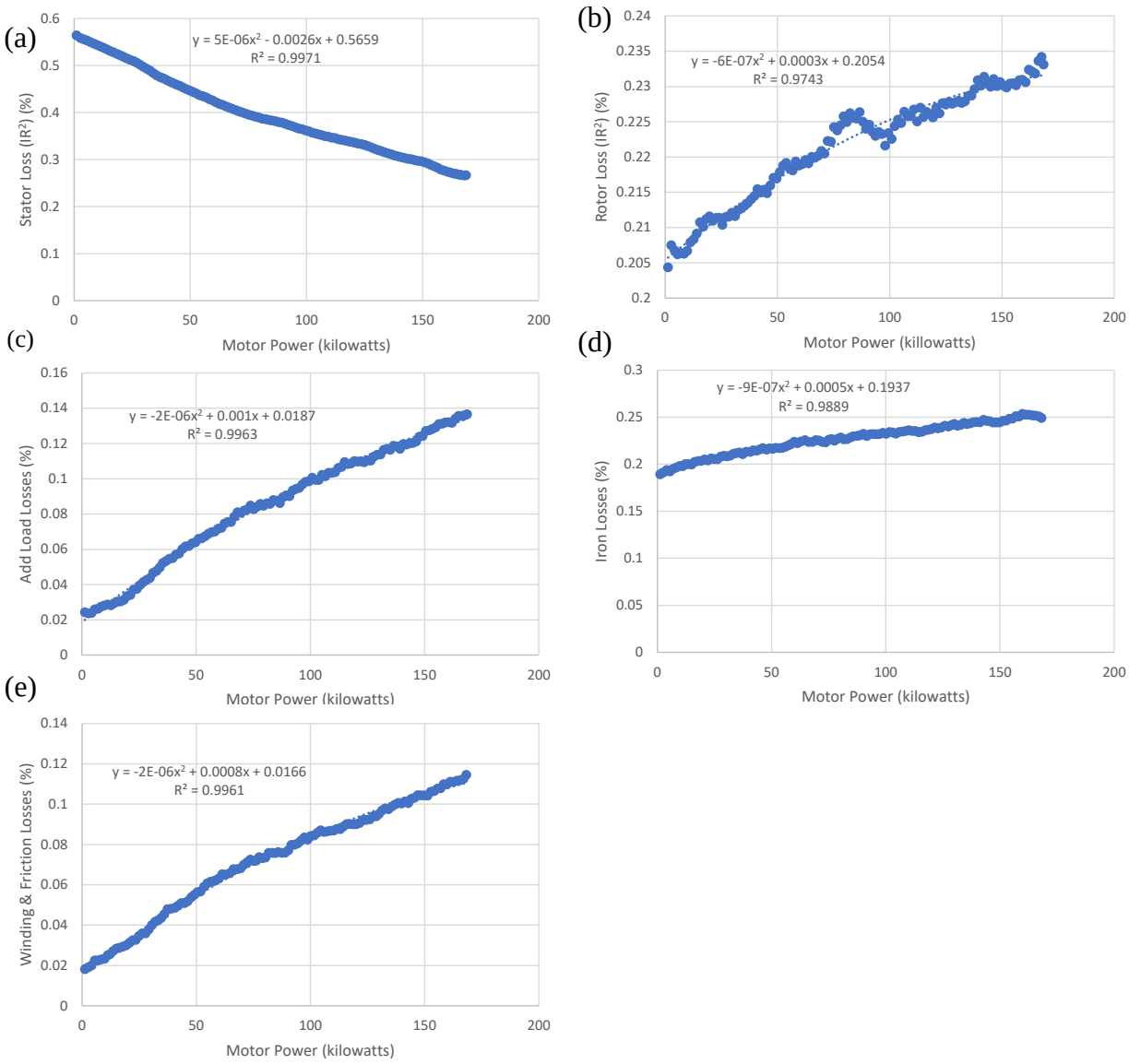

Figure 3.11: Estimated Motor Losses and fitted equations. (a) stator losses, (b) rotor losses, (c) add load losses, (d) iron losses, (e) winding & friction losses. From (de Almeida et al., 2014).

Following Figure 3.11, from (de Almeida et al., 2014), fractional losses of 4-pole induction motors were fitted as a quadratic function shown in Equation (3.16) with the coefficients in Table 3.1.

$$PercentLosses = aP^2 + bP + c \tag{3.16}$$

Table 3.1: Coefficients used to calculate percent losses of a motor, fitted from Almeida 2014.

	Stator I^2R	Rotor I^2R	Stray Load	Iron Core	Winding & Friction
a	4.87025E-06	-6.29219E-07	-1.68376E-06	-9.24101E-07	-1.67907E-06
b	-0.002552991	0.000261408	0.000966755	0.000492258	0.000840637
c	0.565862591	0.205410251	0.018714569	0.193747665	0.01660451

Some losses can be calculated directly following the method described in (Chapman, 1999), for example in 3 phase induction AC motors, input power is estimated using the total voltage and total current with Equation (3.17):

$$P_{in} = \sqrt{3} V_T I_L cos\theta \tag{3.17}$$

The power after the stator and copper losses is calculated using the armature current and resistance, or the equivalent circuit current and resistance at position 1 (Chapman, 1999) (p. 375) in Equation (3.18):

$$P_{in} = 3I_A^2 R_A = 3I_1^2 R_1 \tag{3.18}$$

The airgap (gap between stator and rotor) power is then calculated with Equation (3.19), which also is represented as the power calculated at position 2 in the equivalent circuit diagram of (Chapman, 1999) (p. 375):

$$P_{AG} = P_{in} - P_{SCL} = 3I_2^2 \frac{R_2}{s} \tag{3.19}$$

The converted power is then the airgap power accounting for the efficiency loss caused by the motor slip (s) in Equation (3.20):

$$P_{conv} = (1 - s)P_{AG} = \tau_{ind}\omega_{in} \tag{3.20}$$

Finally, the output power is then difference between the converted power and the total rotational losses, as seen in Equation (3.21), where rotational losses include friction and winding losses $P_{RCL} = 3I_R^2 R_R$, iron core losses $P_{core} = 3E_1^2 G_C$, and stray losses which are typically 1% (Chapman).

$$P_{out} = P_{conv} - P_{rot} = \tau_{load}\omega_{in} \tag{3.21}$$

Lastly, additional motor efficiency and output power equations are described in other literature, including (Torrent et al., 2012). And motor efficiency can be estimated from motor power in kilowatts using a fitted equation from (Mueller and Besant, 1999) in Equation (3.22); or from motor torque in Newton-meters from (Mueller et al., 2004) using Equation (3.23):

$$Eff = 0.3 + 0.69 \cdot e^{\frac{-5.75}{P^{0.4}}} \tag{3.22}$$

$$Eff = \left(1.0187 + \frac{0.3149 \cdot \tau^{1-0.4515}}{\tau}\right)^{-1} \tag{3.23}$$

3.3.3 Step 3: Select Motor Type and Calculate Constituent Material Masses from BOM

To estimate the embodied energy within an electric motor, the constituent materials must be known because each different material carries a different embedded energy. If the motor that is being assessed is not available for disassembly, then we must estimate its constituent materials. To do so, a literature review of papers that identify constituent materials was performed and the data extracted can be seen in Table 3.2.

Table 3.2: Electric Motor Constituent Material Mass Percentages; data from (Andrada et al., 2012; Boughanmi et al., 2012; Ferreira et al., 2011; Mueller et al., 2004; Mueller and Besant, 1999; Nordelöf et al., 2019b; Orlova et al., 2016)

Source	Muller 1999	Muller 2004	Ferreira 2011	Ferreira 2011	Ferreira 2011	Boughanmi 2012	Andrada 2012	Andrada 2012	Andrada 2012	Orlova 2016	Orlova 2016	Orlova 2016	Nordelf 2019	Nordelf 2019	Nordelf 2019
								Eff1/IE2				PM Syn	PMSM	PMSM	PM Syn RM
Motor Type	IM	IM	IM	IM	IM	IM	Eff3 IM	IM	8/6 SRM	IM	Syn RM	RM	(Nd(Dy)FeB)	(SmCo)	(Sr-ferrite)
Motor Power	0.1-1000	-	1.1 kW	11 kW	110 kW	10 kW	1.5 kW	1.5 kW	1.5 kW	10 kW	10 kW	10 kW	20-200 kW	20-200 kW	20-200 kW
Material	(%)	(%)	(%)	(%)	(%)	(%)	(%)	(%)	(%)	(%)	(%)	(%)	(%)	(%)	(%)
Electrical Steel	40%	40%	39.2%	42.6%	38.5%	45.5%	39.8%	42.3%	39.9%	47.6%	52.6%	52.1%	45.3%	46.0%	44.0%
Other Steel	10%	10%	10.9%	11.2%	8.3%	42.6%	11.1%	8.5%	8.1%	12.6%	3.2%	3.1%	6.1%	6.0%	6.1%
Cast Iron	30%	32%	18.1%	15.4%	37.2%										
Aluminum			12.3%	10.6%	2.2%	3.6%	26.0%	25.8%	24.0%	17.2%	19.3%	19.1%	32.1%	31.2%	31.6%
Copper	8%	9%	9.0%	7.6%	6.7%	5.8%	9.1%	10.0%	13.4%	8.5%	9.9%	9.8%	10.9%	10.9%	11.2%
Insulation Material		9%	0.4%	0.2%	0.1%	0.7%	0.4%	0.3%	0.1%	0.3%	0.3%	0.3%	2.8%	2.7%	2.8%
Permanent Magnets												1.1%	2.8%	3.1%	4.3%
Impregnation Resin			2.2%	1.2%	0.6%	1.4%	2.2%	2.2%	1.1%	1.3%	0.7%	0.7%			
Paint			0.7%	0.6%	0.1%		0.3%	0.3%	0.3%	0.7%	0.5%	0.5%			
Packing Material			7.3%	10.6%	6.2%		7.6%	7.3%	8.0%	11.9%	13.6%	13.4%			
Plastic						0.4%	2.0%	1.9%	3.0%						
Electronics							1.5%	1.4%	2.2%						
Other	12%														
Total Percent	100.0%	100.0%	100.0%	100.0%	100.0%	100.0%	100.0%	100.0%	100.0%	100.0%	100.0%	100.0%	100.0%	99.9%	100.0%

An interesting note, over time the data contained in each paper has become more detailed. The table displays material percentages that sum to 100 for different studies, and it includes several motor types and sizes. Most are induction motors (IM), and additionally synchronous reluctance motors (Syn RM), permanent magnet synchronous reluctance motors (PM Syn RM), permanent magnet synchronous motors (PMSM) are included.

To then determine the energy requirements of a motor, the energy requirements for producing each of the materials shown in Table 3.2 are then shown in Table 3.3.

Table 3.3: Energy Requirements for Constituent Materials Used to Evaluate the Example Electric Motor; data from (Engelbeen, n.d.; M. Li et al., 2018; McHenry and Laughlin, 2014; Nawaz and Tiwari, 2006; Nordelfof et al., 2016; Nordelöf et al., 2018; Norgate et al., 2007; van der Voet et al., 2013)

Material	MJ/kg	Reference
Electrical Steel	27	van der Voet 2013, Nawaz 2006, McHenry 2014
Other Steel	23	Norgate 2007
Cast Iron	20	Norgate 2007
Aluminum	211	Norgate 2007
Copper	60	van der Voet 2013
Insulation Material	84	Nordelf 2016
Nd(Dy)FeB Permanent Magnets	52	Nordelf 2016, p.42, table 25
SrCo Permanent Magnets	35	Nordelf 2019, p. s21, table s15
Strontium-Ferrite Permanent Magnets	53	Nordelf 2019, p. s26 Table s19
Impregnation Resin	23	Nordelf 2016, Calculated
Paint	20	Nodelf 2016, p.65, table 68
Packing Material	13	Li, 2019
Plastic	84	Englebeen, 2007
Electronics	32	Nordelof 2019, Calculated

Of note, the minute difference between electrical steel and other steel. Electrical steel typically is an alloy with low carbon percent and 2 - 4.5 percent silicon; and embrittlement usually occurs at 2 percent silicon added (McHenry and Laughlin, 2014) (p. 1931). The silicon addition improves performance of the motors both reducing losses and improving magnetic softness. Thus, electrical

steel was estimated assuming embedded energy of iron/steel at 25 MJ/kg (van der Voet et al., 2013) and metallurgical grade silicon at 72 MJ/kg (Nawaz and Tiwari, 2006). Thus 2 % Si steel would be 26 MJ/kg, 4.5 % Si steel would be 27 MJ/kg, and Sendust (85% Fe, 9% Si, 6% Al) would be 40 MJ/kg.

3.3.4 Case Study of Pump Motor Embodied Energy Payback Period

The following case study uses the example of eliminating a pump motor used in a grinding machine by raising the grinding machine and using gravity to run the coolant though a filter and return it to a storage tank. The grinding machine and the coolant tank can be seen in Figure 3.12. Thus, by estimating motor mass using an equation from Section 3.3.1, selecting an appropriate material composition from Table 3.2, the energy consumption to manufacture a motor can be estimated using Table 3.3.

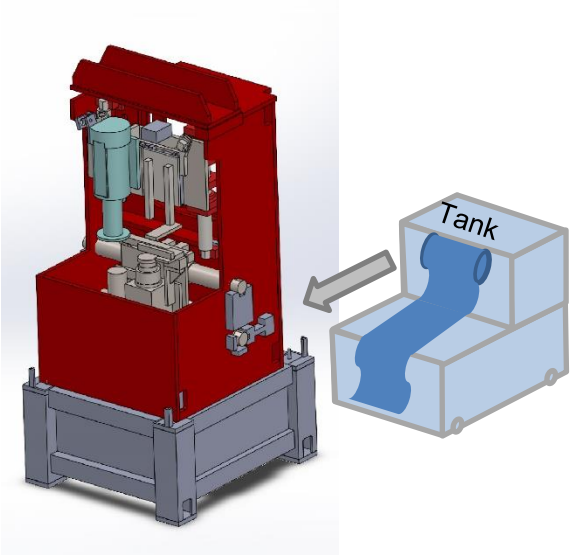

Figure 3.12: Hahn grinding machine tool on stand and the coolant tank.

An example using a 6-kilowatt (8 HP) IM motor is used for demonstration here, where the constituent mass is calculated Table 3.5. And, the energy used to manufacture the motor is

estimated in Table 3.6. Since this is an IM motor, one of the left columns will be used, and since the motor falls in between the 1.1 kW and 11 kW estimates from Ferreira the closer will be selected. Thus 3086 MJ of energy is used to produce the 6 kW motor. Similar examples can be carried out for ¼ HP, ⅙ HP, and ⅛, HP pump motors with energy consumption being summarized in Table 3.4

Table 3.4: Parameters and Energy to Produce Three Fractional Horsepower Pump Motors

	hp	kW	C Dim. (in)	kg	MJ
Graymills (1/4 hp)	0.25	0.19	14.875	15.36	873
Graymills (1/6 hp)	0.17	0.12	14.875	14.25	810
Flair (1/8 hp)	0.13	0.09	11.75	6.61	458

With the stand made of steel and weighting 377.5 kg, the energy to produce the steel in the stand is estimated to be 8682 MJ; this estimate does not include the welding energy. A comparison is now made between replacing the three fractional horsepower motors with a stand, as seen in Figure 3.13. This compares running the pump motors either continuously or on eight-hour workdays five days per week. Pump energy is estimated using the kilowattage size of the motor, and the breakeven time is calculated by first taking the difference between the energy to manufacture the stand and the pump, and then dividing the difference by the wattage of the motors.

The motors are assumed to run at their rated motor kilowattage, as this power would be higher than output power as described in Section 3.3.2. Motor efficiency was estimated to be 82.5% using Figure 3.10, and are assumed to be of standard efficiency class and operate at 50% load. In this example, a breakeven point can be made either under 2 years or after nearly 12 years and is influence by both the operating schedule and pump size.

.

Table 3.5: Electric Motor Constituent Masses (kg) of an Example 6kW IM Motor with a Total Mass of 68.83kg

Source	Muller	Muller	Ferreira	Ferreira	Ferreira	Boughanmi	Andrada	Andrada	Andrada	Orlova	Orlova	Orlova	Nordelf	Nordelf	Nordelf
	1999	2004	2011	2011	2011	2012	2012	2012	2012	2016	2016	2016	2019	2019	2019
Motor Type	IM	IM	IM	IM	IM	IM	Eff3 IM	Eff1/IE2 IM	8/6 SRM	IM	Syn RM	PM Syn RM	PMSM (Nd(Dy)FeB)	PMSM (SmCo)	PM Syn RM (Sr-ferrite)
Material	kg	kg	kg	kg	kg	kg	kg	kg	kg	kg	kg	kg	kg	kg	kg
Electrical Steel	27.53	27.53	26.95	29.29	26.47	31.35	27.39	29.10	27.46	32.78	36.24	35.85	31.18	31.66	30.29
Other Steel	6.88	6.88	7.49	7.73	5.72	29.30	7.62	5.82	5.56	8.65	2.19	2.17	4.20	4.13	4.20
Cast Iron	20.65	22.03	12.48	10.58	25.62										
Aluminum			8.49	7.32	1.54	2.51	17.92	17.76	16.49	11.84	13.25	13.11	22.09	21.47	21.75
Copper	5.51	6.19	6.19	5.21	4.61	4.00	6.29	6.90	9.20	5.83	6.80	6.72	7.50	7.50	7.71
Insulation Material		6.19	0.25	0.16	0.09	0.47	0.24	0.24	0.04	0.18	0.21	0.21	1.93	1.86	1.93
Permanent Magnets												0.73	1.93	2.13	2.96
Impregnation Resin			1.50	0.81	0.43	0.93	1.54	1.48	0.74	0.91	0.49	0.48			
Paint			0.50	0.41	0.09		0.21	0.20	0.22	0.46	0.31	0.31			
Packing Material			4.99	7.32	4.27		5.24	5.05	5.52	8.19	9.34	9.25			
Plastic						0.28	1.36	1.31	2.06						
Electronics							1.01	0.98	1.55						
Other	8.26														
Total Mass	68.83	68.83	68.83	68.83	68.83	68.83	68.83	68.83	68.83	68.83	68.83	68.83	68.83	68.76	68.83

Table 3.6: Energy (MJ) Required to Produce an Example 6kW IM Motor with a Total Mass of 68.83kg

Source	Muller	Muller	Ferreira	Ferreira	Ferreira	Boughanmi	Andrada	Andrada	Andrada	Orlova	Orlova	Orlova	Nordelf	Nordelf	Nordelf
	1999	2004	2011	2011	2011	2012	2012	2012	2012	2016	2016	2016	2019	2019	2019
Motor Type	IM	IM	IM	IM	IM	IM	Eff3 IM	Eff1/IE2 IM	8/6 SRM	IM	Syn RM	PM Syn RM	PMSM (Nd(Dy)FeB)	PMSM (SmCo)	PM Syn RM (Sr-ferrite)
Material	MJ	MJ	MJ	MJ	MJ	MJ	MJ	MJ	MJ	MJ	MJ	MJ	MJ	MJ	MJ
Electrical Steel	746.53	746.53	730.83	794.18	717.82	849.93	742.74	789.04	744.53	888.73	982.54	972.13	845.45	858.51	821.18
Other Steel	158.31	158.31	172.20	177.77	131.60	673.88	175.18	133.86	127.83	198.93	50.39	49.85	96.57	94.99	96.57
Cast Iron	412.98	440.51	249.56	211.53	512.38										
Aluminum		1790.38	1545.01	324.34	529.90	3781.91	3747.90	3479.34	2497.36	2796.31	2766.68	4661.92	4531.22	4589.31	
Copper	330.38	371.68	371.35	312.42	276.69	239.97	377.34	413.79	552.11	349.61	407.80	403.48	450.15	450.15	462.54
Insulation Material		520.35	20.96	13.67	7.17	39.07	20.54	19.78	3.09	15.30	17.44	17.26	161.89	156.11	161.89
Permanent Magnets												37.81	99.91	73.74	155.74
Impregnation Resin			34.72	18.86	9.90	21.56	35.64	34.32	17.07	21.11	11.31	11.19			
Paint			10.06	8.20	1.72		4.23	4.07	4.45	9.18	6.32	6.25			
Packing Material			66.30	97.26	56.72		69.61	67.03	73.34	108.84	124.12	122.81			
Plastic						23.44	114.46	110.21	173.14						
Electronics							32.76	31.54	49.98						
Other															
Total Energy	1648	2237	3446	3179	2038	2378	5354	5352	5225	4089	4396	4387	6316	6165	6287

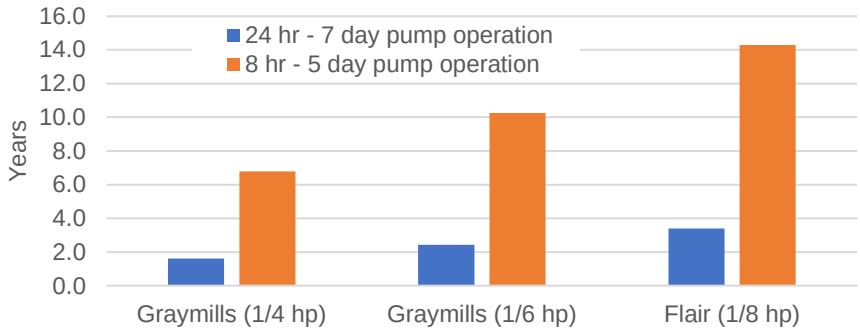

Figure 3.13: Breakeven Energy Comparison for Replacing Either a ¼, ⅙, or ⅛ HP Fractional Horsepower Motor with a Steel Stand; Comparison Includes Manufacturing and Operation of each Motor and Stand.

3.4 Conclusions

A Stand for a grinding machine tool was designed to raise the machine to replace a coolant pump to reduce the energy consumption of the machine. A method for estimating the embodied energy of a motor was described; and is summarized by estimating the motor mass given its power and length, then estimating the constituent materials from a literature review, then calculating the energy given the energy requirement for each material. An energy analysis was undertaken for the life cycle of both a pump motor and the machine tool stand to find the energy payback period. Depending on the operating schedule, and size of the pump, replacement could be highly beneficial to reduce energy consumption. The frequency of operation greatly determined the payback period for a given motor, where more frequently used pump motors are good candidates for replacement.

Chapter Four: Peak Power Load and Energy Costs Using the Example of the Start-up and Idling of a Grinding Machine

By

Henning Voet, Ian C. Garretson, Björn Falk, Robert H. Schmitt, Barbara S. Linke

Accepted and Presented at *Procedia CIRP, 25th CRIP Life Cycle Engineering (LCE) Conference*

https://www.sciencedirect.com/journal/procedia-cirp/vol/69/suppl/C

Chapter 4: Peak Power Load and Energy Costs Using the Example of the Start-up and Idling of a Grinding Machine

4.1 Abstract

Countries worldwide are experiencing changes in their electricity generating portfolio, from base load sources – coal or nuclear – to more sustainable but more volatile and intermittent sources – wind or photovoltaics. Industrial, high wattage consumers with machines that have frequent short-term peak power loads can cause grid failure when a demand peak coincides with an available power lull. These demand peaks are fulfilled by fossil-fuel-based peaking power plants. To avoid additional energy and cost expenditures of peaking power plants and reduce the lifecycle impact of production, peak demand needs to be mitigated. A procedure is proposed to reduce the peak loads of a grinding machine by controlling machine parameters. First, spindle energy and power data is measured while varying ramp up time to evaluate peak load and energy consumption tradeoffs. Then, a model is developed with three different objectives: minimize energy, peak power, or cost.

4.2 Introduction

World industrial energy consumption is expected to grow by 3.4% annually until 2040, and Organization for Economic Co-operation and Development (OECD) countries is 0.7% annually (USEIA, 2016a). In the United States, manufacturing consumes a third of the total energy produced (USEIA, 2016b), and in Europe, a quarter of the total energy produced (Eurostat, 2017). Historically, electricity has been produced using non-renewable energy sources, being either fossil

fuels (i.e. coal, natural gas, petroleum) and nuclear (Hodge, 2010). A majority of power plants deliver base load power that provide a constant power supply. Diesel generators and gas plants provide peaking power that meets a need above the base load. But over a decade, from 2005 to 2015, the installed electricity generation capacities of power stations in Germany and the US have shifted strongly to wind and photovoltaics; see Figure 4.1.

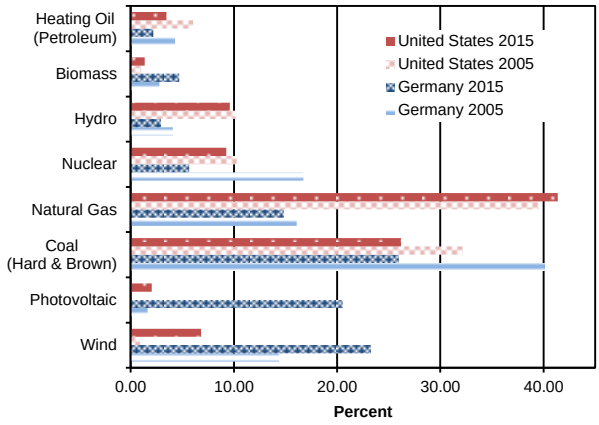

Figure 4.1: Electricity generating capacity of power plants in Germany and the United States – 2005 and 2015 – data from (Fraunhofer ISE, 2017; USEIA, 2016c).

Renewable energy plants, including wind and solar, are replacing some of the energy supply, but because the two are inherently intermittent and volatile, they are not able to provide as a baseload source, and can result in fluctuations in the grid. Due to the continuous increase of the volatile energy sources – wind and solar – energy as a resource is changing from an input with steady availability to an input with likelihood to perturb production (Reinhart et al., 2012). There are two technological solutions to avoid utilizing fossil-fuel-based power plants for phases when the electricity demand is high. The first is energy storage and includes batteries, fuel cells, capacitors, flywheels, compressed air, and pumped hydro (Vazquez et al., 2010). The second is for the demand to adapt to the supply, termed energy flexibility.

Energy flexibility is defined as “the ability of a production system to adapt quickly and with very little financial outlay to the changes in the energy market” (Reinhart et al., 2012). When manufacturing companies adapt their production to the availability of electricity from the grid, electricity disturbances can reduce the production output. Thus, manufacturing systems will become more complicated because all other target metrics like quality, time, and cost interact with energy. Popp et al. (2017) demonstrated the feasibility by simulating a factory that adapted to power variations from wind and solar power, and demonstrated a six percent average reduction in grid demand. It is likely that a combination of both energy storage and energy flexibility will be required.

The energy profile for traditional machining processes all have peak demand at startup, which is the work to accelerate the spindle to cutting speed. Li et al. (2011b) investigated energy consumption in two grinding machines, two lathes, and two milling centers; the peak power in their study ranged from 170% to 570% of the fixed power for the machine. Figure 4.2 demonstrates the initial, peak, and fixed power for various traditional manufacturing machines. As identified by Gutowski et al. (2006) grinding processes require more energy per kilogram processes (J/kg) than other machining processes; thus a grinding machine is investigated herein.

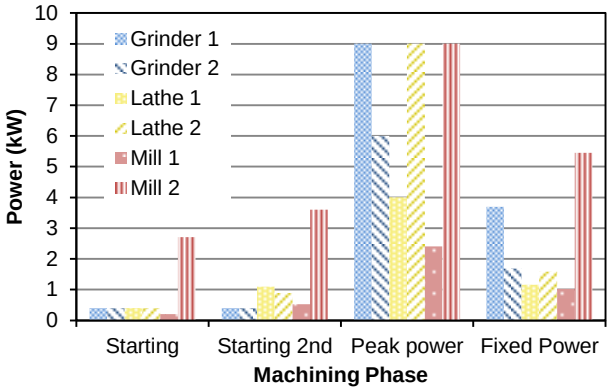

Figure 4.2: Start-up, peak, and fixed power. Adapted from (Li et al., 2011b).

In the context of sustainable manufacturing, defined as “the creation of goods or services using a system of processes that simultaneously addresses economic, environmental, and social aspects in an attempt to improve the positive or reduce the negative impacts of production by means of responsible and conscious actions” (Garretson et al., 2016b). Broadly, this indicates that impact reduction of a manufacturing facility is a sustainable action. Thus, reducing the power demand of a machine tool will reduce the environmental and economic impact of that machine by reducing the upstream impact of the power plant. Cumulatively flattening peak demands allows power plants to operate more efficiently, which reduces the upstream impacts of operating the machine tool. A more efficient power plant will reduce emissions (if it is fossil-fuel-based) and costs of operating the plant.

Several CIRP authors have previously investigated energy and power efficiency in machine tools. Aspostolos et al. (2013) identified energy-efficient planning could be accomplished by reducing idle time and periodic machine shutdowns. Humphrey et al. (2014) demonstrated the importance of measurement frequency in energy monitoring using a drilling process as an example. Suwa and Samukawa (2016) developed a method for optimizing energy efficiency for multiple machines by controlling machine processing modes (normal and fast) and operation scheduling. Tapoglou et al. (2016) minimized the energy consumption of a milling machine in real time by controlling processing parameters. Bohner et al. (2014) improved electric efficiency by performing peak load management for machine tools, resizing electric drives, and controlling operating mode. Hacksteiner et al. (2017) performed real time energy monitoring of a CNC turning and milling centers to evaluate process efficiency. Shabi et al. (2017) investigated energy consumption of the

cooling system of a machine tool, finding the systems are not well adapted for machine tools as they typically account for over 40 percent of the energy consumption during idle. Thus, while various aspects of machine tool electric efficiency have been investigated, spindle startup still is an applicable area for investigation.

In the following, the startup behavior of a grinding machine is examined more closely and the resulting changes in the peak power load and the resulting energy costs are analyzed.

4.3 Experimental Setup

The equipment and experiments are described below. The equipment includes both the operating machine and measurement tools. The experiments include an initial and main study.

4.3.1 Test Equipment Description

For the experiments, a 1½ hp Baldor Grinder 248-183TD Class B is used, which is controlled by a Bosch Rexroth variable frequency drive (VFD) EFC 3610. The Grinder is rated to run at a maximum 3600 RPM, and was verified to run at a maximum of 3570 RPM using a Cen-Tech 66632 Photo Tachometer. A Yokogawa CW240 power quality analyzer was utilized to collect power and energy data, and was attached before the VFD drive; the 3P3W2I setting was utilized as the VFD drive only uses two of the three phases for input power. Key experimental data includes current and voltage for both leads entering the VFD, and in addition the real (P), reactive (Q), and apparent (S) power entering the VFD. The VFD drive is capable of varying the time to deliver zero to full power from 0.1-6000 seconds. Through tests a minimum startup time of two seconds for this setup was identified.

4.3.2 Experiment: Variation of the acceleration time and measuring the peak power load

Two electric motor acceleration experiments were conducted. The first experiment was ran to determine a relative energy minimization curve for the electric motor, to find an area for further study. The initial study was not randomized, and three repetitions were run for each startup time ran. Energy and power data was collected for the following acceleration times: 2, 5, 10, 20, 40, and 60 seconds.

The second experiment included the following times: 2, 3, 4, 5, 6, 7, 8, 9, and 10 seconds. Five repetitions were ran for each time point, resulting in 45 data points. The prior, non-randomized experiment showed a trend that less energy was required for subsequent startups at the same time to start; thus the startup times were randomly sequenced. This experiment was randomized by listing each time point in sequence, assigning random numbers, and performing tests from low to high. All experiments are performed consecutively; only interrupted by short periods after five measurements in order to transfer measured data from the measuring device to an external storage device.

4.4 Results and Discussion

Both test series show that a significant reduction in the peak power and overall energy consumption can be achieved by controlling the acceleration time.

4.4.1 Energy Calculation

Energy was calculated from the power profile data collected for each spindle acceleration test. Power is defined in Equation (4.1) (Nilsson and Riedel, 2008).

$$p = \frac{dw}{dt} \tag{4.1}$$

Where p is the power in watts (W), w the energy in watt-seconds (Ws) and t the time in seconds (s). Energy is then calculated with Equation (4.2), where start-up time t_{UP} is the upper limit of the integral.

$$w\,(t_{UP}) = \int_0^{t_{UP}} p(t)dt \tag{4.2}$$

Thus the energy is described by the area under the power curve. Figure 4.3 displays the power demand profiles for two and nine seconds acceleration time.

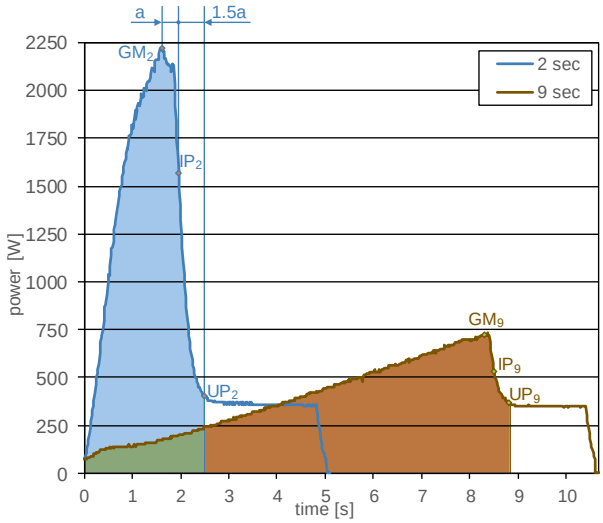

Figure 4.3: Real Power profiles of 2 and 9 sec acceleration times, demonstrating the energy integration profile using the global maximum (GM), inflection point (IP), and steady state time (UP).

Each power profile displayed in Figures 4 and 5 are individual profiles with the closest match to the average energy consumption of the five startups performed for each acceleration time. It is seen that the peak power demand (watts) decreases substantially when the acceleration time increases from two to nine seconds.

In the calculation of the energy consumption, the energy is counted until the Baldor Grinder has reached its operating speed of 3600 RPM. Figure 4.3 indicates how the energy consumption is calculated:

1. The distance (a) along the x-direction is set to be from the global maximum (GM_2) to the inflection point (IP_2).
2. The upper calculation point (UP_2) in the x-direction is set as IP_2 plus 1.5 a.
3. To smooth the variation a moving average of the power values is taken.
4. Energy is then calculated using Equation 2 by integrating from 0 to UP_2.

The described calculation procedure works for this specific machine based on the measured power profile and operating experience. When using the method for another machine, the adjustment of the a-value by 1.5 will have to be adapted. A moving average is applied to the power measurement curve prior to the energy integration because of large fluctuations in the power data. The moving average is applied to the specific point and includes five values before and after for a total of eleven points. Note that the method described results in marginal differences between the real startup time and the pre-set startup time.

4.4.2 Power Measurements and Energy Results

In the first experiment with startup times of 2, 5, 10, 20, 40, and 60 seconds it became apparent that the peak power loads increase when the startup time decreases. Whereas, energy consumption decreases from two to five seconds startup time then monotonically increased. So a minimum occurs between two and ten seconds; startup times up to 10 seconds are still be practical in everyday working operations, a much more detailed follow up experiment was carried out.

Figure 4.4 shows the power profiles used to calculate the energy for each acceleration time. As seen, peak power decreases as acceleration time increases.

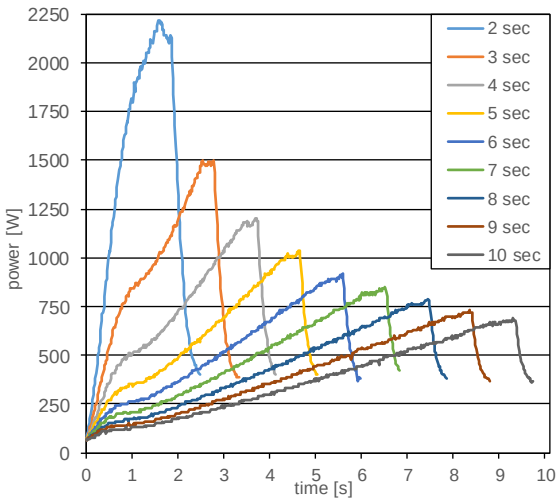

Figure 4.4: Power profiles of the Baldor Grinder for different acceleration times

Using the curve sections shown, the required acceleration energy is determined by the calculation of the area under the curve (see Equation (4.2)) and is shown together with the peak power load for the different startup times in Figure 4.5. The values displayed are averages and medians for the peak power load and energy consumption using the five measurements for each acceleration time.

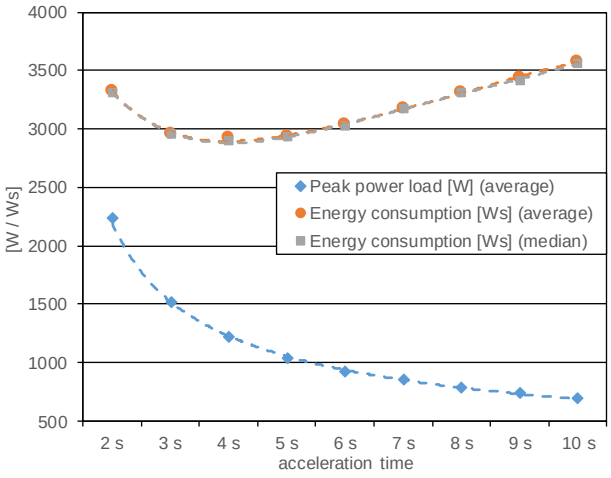

Figure 4.5: Peak power loads and energy consumption for different acceleration times

As acceleration time increases, the peak power loads decrease from near 2230 W (2 s) down to about 700 W (10 s). This reduces peak power load by about 69 percent. At 2 seconds, energy consumption is about 3325 Ws (average) or 3313 Ws (median) and decreases towards a minimum of 2925 Ws (average) or 2895 Ws (median) at an acceleration time of 4 seconds. This is a reduction of about 12 percent. Moreover, the peak power load decreases from a 2-second compared to a 4-second startup time by 45 percent. From 4 seconds, as the startup time increases, the energy consumption increases monotonically. Hence, a good solution with minimum energy and greatly reduced power with minor time inconvenience is a 4-second acceleration.

4.4.3 Cost Analysis

Industrial energy is priced using three metrics, energy charges ($/kWh), demand charges ($/kW), and power factor (PF) adjustment ($/kWh/%) (Pacific Gas & Electric, 2017). Energy charges are for the total use over the use period. Demand charges are the maximum power demand for a single month, where demand is measured as an average over a 15 minute interval (PG&E, 2007). Power

factor adjustment accounts for the phase angle shift between the current and voltage; see equation (4.3) from (Humphrey et al., 2014), where φ is the phase angle, subscripts *i* and *v* refer to current and voltage, *P* is real power, and *S* is apparent power.

$$PF = cos(\varphi) = cos(\varphi_i - \varphi_v) = \frac{P}{S} \tag{4.3}$$

The local power company records real power (*P*) and reactive power (*R*), and uses Equation (4.4) to determine power factor (PF) (PG&E, 2007). Note, the Californian electricity provider PG&E takes the PF as the monthly average and calculates as a penalty or credit of 0.06% for each percent below or above 85% (PG&E, 2007).

$$PF = cos(\varphi) = cos\left(arctan\left(\frac{R}{P}\right)\right) \tag{4.4}$$

Thus, a cost model is seen in Equation (4.5), and is used to calculate the contour lines see in Figure 4.6 and Figure 4.7.

$$C_T = (R_E * E + R_{PD} * PD_{15}) * \left(1 + R_{PF} * PF_{M,adj}\right) \tag{4.5}$$

Where *R* is a cost rate, and subscripts *E, PD,* and *PF* denote energy, demand, and power factor charges. Additionally, *E*, *PD*, and *PF* are the energy, power demand, and power factor; and their subscripts *M* and 15 denote either a monthly or 15-minute average, finally adj subscript denotes the power factor adjustment. Note, that peak day pricing (PDP) is omitted from the model, and is an additional demand charge when temperatures are above 98 ^{o}F (36.7 ^{o}C) (PG&E, 2010). Additional note, rates vary by time-of-use, max peak (12-18), partial peak (8:30-12 and 18-21:30),

and off peak (21:30-8:30) (Pacific Gas & Electric, 2017); time-of-use rates are not incorporated in the model due to short time scale. Equation 5 is to be minimized and is subject to Equations (4.6) and (4.7).

$$PD_{15} = max\left(\left(\frac{1}{n}\sum_{i=0}^{n-1} P_i\right)_i\right) \tag{4.6}$$

$$PF_{adj} = 0.85 - \ cos\left(arctan\left(\frac{R}{P}\right)\right) \tag{4.7}$$

These calculations are used in Equations (4.5) for the power demand (PD_{15}) and power factor (PF_M). Where n is the number of samples that are averaged and P_i is the instantaneous power for each element i. n is determined using the sampling frequency of the power quality analyzer (60hz). Equation (4.6), calculates the maximum value of the 15-minute moving average for the power demand. And Equation (4.7) is the power factor adjustment. The following values will be used assuming peak charges, from (Pacific Gas & Electric, 2017):

- $R_{E,\ Max}$ = 0.14244 ($/kWh)
- $R_{PD,\ Max}$ = 18.05 ($/kW)
- $R_{E,\ Off}$ = 0.08029 ($/kWh)
- $R_{PD,\ Off}$ = 0.00 ($/kW)
- R_{PF} = 0.00005 ($/kWh/%)

Equations (4.8) and (4.9) calculate energy (E_{15}) and peak power demand (PD_{AVG}) for a special use case, which includes many acceleration cycles, and were derived from the experiments monitoring energy consumption of the electric motor. Where energy is measured in watt-seconds, and power

demand in watts. And t_{ac} is the number of seconds required to accelerate the motor. The coefficient of determination (R^2) is at least 0.99 for both fitted equations.

$$E_{15} = 504683 \cdot t_{ac}^{-0.156} \tag{4.8}$$

$$PD_{Avg} = 560.71 \cdot t_{ac}^{-0.156} \tag{4.9}$$

Equation (4.8) is the total energy to accelerate the motor and idle for 20 seconds, repeatedly over a 15-minute interval as a function of acceleration time (t_{ac}). Note, that because the power demand cost is calculated as a 15-minute average, a time period of 15 minutes was selected for equation (4.8). And was calculated by repeating startup-cycles with a runtime of 20 seconds of the electric motor for a 15-minute period; e.g. 2 second startup would correspond to a 2.5 real startup (Fig.6) and with a 22.5 operation cycle would occur approximately 40 times in a 15 minute period. Equation (4.9) is average power demand as a function of acceleration time (t_{ac}). Equations (4.8) and (4.9) were used to solve for Equation (4.10). The solution of the fitted Equations (4.8) and (4.9) to Equation (4.10) match the theory of average power, see Equation (4.11), where ΔW is work performed, Δt is time, and P_{avg} is average power (Nilsson and Riedel, 2008). Equation (4.11) validates the power measurements.

$$E = 504638 \cdot \left(\frac{PD_{avg}}{560.71}\right) \approx 900\ (sec)\ \cdot PD_{avg} \tag{4.10}$$

$$\Delta W = \Delta t \cdot PD_{avg} \tag{4.11}$$

Equations (4.10) is used to determine the price of accelerating the electric motor in Figure 4.6 and Figure 4.7. The 15-minute energy interval is plotted against average power with cost contours (US

dollars) seen in solid lines using Equation (4.5). The dashed line is Equation (4.10) and is used to determine cost given the average power or total energy over a 15-minute period for using the grinder; which can be calculated from equations (4.8) or (4.9) using the time to accelerate the motor.

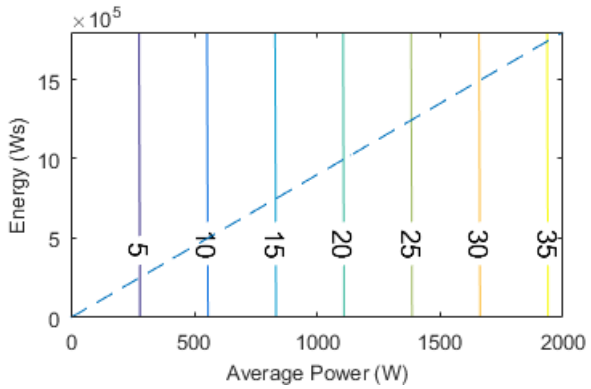

Figure 4.6: Max. peak costs in dollars (vertical lines), 15 minutes interval energy plotted against average power

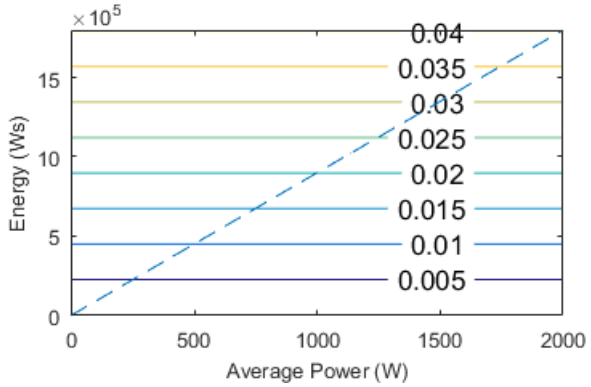

Figure 4.7: Off peak costs in dollars (horizontal lines), 15 minutes interval energy plotted against average power

While energy and instantaneous power have conflicting objectives and are minimized separately as trade-offs (see Figure 5); but because average power is used in electricity pricing no conflict

occurs between power and energy costs. Thus, cost is minimized by increasing the acceleration time. But, operationally there needs to be a limit on start-up time, work cannot be performed while waiting for a machine to turn on, as labor, overhead, and lost sales increases the costs of waiting. An individual start-up is minimized in Figure 5 at 4 seconds; the situation described here where several start-ups occur back-to-back is minimized at max startup time.

Additionally, the cost assessment for the study is limited because power pricing is on 15-minute averages and a single spindle startup that occurs in less than ten seconds is insignificant. A larger spindle with a larger grinding wheel would cause a larger power peak than the one used in the study. Future studies may not need to perform repeated operations like the one done here. Also noteworthy, as other authors identify that energy is wasted during idle time and push for machines tools to be turned off, this will increase the number of spindle starts in factories.

4.5 Summary and Outlook

Making manufacturing more sustainable is an important aspect of current research and industry trends. Various methods for improving sustainability include focusing on environmental, economic, and social aspects. This study focused on environmental and economic aspects by accounting for the electricity consumption of a spindle start of a pedestal grinder and the costs associated with the electricity.

The influence of the weather on electricity generation is growing in many national power grids and is inherently more volatile than power demand. As the electric profile becomes more volatile the pricing structure is likely to change, with benefits given to firms that can adapt to electric grid

fluctuations. As energy flexibility is incorporated into production, the tradeoffs between sustainability, costs, and the production schedule need to be analyzed. In each process step, the energy-, power- and cost savings, which has no direct negative influence on the product quality like the acceleration time of a grinding machine should be raised first.

In the considered startup of the grinding machine, the peak load decreases as the acceleration time increases. An absolute energy minimum is reached at a four-second-acceleration. The results show instantaneous power, and energy minimized in unison; but electricity pricing forces the costs for both energy and power to minimize monotonically as acceleration time increases. But the costing method used here is limited as it only incorporates electricity, and additional costs including labor, overhead, and lost sales would improve the model. Additionally, the electricity cost model has limited application because the time scale of spindle acceleration in seconds is much shorter than the 15-minute electricity pricing structure.

The presented results refer only to the startup and idle phase. In the next step, the experiments will be extended to the phase of component processing to be able to analyze interactions between the power load profile of the grinding machine and the product quality of the component. Since the product quality itself is part of the research, these analyses can even have more impact on the economic success of a company and thus are more critical. Moreover, future work includes developing first-principles-based models of the machine for power and energy calculation, expanding the cost model to include operator, overhead, and cost of lost productivity. While energy is not the only sustainability metric, it is easy to implement for industry practitioners as it typically results in costs savings; but other sustainability aspects should be addressed in follow-up projects.

Chapter Five: Energy Consumption and Workpiece Surface Roughness Tradeoff in a Grinding Machine: A Study with Cold Air Coolant

By

Ian C. Garretson, Malte Seibt, Robert H. Schmitt, Barbara S. Linke

To be submitted to *The Intentional Journal of Advanced Manufacturing Technology*

https://www.springer.com/journal/170

Chapter 5: Energy Consumption and Workpiece Surface Roughness Tradeoff in a Grinding Machine: A Study with Cold Air Coolant

5.1 Abstract

A trade-off between electricity consumption per kilogram and process rate kilograms per hour for different manufacturing processes has been determined, where electricity scales linearly upwards as process rate decreases below processing rates of one kilogram per hour. The authors contend that while finding such a trend helps to shape our understanding of manufacturing science, the finding leaves a need to relate energy consumption to output quality. This paper will then investigate surface roughness in relation to energy consumption of a grinding machine tool. Grinding experiments will be performed on hardened 440C stainless steel, a bearing material. Findings indicate that higher electricity and process work is required to achieve better workpiece quality in terms of lower surface roughness values.

5.2 Introduction

From 1998 to 2018, US gross manufacturing output has increased by 12 percent while manufacturing energy consumption decreased by 26 percent (US EIA, 2021), which implies a 20 year growth in energy efficiency. Furthermore, machine tools that utilize machine drives energy is estimated to be 2122 TBtus, and account for 19.6 percent of process energy used in manufacturing and with only 753 TBtus applied it is only 35.5 percent efficient (US EIA, 2019). Notably, the other categories of process energy, heating, cooling & refrigeration, electro-chemical, and other use are much more efficiency with 66.0, 65.9, 52.1, and 51.0 percent efficient respectively. This poor efficiency performance in machine drive manufacturing technology needs

investigation. Menghi et al. (2019) reviewed the energy efficiency method and tools used in manufacturing systems from between 2003 and 2018. The authors found both increasing frequency of studies in the nearer past and that researchers take a variety of system boundaries from factor or plant level down to machine level. For individual machines, Yoon et al. (2015) identified that energy saving strategies can be deconstructed into micro process planning, macro process planning, and the machine design level.

Gutowski et al. (2009) investigated the relationship between electricity consumption and processing rate on a unit kilogram basis. The authors had identified an interestingly linear relationship where electricity requirements (J/kg) increase by an order of 10 for a decrease in processing rate (kg/hr) by an order of 10, at processing rates under one kilogram per hour. But this investigation does not identify the relationship between quality and energy consumption. The following paper will investigate the tradeoff between energy consumption and surface roughness.

5.3 Literature Review

A majority of the literature that report the relationship between surface quality and energy consumption in machining were investigating dry machining conditions or minimum quantity lubrication (MQL) conditions.

Kwak et al. (2006) performed cylindrical grinding experiments on hardened SMC440 steel to investigate the effects of workpiece speed, and traverse speed on power and surface roughness. They found that in general, increasing either workpiece speed and traverse speed increased grinding power and surface roughness. Li et al. (2012) investigated grinding of two steels,

hardened 100Cr6 and non-hardened 16MnCr5, to determine the tradeoff between energy consumption and surface roughness. The authors found that surface roughness R_z (μm) both increased in magnitude and variation as specific energy consumption (kJ/cm^3) decreased; the authors related the two outputs using material removal rate (MRR cm^3/s). Priarone (2016) found that a vitrified bonded grinding wheel produced improved energy efficiency, where as a resinoid bonded wheel produced improved part quality. Furthermore, the author developed a method for selecting between the two in a tradeoff scenario.

Winter et al. (2015) compared specific energy consumption (W/mm) to surface roughness (R_a μm) for different cutting fluids, grinding oil, jatropha oil, mineral oil emulsion, polymer dilution, and glycerol dilution. The authors found that the cuttings fluids would either produce a high-quality surface or an improved energy efficiency but not both. Heinzel and Kolkwitz (2019) performed grinding experiments on hardened steel workpieces to compare different cooling fluid nozzles, a tangential flat nozzle to a modular nozzle in terms of specific energy (Ws/mm^3). The authors found that the tangential flat nozzle experiences improved energy efficiency at equivalent material removal rates.

Salonitis (2015) investigated energy consumption in grinding, and found that a majority of energy is used to maintain the process environment, and that reducing process duration would reduce process energy. Hacksteiner et al. (2018) found similar results, that cooling lubricant pumps and machine cooling account for a majority of energy consumption of the grinding machine, and that demand adjustments to cooling lubricant flow rates is an effective method for improving energy

efficiency. Priarone (2016) also demonstrated that process filtering and cooling uses more energy than the process.

Several authors have investigated using minimum quantity lubrication (MQL) by using cold air from a compressed air system ran through a vortex tube. Choi (2001) showed that as compared to coolant surface roughness (R_a and R_z μm) will be larger, but that the difference greatly reduces as depth of cut (μm/sec) increases. Nguyen and Zhang (2003) found that, as compared to dry grinding, cold air can reduce grinding burn at low material removal rates. Saberi et al. (2016) demonstrated that this method will produce equivalent or worse surface roughness (R_a and R_z μm) than dry grinding. Cearsolo et al. (2016) found that when dressing a grinding wheel, the observed deformation of the tool holder was 2 μm when the cold air was at -20 ^oC, and was an equivalent deformation to dressing with coolant.

5.4 Experiment Methodology

The experiment utilized workpieces, a grinding machine tool, a collection of sensors, post-experimental analysis, and followed a design of experiments (DOE) protocol. The following subsections describe each of the items identified.

5.4.1 Workpieces

It was desired to investigate a workpiece material that is typically used for bearings, is typically ground, can be hardened, and is readily available in an easy to work with size. 440C stainless steel was selected for the experiment because it met these requirements, while being available in the correct size and square shaped bar stock. The workpieces are hardened 440C stainless steel all cut

from a three-foot section of bar stock. The bar stock first underwent the following hardening procedure to 60C Rockwell, and then cut to ½ x ½ x 1 inch cuboids to form the workpieces.

- Preheating at 1550^{o}F (843^{o}C) for minimum one hour under vacuum
- Hardening at 1900^{o}F (1038^{o}C) for minimum one hour under vacuum
- Forced cool to below 150^{o}F (66^{o}C) under vacuum
- Tempering in air at 300^{o}F (149^{o}C) for at minimum two hours
- Air cool

5.4.2 Grinding Machine Tool Setup

The Baldor Grinder 248-183TD is a combination pedestal grinder, with both an abrasive wheel and abrasive belt, and has a 1.5 horsepower motor; as seen in Figure 5.1. The motor has a shaft at both ends, one for the wheel and one for the belt. It was found during testing that the wheel attributed to excessive vibrations during grinding, it was thus removed for the experiments (Seibt, 2019, pp. 27–29). Additionally, three spindle speeds were selected for the design of experiments, one low, one middle, and one high speed, that do not cause excessive vibrations. The selected speeds were 1000, 1950, and 2900 RPM to minimize excessive noise in the force sensor (Seibt, 2019, pp. 27–29). Additionally, the abrasive used was aluminum oxide and two grit mesh numbers were used to perform the experiments, 120 grit and 180 grit 3M - 341D cloth abrasive belts. Belts measured 2in x 48in.

The abrasive belt was selected for this griding experiment over the grinding wheel for multiple reasons. First, using the belt allows for griding against the flat backing plate surface thus will result in a flat workpiece post grinding, which eases measurement of surface roughness. Second, while the linear guideway provides two axes of motion, one axis was not operational at the time of the

experiment, which only allowed for a single axis of movement, using this axis to plunge allows the use of the abrasive belt; a second working axis would be needed to dress the grinding wheel. Thirdly, replacing a belt with the machine is much quicker than dressing the grinding wheel, thus experiment time is minimized by using the abrasive belt.

The linear guideway is made of two Bosch Rexroth Precision PSK 60, one mounted on top of the other to allow for 2 axes of motion. The two guideways are controlled and driven by a Bosch Rexroth IndraMotion MTX L45 controller. Using the IndraWorks Operation software, the machine was controlled using a computer connected to the PLC; and the G-code could be directly edited on the machine. An example of the G-code used for the experiments is shown below:

N10 G01 X300.F3000

N20 G01 X302.3 F3

N30 G01 X300.0 F10

N40 G01 X200.0 F3000

Where the home position is at X = 200 mm, the machine rapid travels to X = 300 mm, the cutting starts at X = 302 mm, and the cut ends at X = 302.3 mm with a depth of cut of 0.3 mm; and the feed varies between 3 mm/min and 3000 mm/min (although it didn't actually travel at 3000 mm/min, just the maximum speed).

Cooling air was used to dissipate heat from the machine, and perform for dry grinding. An Exair 3204 vortex tube was used inline with the compressed shop air to supply chilled air, as shown in Figure 5.1. The vortex tube is used to separate a single airstream into two, one hot and one cold.

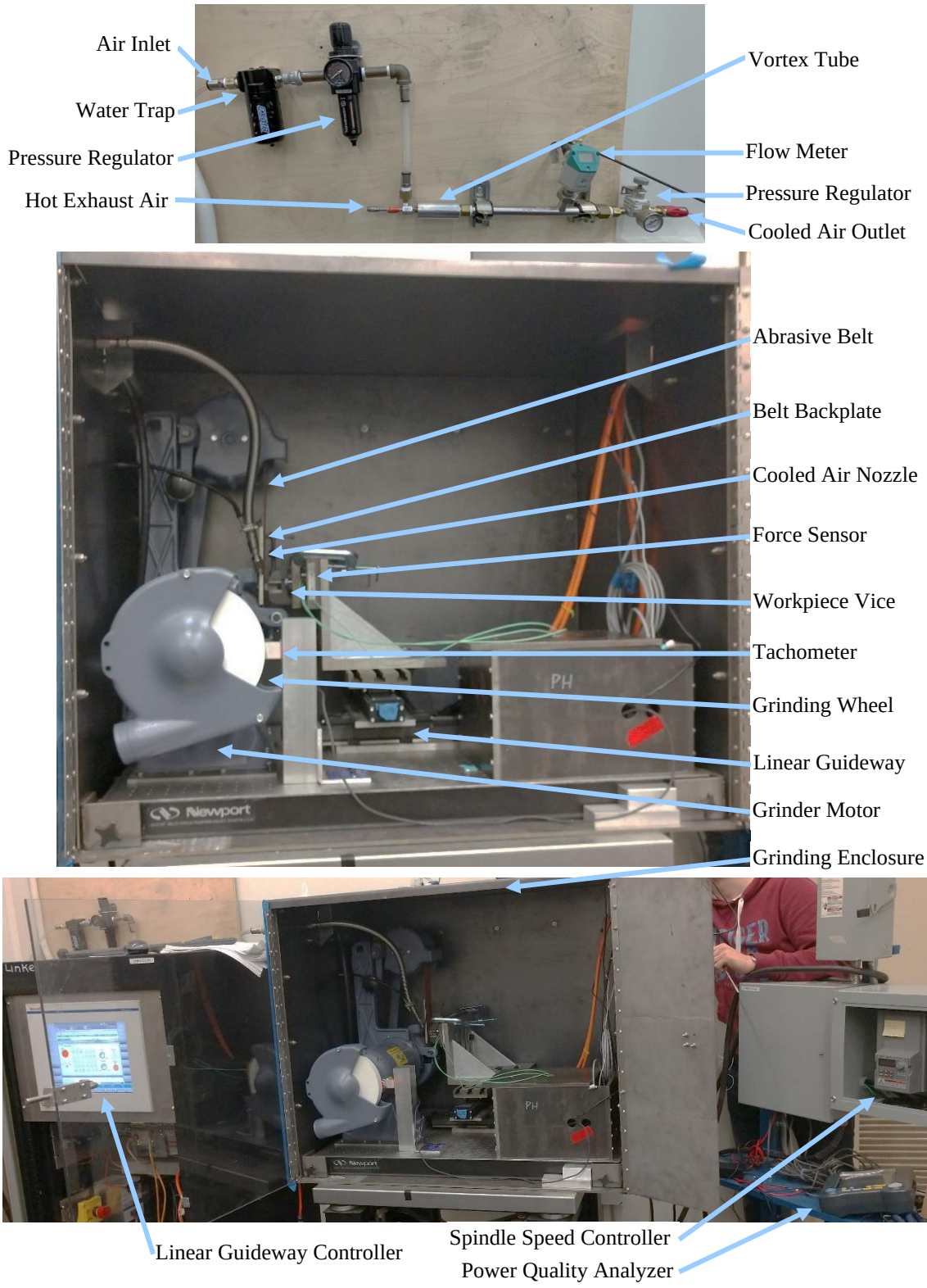

Figure 5.1: Grinding machine experimental setup; top: cool air supply; middle: grinding machine; bottom: controllers and enclosure

Two pressure gauges were used, one before and one after the vortex tube, to validate that the air was supplied and remained at a steady state. Following the recommendations of Lei (2018), the vortex tube screw position was set to 0.25, and the supply pressure was varied for three different experimental levels, being 0 Bar, 3.3 Bar, and 6.6 Bar; this should provide an output temperature of NA, 18 ºC, and 8 ºC respectively and output flow of NA, 1.7 m^3/h, and 3.7 m^3/h respectively.

5.4.3 Data Collection

Data was collected using several different sensors, including a force sensor, a power analyzer, and a profilometer. The force sensor is a Kistler 9251A, measures three components, being F_x, F_y, and Fz, and by utilizing three pairs of piezoelectric quartz rings, two for shear and one for pressure. The quartz rings in the sensor output a charge which is fed into an amplifier, and converts the charge into a voltage between 0 and 10 V; where the x and y axis were set to -8 pC/N, and the z axis was set to -4 pC/N. The charge amplified is connected to a computer via USB, and a National Instruments data acquisition unit (DAQ) which is also connected to the computer via USB. Kistler ManuWare software is then used to control the amplifier, and National Instruments SignalExpress is used to log the data. The force sensor was mounted between the plunge axis of the linear guideway on a right-angle block and the workpiece vice. This mounting location and orientation allows the z-axis to collect normal force data, and the x-axis to collect tangential force data; the y-axis was not used.

A Yokogawa CW240 clamp-on power quality analyzer used to collect power data. The analyzer uses both voltage probes and current probes to calculate and log real-time power usage data. The power analyzer was used to measure the power consumption of the Baldor grinder and was

connected inline before the variable frequency drive (VFD) speed controller. The Baldor motor was wired such that only two of the three phases delivered power to the motor; thus the Yokogawa was set to measure using the three phase, three wire, three current (3P3W3I) setting and 1 of the three measurement was zero because it had no current. The power meter sampling time interval was set to 1 wave, which is sampling frequency of 60Hz yielding 60 measurements per second. This was the fastest sampling frequency setting on the power quality analyzer and will capture short power spikes typically observed in machine tool operation.

A Bruker DektekXT profilometer was used to collect two-dimensional height data of the samples after they were ground. The profilometer uses a physical stylus with a 12.5 μm radius tip, has a vertical resolution of about ½ nm (4 Å), and collects a maximum of 2182 data points per mm. The measured profile is then filtered to remove form and waviness, and yield only roughness data. Then roughness parameters can be calculated, described in Section 5.5.3.

5.4.4 Design of Experiments

The grinding experiments that follow were carried out in two blocks, with four total factors. The two blocks use grinding belts with two different grit mesh numbers, 120 and 180, wherein the grinding belts were changed every three experiments (wide enough for 3 experiments to be ground on new grit); and the 120 grit experiments were all ran first followed by the 180 grit experiments. Thus, two sets of grinding experiments were carried out with three factors each. These factors include spindle speed (RPM), feed rate (mm/s) and cooled air (Bar). In the first set of experiments, each factor was tested at three treatment levels. In the second set, each factor was tested at two treatment levels. This can be seen in Table 5.1, where the yellow and blue highlighted colors

identify the varied factors. Additionally, to save time and resources a full factorial design was not carried out, thus the experiments is a fractional factorial design. The experiments were randomized within the blocks, the sequence can also be seen in Table 5.1.

Table 5.1: Experiment Design

		Spindle Speed	Feed Rate	Air Pressure
	Exp. No.	RPM	mm/s	Bar
120 Grit	4, 9, 11	1000	5.5	3.3
	3, 5, 10	1950	1	3.3
	7, 12, 20	1950	5.5	3.3
	2, 17, 18	1950	10	3.3
	6, 13, 15	1950	5.5	0
	14, 16, 21	1950	5.5	6.6
	1, 8. 19	2900	5.5	3.3
180 Grit	3, 6, 12	1950	5.5	3.3
	1, 8, 9	1950	5.5	6.6
	2, 4, 7	1950	10	3.3
	5, 10, 11	2900	5.5	3.3

A total of 36 experiments were carried out. Three experiments were omitted from the results due to poor resulting data, much lower force and energy readings. This was likely caused by incorrect offsets used in the grinding machine tool when these three experiments were setup. These were 120 grit experiment number 2, and 180 grit experiment number 2 and 10.

5.5 Results and Discussion

5.5.1 Spindle Power and Energy Results from Power Quality Analyzer

The power data was collected with a Yokogawa power meter. An example of the power data collected can be seen in Figure 5.2. This power profile can be subdivided into 3 phases, the first is the start-up phase, and accounts for the spindle accelerating. The second is the idle phase, and

accounts for the spindle being on but not engaged with the workpiece. And the third is the grinding phase, and accounts for the cutting action of the grinding belt engaged with the workpiece. Table 5.2 shows an example of the division of power and energy calculated using the phases as described.

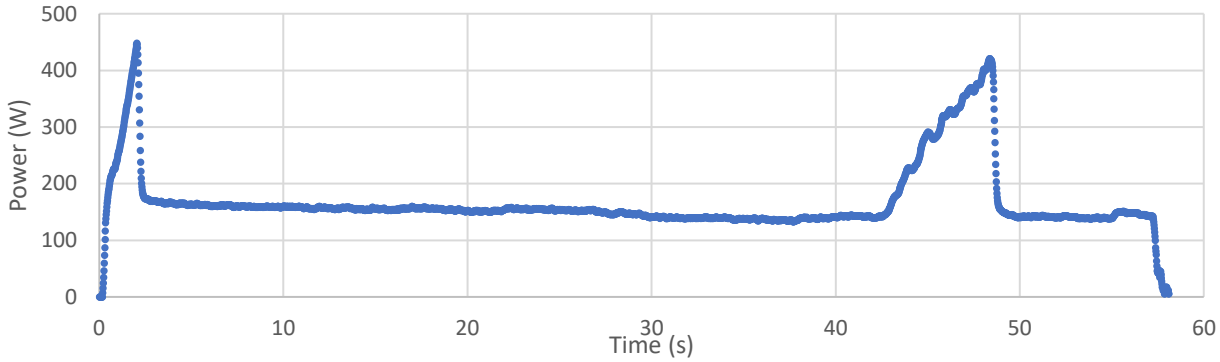

Figure 5.2: Example power data collected, note peak power from spindle start-up at the left side of the graph, the middle idle energy (machine is feeding), and the second peak is the grinding energy; experiment is 180 Grit, 1950 RPM, 5.5 mm/s, 6.6 Bar

Table 5.2: Example cut-offs used to subdivide the power band into different phases; 180 Grit, 1950 RPM, 5.5 mm/s, 6.6 Bar

Peak Startup Power (W)	Startup Energy
448.18	592.00
Idle Power (W)	Idle Energy
259.09	6073.68
Peak Grinding Power (W)	Grinding Energy
420.91	1868.09

Energy is integrated from the power data using the trapezoidal rule following same method as described in Chapter 4: and (Voet et al., 2018), and the integration limits are determined using the phases described previously. This yields two points interesting energy data, the first being the grinding energy, which is expected to vary depending on the parameters identified in the DOE. The second would be the start-up energy, which varies on account of the RPM. The idle energy is less interesting in this case, because there is unaccounted variance in the time between when the

spindle starts and when the grinding occurs; the as the spindle and feed systems are controlled independently on the machine, and with the experiment not designed to collect idle energy data. Thus, the idle power could be used for comparisons, but not the idle energy.

Table 5.3 and Table 5.4 show the power measurements and energy results for each replication of each treatment combination. The tables show the results on the left and the treatment combinations on the right, and the experiment number in the far left. The peak startup power and peak grinding power are calculated as maximums of their respective operation phase. The idle power is calculated as an average of the idle operation phase. Each energy segment is calculated as an integration of the power over the respective operation phase. Note that experiment 2 in Table 5.4 and experiments 2 and 10 Table 5.3 did not have apparent grinding phases, and were assumed to not cut to the full 0.3 mm depth.

Table 5.3: 180 Grit Power and Energy Data

Exp. No.	Peak Startup Power W	Idle Power W	Peak Grinding Power W	Start up Energy Ws	Idle Energy Ws	Grinding Energy Ws	Spindle Speed RPM	Feed Rate mm/s	Air Flow Bar
E3	447	336	256	582	6636	772	1950	5.5	3.3
E6	444	185	286	611	5848	926	1950	5.5	3.3
E12	442	329	344	572	6716	1695	1950	5.5	3.3
E1	150	2560	2960	448	0	0	1950	5.5	6.6
E8	435	172	356	639	6210	1340	1950	5.5	6.6
E9	440	182	329	608	6077	1312	1950	5.5	6.6
E2	450	189		624	4573		**OMITTED!**		3.3
E4	438	350	353	578	4623	610	1950	10	3.3
E7	438	180	343	607	4843	643	1950	10	3.3
E5	650	324	492	1211	11661	2229	2900	5.5	3.3
E11	693	368	425	1252	17346	2024	2900	5.5	3.3
E10	659	344		1222	14063		**OMITTED!**	5.5	3.3

Table 5.4: 120 Grit Power and Energy Data

Exp. No.	Peak Startup Power W	Idle Power W	Peak Grinding Power W	Start up Energy Ws	Idle Energy Ws	Grinding Energy Ws	Spindle Speed RPM	Feed Rate mm/s	Air Flow Bar
4	246	98	154	211	1460	567	1000	5.5	3.3
9	245	117	180	377	1640	447	1000	5.5	3.3
11	235	86	197	205	1504	496	1000	5.5	3.3
3	449	181	179	621	7417	984	1950	1	3.3
5	495	217	238	707	7616	3452	1950	1	3.3
10	440	171	195	606	5956	3137	1950	1	3.3
7	441	302	245	578	2595	666	1950	5.5	3.3
12	455	186	278	620	3163	1677	1950	5.5	3.3
20	432	165	288	598	3677	1054	1950	5.5	3.3
2	663	309		1237	7222		**OMITTED!**		
17	465	195	324	638	3114	521	1950	10	3.3
18	439	168	272	601	2213	445	1950	10	3.3
6	453	183	295	618	3299	881	1950	5.5	0
13	445	310	240	582	2614	643	1950	5.5	0
15	450	183	204	616	3024	381	1950	5.5	0
14	473	372	285	611	3217	798	1950	5.5	6.6
16	444	330	279	579	3013	710	1950	5.5	6.6
21	435	178	300	602	2776	792	1950	5.5	6.6
1	660	327	286	1232	7139	535	2900	5.5	3.3
8	655	311	399	1229	5132	1243	2900	5.5	3.3
19	634	287	397	1190	4477	1207	2900	5.5	3.3

Figure 5.3 and Figure 5.4 displays the energy consumption results of the study. It can be seen that increasing spindle speed causes an increase in energy consumption, as seen in Figure 5.3. It can also be seen that decreasing feed rate increases energy consumption, as seen in Figure 5.4. These results match expectations, first a faster spindle speed would draw more amperage and thus more power to run the motor, and would result in more energy consumption with all other variables held constant. Second, a slower feed rate would increase the experiment time and thus increase energy consumption with all other variables held constant.

Finally, Figure 5.5 shows the results from increasing the cooling air supplied (measured in Bar) to the work zone; it can be seen that the energy consumption increased when the cooling air increased.

Perhaps the workpieces are hardened as they heat up during grinding and the cold air quenches the upper workpiece layer. Nguyen and Zhang (2003), also showed a hardening effect with a higher travel distance during their grinding process; and furthermore explain that air is a poor heat removal medium at high temperatures due to air's heat transfer coefficient dropping.

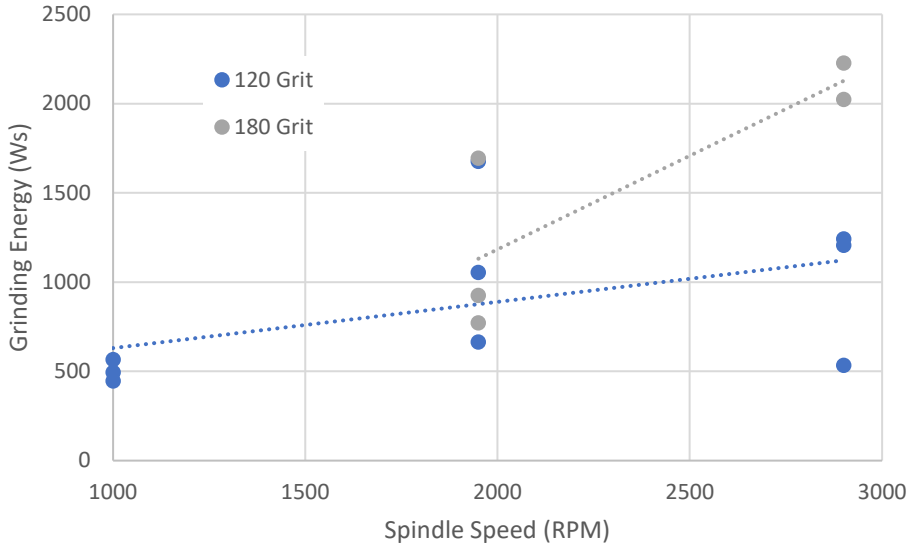

Figure 5.3: Grinding energy (Ws) and spindle speed (RPM) results

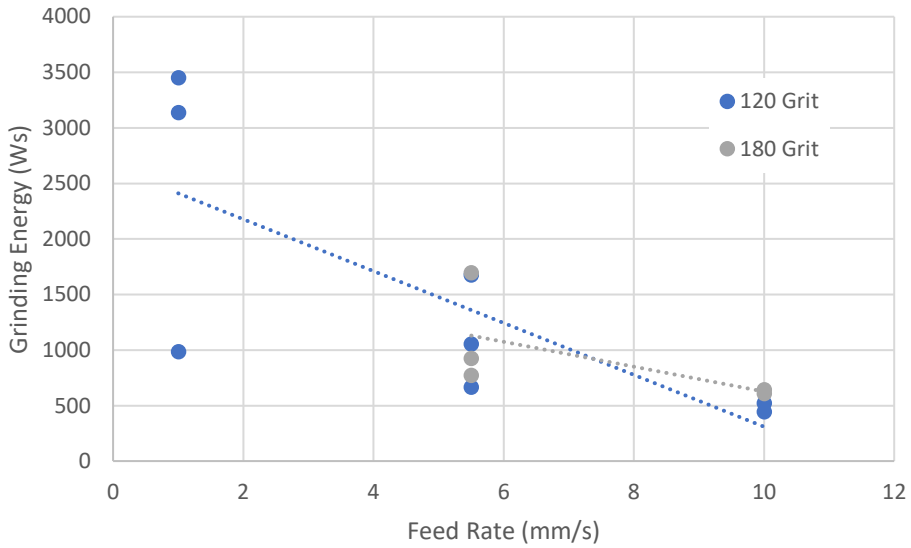

Figure 5.4: Grinding energy (Ws) and feed rate (mm/s) results

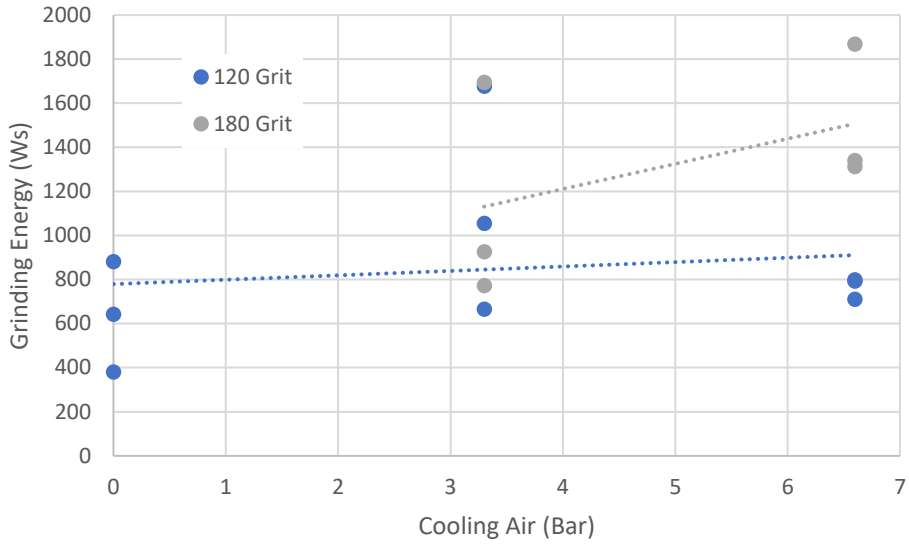

Figure 5.5: Grinding energy (Ws) and cooling air (Bar) results; the cold air supplied to the workpiece was 3.3 bar was at 18ºC and 6.6 bar was at 8ºC.

5.5.2 Work Calculated from Force Results

Figure 5.6 shows a comparison between different rolling averages and the impact on data smoothness and lag using data from 180 grit block experiment 5.

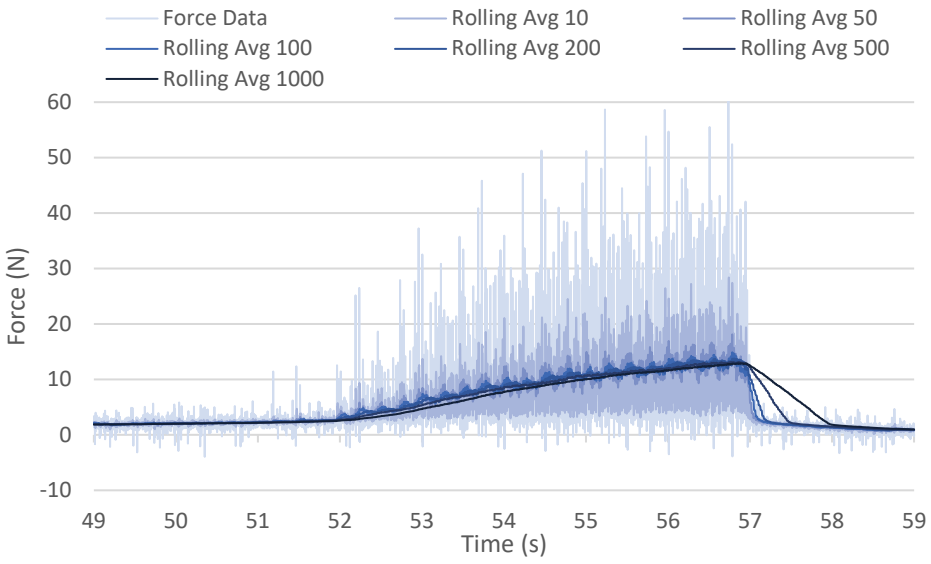

Figure 5.6: Comparison of Rolling Averages; example from 180 grit experiment 5

The lag is apparent between 57 and 58 seconds where the force can be seen to gradually fade for the higher rolling averages. A rolling average of 200 can be seen to have minimal lag and provides highly smoothed data.

Table 5.5 shows the calculated energy for each rolling average filter applied to the example data set. It can be seen that regardless of the size of the rolling average filter, the calculated work (Ws) all have similar values, close to 1670 Ws. Additionally, a simple high pass filter is applied to only passes values greater than 2N, this is shown in Figure 5.7. Calculated work (Ws) values using the simple high pass filter are also shown in Table 5.5, and with the exception of the unfiltered force data the values are all similarly close to 820 Ws. Thus, any rolling average filter along with a simple high pass filter will result in similar work values.

Table 5.5: Work in Watt-seconds integrated from force data; rolling average and rolling average with a simple high pass filter of greater than 2 N; example from180 grit experiment 5

	Work (Ws)	
	Roll Avg	High Pass
Force Data	1675	954
Rolling Avg 10	1675	833
Rolling Avg 50	1675	819
Rolling Avg 100	1674	821
Rolling Avg 200	1673	821
Rolling Avg 500	1669	820
Rolling Avg 1000	1662	822

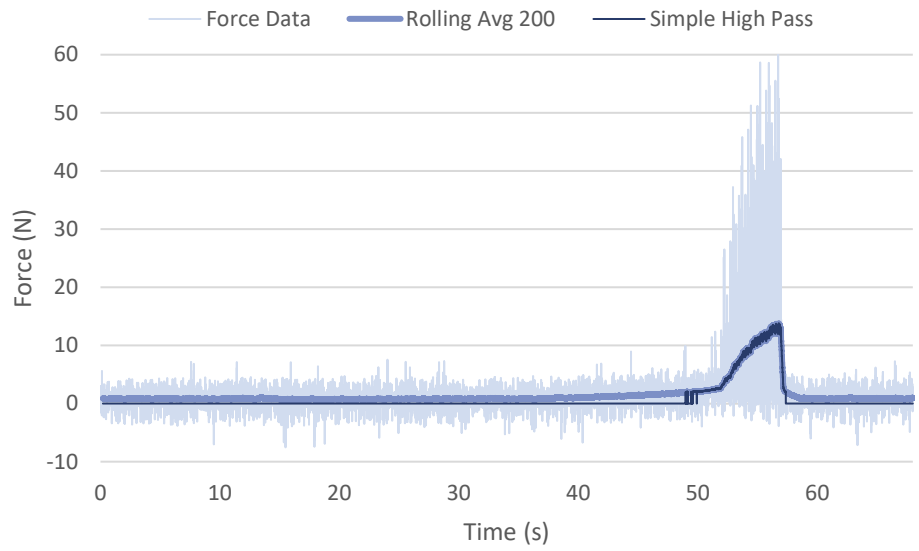

Figure 5.7: Example force data showing in X direction, and the filtered data. Two filters were used, first a 200-point rolling average filter and second a simple high pass greater than 2N.

Work values were calculated using two equations. Work done by the grinding spindle was calculated using equations (5.1) and (5.2), work done by the feed drive was calculated using equations (5.1) and (5.3). But the work done by the feed drive was found to be negligible.

$$W = \int f dx \tag{5.1}$$

$$dx = 2\pi r_{belt} V_s \frac{1}{1000} \tag{5.2}$$

$$dz = f_r \frac{1}{1000} \tag{5.3}$$

Where dx is the distance the belt moves per each force reading, r_{belt} is radius of the belt grinders drive wheel in meters, V_s is the revolutions per second (RPM/60), f_r is the feed rate in m/s, and it is divided by sampling rate which is 1000.

Figure 5.8 shows the force data collected for the 180 grit experiments after being filtered using a 200-point moving average. A simple high pass filter can be applied to easily identify the when the grinding occurs. This high pass filter value was selected individually for each experiment to keep a majority of the data without losing too much; cutoffs used were between 1N and 2N.

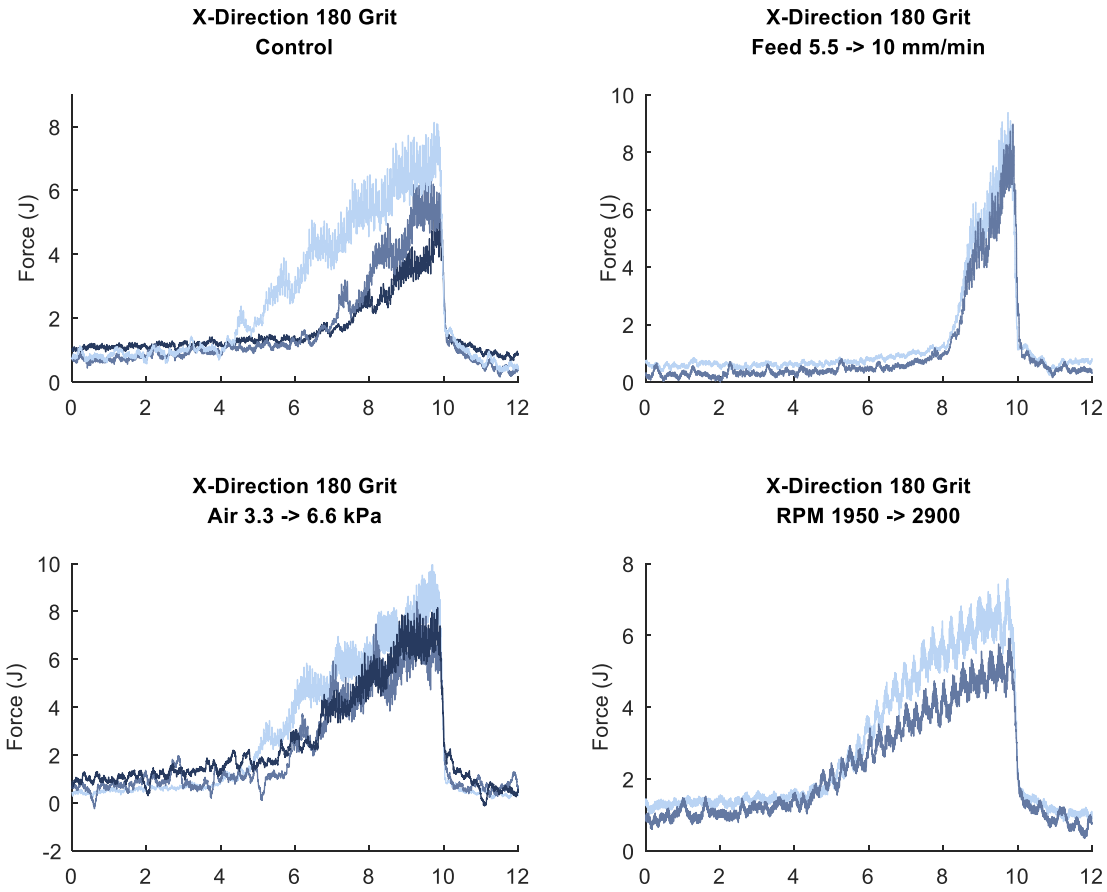

Figure 5.8: Forces in the X direction; filtered using a 200-point moving average; used to calculate spindle energy consumption for the 180 grit experiments

The calculated work is plotted below Figure 5.9, Figure 5.10, and Figure 5.11. It can be seen that the data trends in general match the measured energy results from Section 5.5.1. Increasing spindle

speed increases work performed by the spindle. Increasing feed rate decreases work, since the operation is finished earlier.

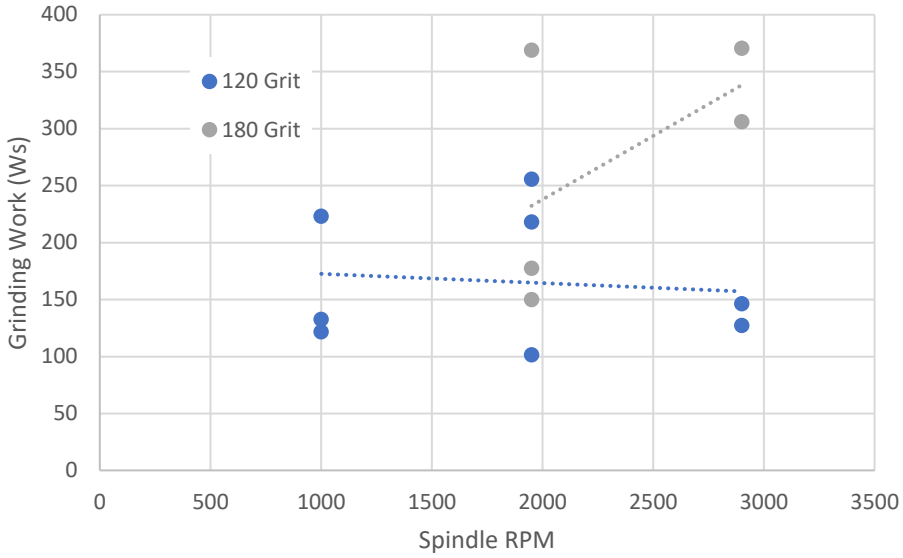

Figure 5.9: Calculated work (Ws) and spindle speed (RPM)

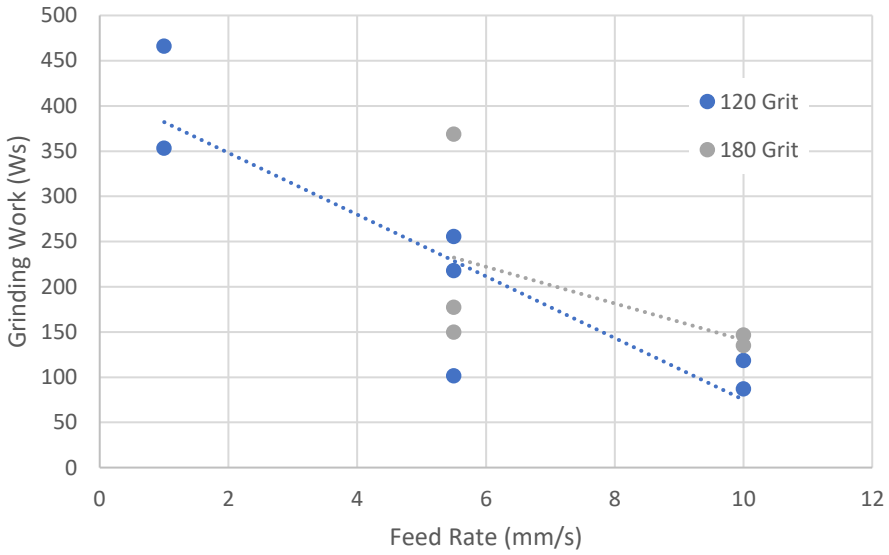

Figure 5.10: Calculated work (Ws) and feed rate (mm/s)

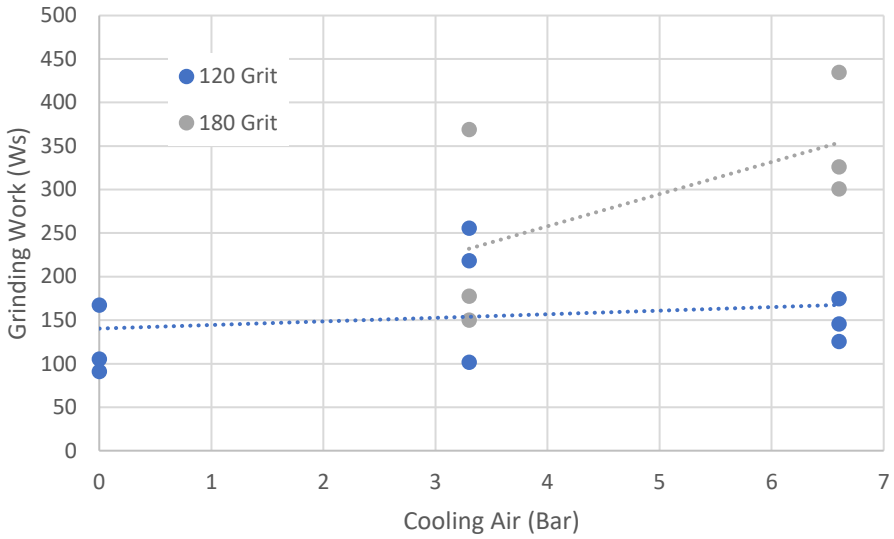

Figure 5.11: Calculated work (Ws) and cooling air (Bar)

Table 5.6 shows the difference between the two calculated energy values, and are shown as average values for each treatment combination. The table shows power-measured energy minus the force-measured work. The difference between the measurements can be attributed to a several phenomena. First, the power quality analyzer is measuring power for both the motor and the motor controller. Second the power quality analyzer also captures input power for the motor, which includes any losses not seen from the output power. Third, the two measurement devices have different sensitivities and different amounts of noise in their data. Fourth, the speed of the belt was estimated during the actual measurements and could likely have some variation; as the grinding wheel and corresponding tachometer was removed from the grinder during the experiments to minimize noise in the force measurements. All of these reasons can lead to differences and discrepancies in the values.

Table 5.6: Averages and difference between power measured electricity and force measured process work of the spindle.

	Exp. No.	Spindle Speed RPM	Feed Rate mm/s	Air Pressure Bar	Electricity Ws	Process Work Ws	Difference Ws	Percent Difference %
120 Grit	4, 9, 11	1000	5.5	3.3	503.1	159.2	344.0	216.11
	3, 5, 10	1950	1	3.3	3294.3	410.0	2884.3	703.58
	7, 12, 20	1950	5.5	3.3	1132.2	191.8	940.4	490.20
	2, 17, 18	1950	10	3.3	483.0	102.8	380.3	370.07
	6, 13, 15	1950	5.5	0	634.7	121.2	513.4	423.51
	14, 16, 21	1950	5.5	6.6	766.7	148.7	618.0	415.70
	1, 8. 19	2900	5.5	3.3	1224.5	136.9	1087.6	794.48
180 Grit	3, 6, 12	1950	5.5	3.3	1130.8	232.2	898.6	387.07
	1, 8, 9	1950	5.5	6.6	1506.9	353.7	1153.1	325.99
	2, 4, 7	1950	10	3.3	626.6	141.0	485.6	344.39
	5, 10, 11	2900	5.5	3.3	2126.6	338.3	1788.3	528.61

5.5.3 Roughness Results

Each sample was measured using a Bruker DektekXT profilometer twice, both measurements were then used to calculate roughness parameters. After measuring the samples, each measurement was filtered using highpass gaussian filter with a cut-off length lambda C (λ_c) value of 0.8, to filter out the form and waviness values, as described in ISO 16610-20 and -21 (ISO, 2011, 2015a). A lowpass filter using a lambda S (λ_s) value was not applied as this is assumed to be negligible, as the tip radius of the measurement device is assumed to filter the higher order noise. Figure 5.12 shows an example of the measured profile as a blue line, and the form and waviness that were filtered out as a red line, and the resulting roughness as a green line.

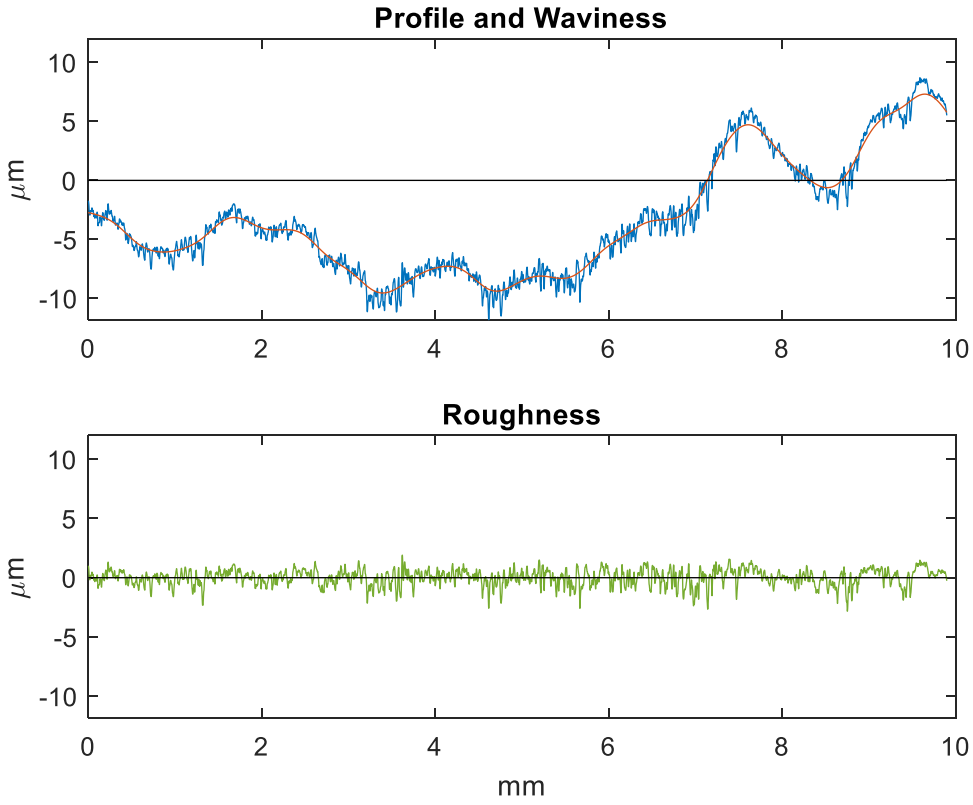

Figure 5.12: Example of roughness measurement from Dektek profilometer; above shows the profile and waviness which was filtered out to yield the roughness below (in green).

After filtering the data, roughness values were calculated following the standards ISO 4287 and ISO 13565-2 (ISO, 1996a, 1997a); including amplitude parameters, hybrid parameters, and functional parameters. The calculation was performed for each measurement, and with two measurements per sample, an average was taken for each sample. Each treatment combination was repeated three times, and the averaged roughness results across each treatment combination can be seen in Table 5.7. The left side of the table displays the treatment combinations, and the right side displays the averaged roughness parameters.

Table 5.7: Averaged R-Parameter Roughness Results

	Exp. No.	Spindle Speed RPM	Feed Rate mm/s	Air Pressure Bar	*Rp*	*Rv*	*Rz*	*Rt*	*Ra*	*Rq*	*Rsk*	*Rku*	*Rdq*	*Rc*	*Rsm*	*Rk*	*Rpk*	*Rvk*	*Mr1*	*Mr2*
120 Grit	4, 9, 11	1000	5.5	3.3	2.79	3.79	6.58	10.23	1.06	1.32	###	3.05	0.12	2.72	62.83	3.11	1.19	1.95	9.60	86.54
	3, 5, 10	1950	1	3.3	2.46	3.25	5.71	9.43	0.97	1.21	###	2.94	0.08	3.18	96.89	2.95	1.24	1.77	9.48	87.81
	7, 12, 20	1950	5.5	3.3	2.35	3.07	5.42	8.35	0.97	1.19	###	2.75	0.08	3.48	107.31	2.88	1.12	1.46	10.83	88.62
	2, 17, 18	1950	10	3.3	2.49	3.54	6.03	11.06	1.03	1.29	###	3.17	0.09	3.61	97.85	3.02	1.24	2.00	9.42	87.07
	6, 13, 15	1950	5.5	0	2.68	3.42	6.09	9.92	1.03	1.28	###	2.93	0.10	2.81	81.72	3.07	1.17	1.71	11.19	87.67
	14, 16, 21	1950	5.5	6.6	2.62	3.63	6.24	9.84	1.05	1.30	###	3.05	0.11	2.21	71.91	3.07	1.27	1.78	9.81	86.79
	1, 8. 19	2900	5.5	3.3	2.39	3.21	5.59	10.26	0.92	1.15	###	3.11	0.09	6.28	88.04	2.63	1.14	1.87	10.08	87.69
180 Grit	3, 6, 12	1950	5.5	3.3	2.30	2.90	5.20	8.32	0.76	0.97	###	3.77	0.11	3.82	46.98	2.23	0.93	1.35	10.26	87.21
	1, 8, 9	1950	5.5	6.6	2.44	3.33	5.77	9.44	0.81	1.04	###	3.66	0.13	3.87	44.79	2.47	0.86	1.53	8.44	87.38
	2, 4, 7	1950	10	3.3	2.52	3.20	5.72	8.20	0.88	1.11	###	3.18	0.12	3.01	52.89	2.66	0.86	1.49	8.48	86.83
	5, 10, 11	2900	5.5	3.3	1.82	2.62	4.45	6.92	0.58	0.76	###	4.13	0.10	1.36	43.28	1.73	0.63	1.19	9.49	87.99

440C stainless steel is typically used for manufacturing bearings, (Sacerdotti et al., 2000) identifies that bearings are best evaluated using amplitude and functional roughness parameters; thus, the the functional parameters (*Rk, Rpk,* and *Rvk*) calculation are described herein. Where *Rk* is the core distance, *Rpk* is the reduced peak height, and *Rv*k is the reduced valley height. These parameters are calculated using the Abbott-Firestone curve as described in ISO 13565-2; an example is shown in Figure 5.13. While the method used follows ISO 13565-2, for clarity a simplified account for the calculation is described as follows. The Abbott curve shows the profile height values sorted in order from highest to lowest (blue line), a line is fitted to points with the smallest slope and extended to the ends of the graph (red line), a horizontal line is drawn from the edge of the graph to intersect the Abbott curve (dashed horizontal green line), then a triangle is drawn with an equivalent area to the area between the horizontal line and the Abbott curve (dashed green triangles).

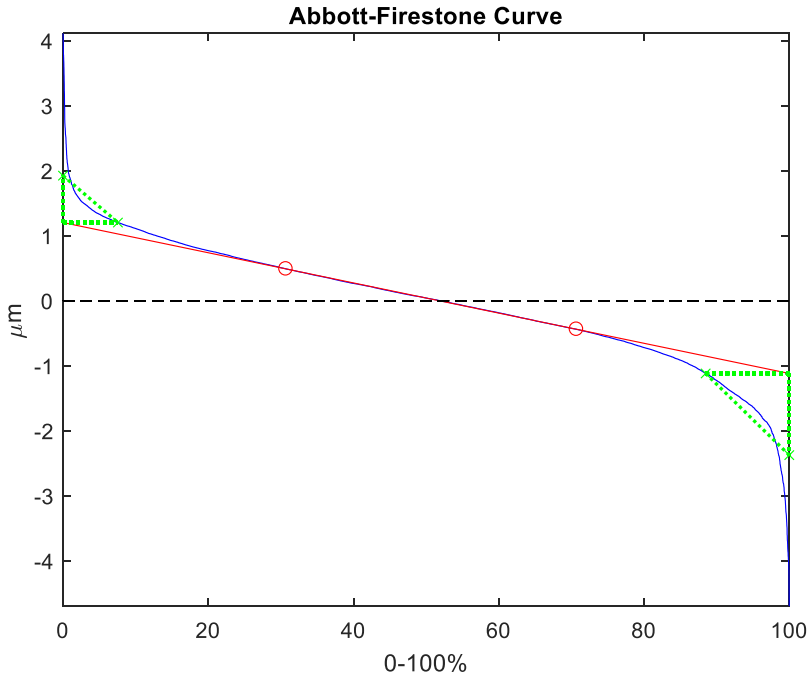

Figure 5.13: Example Abbott-Firestone curve, which shows the height values of a roughness measurement sample sorted highest to lowest, and enables the calculation of *Rk*, *Rpk*, and *Rvk*.

Figure 5.14 shows the profile roughness results for the samples, split into three graphs to both display the data concisely and clearly. The roughness values are shown for both changes in spindle speed and feed rate. Results for changes in air pressure were minimal and thus not displayed. It can be seen in Figure 5.14 that the R-parameters in general decreased with increasing spindle speed and increased with increasing federate. These results are expected and align with the grinding fundamentals of chip formation. Larger chips are expected to occur with decreasing spindle speed and increasing feed rate. The opposite is also true, smaller chips are expected to occur with increasing spindle speed and decreasing feed rate. Stated simply, a higher feed rate and slower spindle speed will increase an individual chip's depth of cut, among other changes to chip geometry.

Figure 5.14 noticeably displays larger changes in roughness for the 180 grit experiments vs the 120 grit experiments. Considering that the 120 grit and 180 grit experiments were respectively blocked together, and not randomized across the two grits (experiments were randomized within blocks), this difference would be accounted for in experimental setup between the blocks.

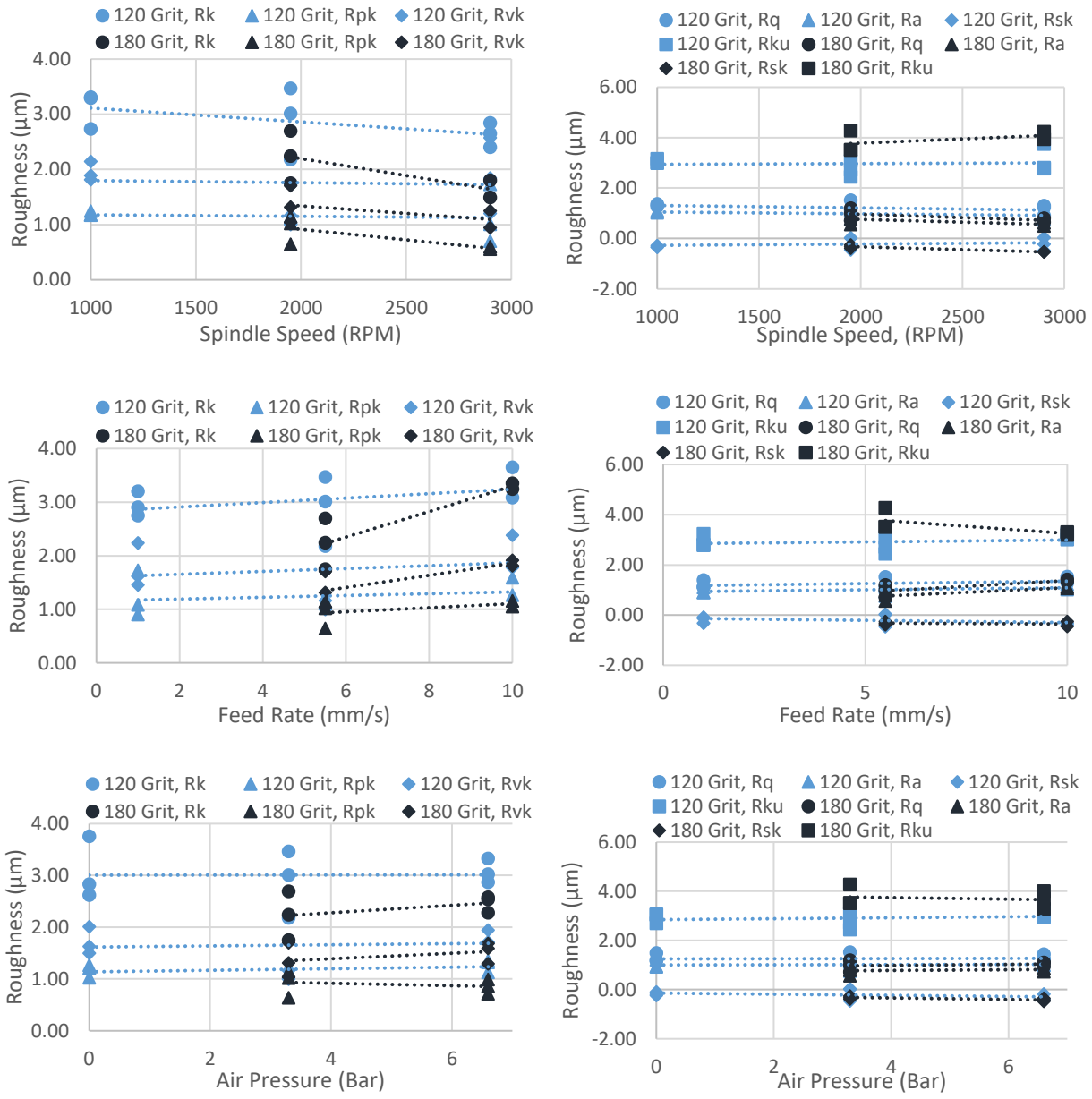

Figure 5.14: R-Parameter roughness results

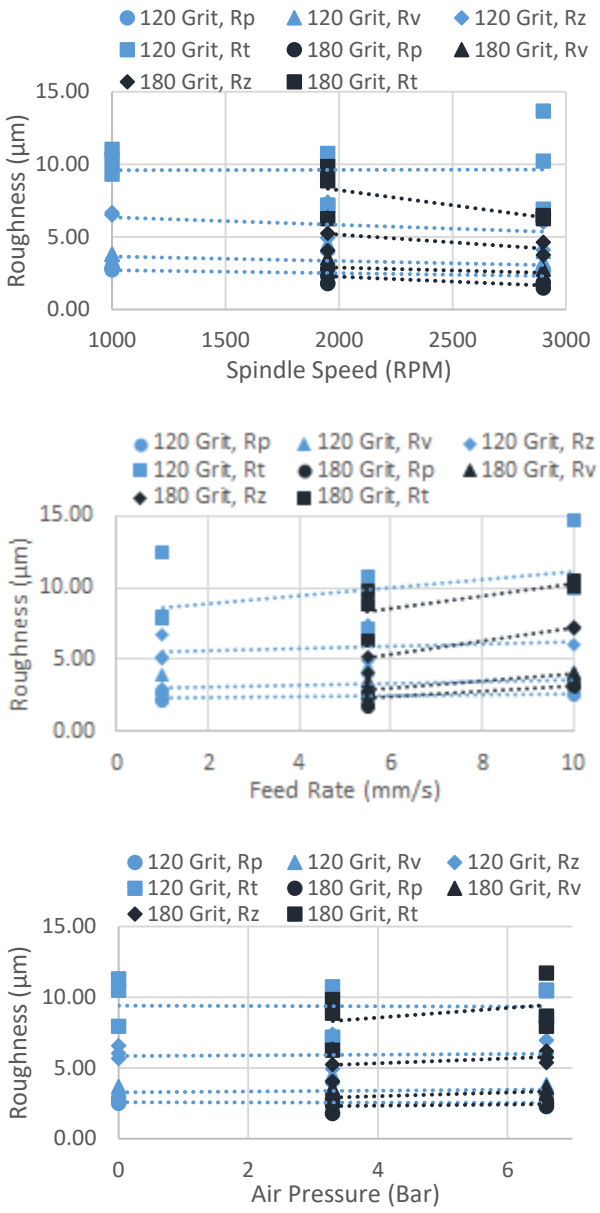

Figure 5.15: R-Parameter roughness results continued

5.5.4 Energy and Roughness Comparison

Comparing the energy consumption and the surface roughness of the workpieces, Figure 5.16 demonstrates that for nearly every *R* roughness parameter evaluated, with the exception of kurtosis R_{ku}, the trend of increased energy consumption decreases roughness holds true. The trend is more

apparent with the 180 grit data, which again is likely an unattributable effect of blocking but could be caused by the smaller grit sizes of the 180 grit cloth belts.

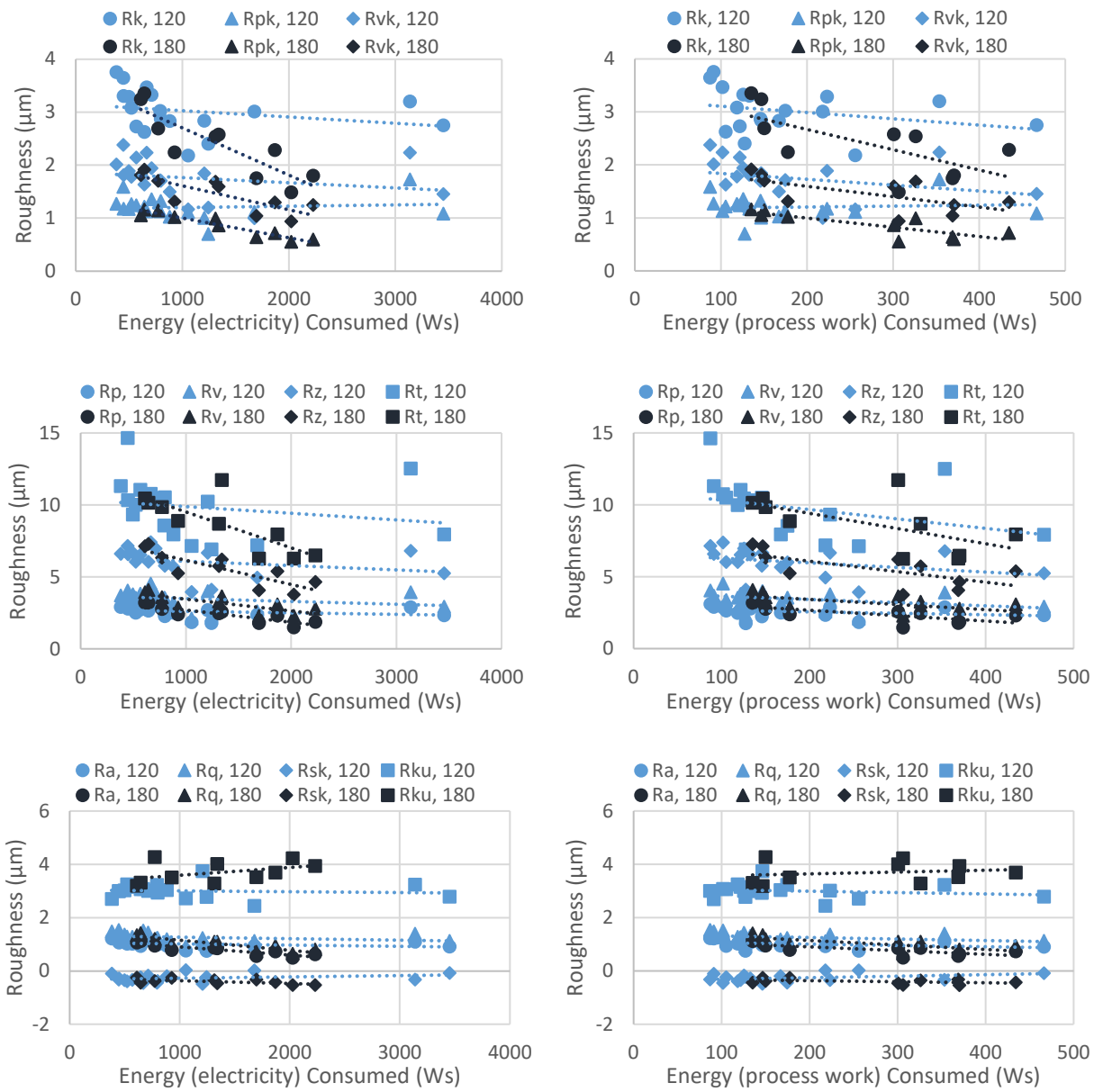

Figure 5.16: Comparison between energy consumed and surface roughness; left is electricity right is process work

The increase in kurtosis is seen in tandem with an increase in negative skewness and an overall decrease in roughness. The increase in kurtosis would indicate pointer peaks and valleys, but with an increase in negative skewness, this indicates that the valleys are remaining pointy and the peeks are being shaved off. In tandem with decreases in *Rk*, *Rpk*, and *Rvk*, the middle area, peaks, and valleys are all smaller.

5.6 Conclusion

This work investigated the tradeoff between energy consumption and roughness generation of a grinding machine. The work additionally investigated the difference in energy consumption when measuring with a power meter and with a force sensor. Additionally, this work had investigated using cold air generated from a vortex tube to act as a grinding coolant. This work had also reviewed the literature that also had investigated energy consumption and roughness tradeoffs, and literature that had used cold air with grinding. Findings identified a strong indication that as surface roughness decreases an increase in energy consumption would be expected when grinding. Future work includes expanding the experimentation with the vortex tube generator, and see what tradeoffs occur between colder air at lower flows vs warmer air at higher flows. Additional future work includes investigating the energy and roughness tradeoffs between other materials, the application here was for hardened steel with application in bearing technology, perhaps other materials will exhibit a stronger or lesser correlation between energy and roughness.

Chapter Six: Effects of Vibratory Finishing of 304 Stainless Steel Samples on Areal Roughness Parameters: A Correlational Analysis for Anisotropy Parameters

By

Matthias Eifler, Ian C. Garretson, Francois Torner, Jörg Seewig, Jayanti Das, Barbara S. Linke

Submitted to the *Journal of Materials Processing Technology*

https://www.journals.elsevier.com/journal-of-materials-processing-technology

Chapter 6: Effects of Vibratory Finishing of 304 Stainless Steel Samples on Areal Roughness Parameters: a Correlational Analysis for Anisotropy Parameters

6.1 Abstract

Characterizing abrasive manufacturing processes and their resulting surfaces has been subject to numerous examinations. Because ground surfaces are inherently stochastic, surface anisotropy is a particular interesting feature as it describes the general effectiveness of the finishing process that should remove deterministic patterns from the surface topography. In the standardization process of areal surface topography measurement, different approaches for quantifying topography randomness have been proposed. This paper describes a comprehensive analysis of the resulting surface anisotropy of a vibratory finishing process. Experiments are carried out by measuring the same surface area spot after various lengths of time of vibratory finishing. After a rough grind, a vibratory finishing process is applied to multiple samples and after different time steps in the finishing process, the surface topography is measured. The topography datasets are evaluated in order to determine the progression of the loss of anisotropy due to the stochastic finishing process. Several techniques to characterize the anisotropy of a surface are applied and compared. A correlational analysis to other areal surface texture parameters was performed, finding that texture aspect ratio (*Str*) was the best descriptor for directionality because it had little correlation to other parameters. The parameter had less than 40 % correlation to all other examined parameters – indicating that other effects like the change in the roughness amplitude do not falsify the correct determination of the anisotropy when the parameter is applied.

6.2 Introduction

There is a set of manufacturing processes that perform mechanical cleaning and surface treatment by abrasive action (Groover, 2012). Within this set, vibratory finishing is grouped within mass finishing operations, wherein workpieces are abraded by mixing within a vibrating bowl of abrasive media. The processes of mass finishing include barrel tumbling, vibratory finishing, vibratory shaker tumbling, roll-flow finishing, centrifugal barrel finishing, and screw rotor deburring, and these processes differ in the way the relative movements between workpieces and finishing media are achieved (Gillespie, 2007). For example, vibration induces the work and media to rub together. The type of surface effect on the workpiece is dependent on the abrasive media selected. Media can vary in shape and material, is typically smaller than five cubic centimeters (two cubic inches) and common shapes include cones, tetrahedrons, and cylinders being either ceramic, plastic, or natural minerals (Vibra Finish Company, 2018). Mass finishing is mainly applied for deburring, polishing, edge preparation, and/or surface finishing including bright and matte finishes. Additionally, compound can be used with the media to improve finish results, reduce friction, or inhibit rust (Groover, 2012).

The most important process variables in vibratory finishing are machine size and design, media size, shape, composition, absolute amount, media volume relative to part volume, compound abrasive size, material and amount, water volume and ratio-to-compound amount, and run time (Gillespie, 2007). These variables in combination effect the surface finish of the workpieces. Surface finish as an indicator of part surface smoothness has four attributes: roughness, waviness, lay, and flaws. Mass finishing processes provide a uniform surface finish and companies might

use it not to achieve a certain workpiece function but to achieve a certain appearance (Gillespie, 2007, p. 55).

The results of finishing processes can be characterized based on the measured surface topography. With the recent standard ISO 25178, the field of areal surface texture characterization is being standardized. In 2003 work on the standard ISO 25178 commenced, by the work group (WG) 16 of the ISO TC 213; identifying which features the possibilities of areal surface texture evaluation. Today, ISO 25178-2 describes the parameter for areal roughness evaluation (ISO, 2012a). With this standard, several new possibilities besides the conventional amplitude-based parameters were introduced: e.g. functional and volume-based parameters based on the areal-Abbott-curve, parameters based on the autocorrelation function, fractal evaluation and feature-based analysis (ISO, 2012a). These parameters can be applied to obtain different information on the surface and its functional properties.

The goal of this paper is to characterize the vibratory finishing processing of 25.4 mm (1in) cube 304 stainless steel blocks using quantitative surface roughness parameters; the blocks are a representative workpiece. The focus will be to quantify the anisotropy of the surface, which will utilize the parameters *Str, Std, RdMax* and the angular spectral density which is used to evaluate *Str*. Additional areal and volumetric parameters are evaluated to determine how much new information is contained in the anisotropy parameters, i.e. not included in the amplitude-based parameters. This is performed using a correlational analysis for the 20 evaluated roughness parameters.

Traditionally, high quality surface finishing follows one of the two process chains:

- Rough Grind → Fine Grind → Vibratory Finishing
- Rough Grind → Rough Media → Vibratory Finishing

The research done herein skips the second process in both chains to better exemplify the results. And if the resulting surfaces feature a low enough roughness value, there is the potential to skip a step in a finishing process chain.

The chapter continues with the following sections: 2. state of the art review of different surface roughness parameters and their use; 3. the experimental design and methodology for roughness parameter evaluation; 4. the results and discussion; and 5. the conclusions.

6.3 State of the Art

A state-of-the-art review was performed for selecting roughness parameters, for the use of roughness parameters in abrasive processes for steels, and for the use of roughness parameters in vibratory finishing.

6.3.1 Surface Parameter Selection

De Chiffre et al. (2000) and Whitehouse (2002, chap. 5) both provided simple selection matrices of various Profile surface roughness parameters for functional use; e.g. for friction, painting, fatigue, etc. Bruzzone et al. (2008) has since provided a review of various functions of an engineered surface, but did not identify the associated roughness parameters. Technological advancement has enabled the transition from profile to areal surface imaging, but the industrial implementation of areal characterization, evaluation, and the corresponding functional

applications is still in progress. Jiang and Whitehouse (2012) created a comprehensive overview of the use of various areal parameters. Thomas (2014) reviewed the usefulness of many areal surface roughness parameters in evaluating the functional performance of a surface; areas included sheet metal manufacturing, engine and transmission performance, prosthetics, and haptics. Coblas et al. (2015) identified many manufacturing techniques for generating functional textured surfaces and specific applications that utilize those surfaces. Identified domains included optics, acoustics, surface energy, mechanics, lubrication, hydrodynamics, and bioengineering. Grzeski (2016) has initiated an areal parameter equivalent of the Profile parameter selection matrices developed by De Chiffre et al. (2000) and Whitehouse (2002, chap. 5), but more applications are needed for a comprehensive approach. Hashimoto et al. (2016) created process selection guidelines that are based on desired product performance; process selection is just as important as process qualification.

It is just as important to correlate roughness parameters to functional performance as it is to manufacturing process and identifying good parameters for process evaluation. Qi et al. (2015) performed an analysis of surface texture parameters of surfaces generated by 19 different processes and found the following parameters show strong correlation, being height (*Sa/Sq*, *Sz*, *Sp*, and *Sr*), function (*Vvv*, *Vmc*, *Vmp*, *Vvc*, *Svk*, *Spk*, and *Sk*), and hybrid (*Sdq* and *Sdr*); additional parameters were investigated but showed less correlation. They then generated a parameter selection method and identified for any roughness study, either *Sa* or *Sq* should be used in addition to any other parameters. Deltombe et al. (2014) proposed a multiscale surface topography decomposition method for selecting one of 56 areal roughness parameters based on grouping parameters into 6 types. Analysis of variance (ANOVA) was performed that correlated process parameters to

roughness parameters. To find good descriptive parameters for a unit process the authors minimized the variable $F(p,\varepsilon)$, which was the between-group variability divided by the within-group variability. Das and Linke (2017) demonstrated a Profile and areal surface roughness parameter selection method for comparing differently generated surfaces that utilized statistical analysis. The method is summarized as first computing the student's-t statistic to test for significance and second computing the cross correlation coefficient to identify which significant parameter distinguishes between both surfaces.

6.4 Use in abrasive processes

Abrasive finishing processes are organized here according to Klocke and Kuchle (2009) into three areas: traditional, non-traditional, and mechanical cleaning. This review will focus on grinding, a traditional finishing process, and the mechanical cleaning processes. Table 6.1 summarizes the results found in literature, wherein studies may have identified many more surface characterizing parameters, those identified as highly significant or correlative of process characteristics were identified in the table. The review was focused on experiments carried out using steels.

Table 6.1: Areal Surface Roughness Parameters Correlated to Finishing Processes for Steels

Process	Identified Parameters	Material	Reference	Notes
Grinding	*Ssk, Sku*	Hardox 400 steel	(Krolczyk et al., 2016)	Additional parameters were identified that were still but less significant.
	Sq, Sz, Ssk, Sku, and Sbi	16MnCr5 Steel	(Kundrak et al., 2008)	Additional parameters were identified that were still but less significant.
	Sp	304 Stainless Steel	(Das and Linke, 2017)	Additional parameters were identified that were still but less significant.
Blast finishing	*Ssk, Sku*	Hardox 400 steel	(Krolczyk et al., 2016)	--- The only areal parameters identified by the authors
Shot Peening	*Sa, Sq, Sp, Sv,* and *Sz*	AISI 4340 Low-Alloy Steel	(Trung et al., 2016)	Identified relation between process parameters, i.e. pressure and shot size, and roughness parameters.
Mass Finishing	*Sq, Sal, Sds*	AISI 52100 Steel	(Hashimoto et al., 2016)	--- The only areal parameters identified by the authors

Several authors did not identify any one parameter and instead identified a larger variety of parameters for characterizing results of grinding processes. Krolczyk et al. (2016) identified the following: *Ssk, Sku, Sq, Sp, Sv, Sz,* and *Sa*. Kundrak et al. (2008) identified the following *Spk, Svk, Sk, Smr1, Smr2, Vmp, Vw, and Sbi*. Das and Linke (2017) identified *Sq, Ssk, Sku, Sp, Sv, Sz, Sa, Sk, and Svk* as having a significant change; and also identified the most significant parameters for a manufacturing process will change according to prior processing of the material.

There are many studies that investigate the effects of processing on the surface roughness and integrity, but will report out Profile *R*-values instead of more modern areal *S*-values with the reason

being common use of *R*-values, e.g., (Lachenmaier et al., 2018; X. Li et al., 2018). Therefore, this study focuses on areal roughness parameters in particular.

One notable use of angular analysis in surface roughness of steel, but not in grinding, was by Michalski (2009). Michalski (2009) utilized several surface angular analyses including power spectral density to evaluate tooth quality and surface texture direction developed from gear hobbing and Fellows chiseling. They found the texture direction to closely match the mean value of the power spectral density. In ISO 25178-2, the angular spectrum which is used to determine the texture direction of a surface is directly derived from the areal Fourier transform (ISO, 2012a) that is directly connected the power spectral density by the Parseval's theorem.

6.4.1 Vibratory Finishing Process Parameter Selection

Vibratory finishing is a popular type of mass finishing. The basic equipment configurations are rectangular tub and round bowls, which are shaken by vibratory motors, shafts with weights, or vibration generators. Processing happens in batches or continuously. Abrasive media shape affects surface roughness, material removal rate, and part edge profile in holes (Przyklenk and Schlatter, 1987). Process parameters of vibratory tumbling include: compound and soap solution, media shape, and machining time. The machining time is an optimization between burr size, edge radius, surface roughness, and size change (Gillespie, 2007). A unit manufacturing process (UMP) model is seen in Figure 6.1 depicting inputs, outputs, information, and resources.

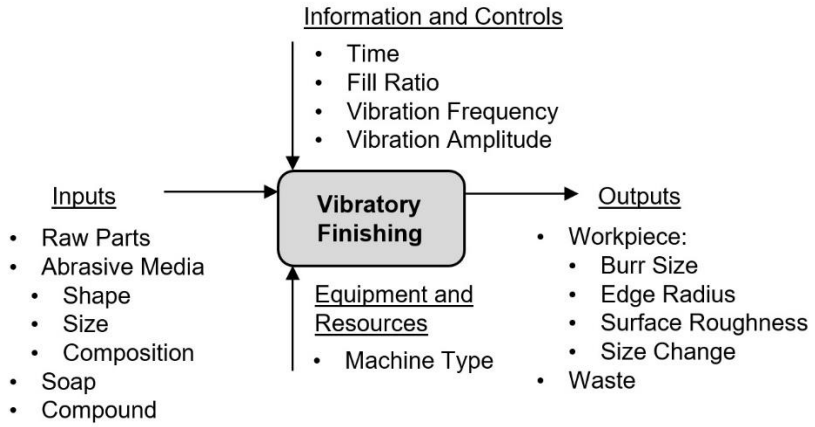

Figure 6.1: Unit manufacturing process model for vibratory finishing.

Gillespie summarizes different examples for experimental equations on burr height reduction, edge radius and surface finish improvement (as function of processing time, media size, and vibratory frequency among others). However, if large abrasive media is used, part surface roughness can even increase. (Gillespie, 2007). Additionally, Gillespie emphasizes that surface finish improvement in vibratory finishing depends upon the initial surface finish (Gillespie, 2007).

Brocker used innovative speed measurements in unguided vibratory finishing relating the power density to the process output. A large correlation exists between the equivalent power density and the material removal and edge radius, whereas surface roughness can be better explained by the abrasive media specification (Brocker, 2015). Mullany et al. (2017) modeled the vibratory finishing process using computational fluid dynamics (CFD) to predict the velocity and pressure of the media around the workpieces. The model allowed the authors to predict the surface topography of the workpiece, namely either pitting, or plowing and smoothening.

Uhlmann et al. developed a new surface roughness model for vibratory finishing depending on processing time, the initial roughness profile of the workpiece, and the material removal rate which has to be determined in preliminary tests (Uhlmann et al., 2014). The authors also stress that topographical features of the workpiece cannot be neglected for the material removal in vibratory finishing.

Hashimoto and DeBra postulate three rules: 1. A surface roughness limit is reached after a certain time (steady state) and depends mainly on the media used. 2. The rate of roughness change is proportional to the difference between roughness at a given time and roughness limit. 3. A constant stock removal rate occurs when the steady state process is reached. (Hashimoto and DeBra, 1996; Uhlmann et al., 2014).

6.5 Methodology & Experiment Design

In order to evaluate which of the areal surface texture parameters especially with regard to the directionality of the surface are useful to characterize a vibratory finishing process, different experiments were conducted. An overview of the experimental setup is given in Figure 6.2. 304 Stainless Steel surfaces were used as test coupons with a dimension of 25.4 mm (1 in) square cubes. All surfaces were pre-conditioned by grinding using Dremel 4000 hand held power tool and resin bonded alumina-sanding bands under different rotational cutting speeds ranging from 5000 rpm to 30000 rpm (Figure 6.2a). A new sanding band was used to prepare each sample for consistency. In total, 20 sample surfaces were manufactured and measured. For the smaller rotational cutting speed values 5000 and 10000, four and six samples respectively were manufactured and measured. Additionally, two samples each were manufactured and measured

for all other speed values. The pre-conditioned surfaces were further processed by a vibratory finisher (Burr King, Model 150, 60 Hz) (Figure 6.2b). The effect of finishing operation on different ground surfaces were observed over different time points ranging from 30 minute to 480 minutes. Large cone media was used as an abrasive media. All grinding operations were done by the same operator to increase the process consistency. Depending on the choice of workpiece material and abrasive media material, the chip formation process will be different; for example, the surfaces could have slightly different topography caused by varying ratios between the plowing and chipping mechanisms. This study is only investigating one combination of workpiece material, sanding band, and vibratory media.

A confocal scanning microscope (Zeiss Axio CSM 700) was used for surface characterization. A 20× magnification was applied to cover an area of 0.588 mm x 0.470 mm (Figure 6.2c). The measuring instrument is connected to a traceability chain with the aid of calibrated material measures. The measured surface topography datasets were pre-processed by removing their nominal shape based on a plane-fit which represents the F-operator as defined in ISO 25178-2 and by removing outliers of the measurements (Figure 6.2d). After this operations, *S*-filtering was applied with a linear areal-Gaussian filtering as described in ISO 16610-61 (ISO, 2015b) with a nesting index of $2.5\ \mu m$. Before the parameter evaluation was performed, an *L*-filter was applied as linear Gaussian areal. The filtering algorithm was executed with a nesting of $lc = 0.8\ mm$.

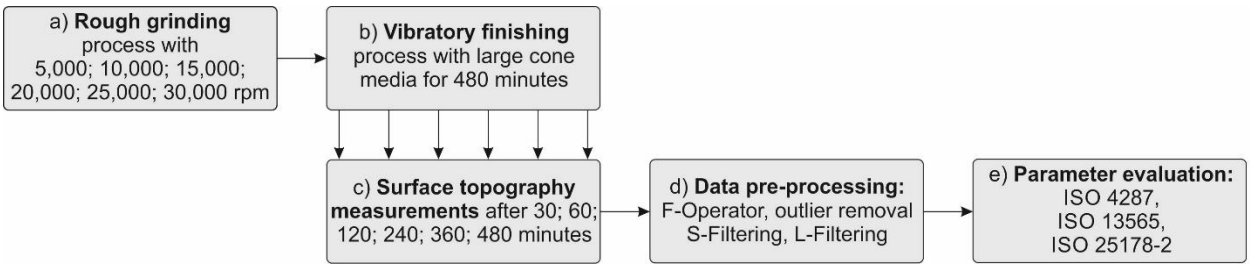

Figure 6.2: Summary of the experimental setup

After the pre-processing, different roughness parameters as defined in ISO 4287 (ISO, 1997b), ISO 13565-2 (ISO, 1996b) and ISO 25178-2 were evaluated in order to describe various properties like the anisotropy and randomness of the surface (Figure 6.2e): the profile parameters *Ra*, *Rq*, *Rt* provide general measures for the degree of surface roughness, whereas their directionality can be used to examine the directionality of the surface just as well as the solidicity ratio *K* defined by Davim (Davim, 2010) in Equation (6.1).

$$K = \frac{Rt - Rp}{Rt} . \tag{6.1}$$

As general measure for areal surface texture, the amplitude parameters, *Sa*, *Sq*, *Sz*, *Ssk* and *Sku* were calculated as defined in the corresponding standard ISO 25178-2. Additional evaluations include the volume-based parameters *Vmp*, *Vmc*, *Vvc*, *Vvv* of the areal-Abbott-curve as defined in ISO 25178-2 and the functional texture parameters *Spk*, *Sk*, *Svk* which are as well based on the areal-Abbott-curve. The hybrid parameter *Sdr* describes a measure for the total interfacial surface area (ISO, 2012a).

Additionally, in order to describe the anisotropy, the parameters based on the autocorrelation function were determined: after the calculation of the areal autocorrelation function (f_{ACF}), the directionality and periodicity was determined with a threshold value of $s=0.2$ to the f_{ACF} as defined in ISO 25178-3 (ISO, 2012b).The edges of the center area with $ACF>s$ and smallest and largest length of the corresponding area which represent the smallest and largest autocorrelation length were determined. The shortest length is the parameter autocorrelation length (*Sal*) and the quotient of the shortest and biggest length provides information about directionality as the texture aspect ratio parameter (*Str*) of ISO 25178-2 (ISO, 2012a). Further measures for the anisotropy of a rough surface can be calculated when the maximum values of the Radon-transformation of the surfaces are compared. This parameter is indicated as Rd_{Max}.

Additionally, the angular spectral density was evaluated as described in the standard ISO 25178-2. The maximum value of this spectrum ASD_{max} is determined and compared for different finishing times in order to provide another measure for the directionality of the surface. The ISO standard includes the parameter *Std* which describes the structure direction of the surface based on this maximum, however does not analyze the angular spectral density itself.

The subsequent evaluation was performed to determine which of parameter values can determine a change in the surface characteristics caused by the vibratory finishing process. Thus, the different evaluation parameters are compared.

6.6 Results & Discussion

The various surfaces of the vibratory finishing process were evaluated with different parameters. The results of the various roughness parameters are described throughout the process in order to characterize the vibratory finishing process and its influence on the surface topography. The section is divided into profile and areal evaluations.

6.6.1 Profile Evaluations

In order to describe to what extent profile evaluations can qualify the vibratory finishing process, all profiles of the measured Areal-topographies were evaluated both in x- and y-direction. The main objective of the selected evaluations is to determine the directionality of the surface using roughness parameters and thus to characterize the anisotropy of the surface. The results of all profile evaluations are summarized in Figure 6.3. A general decrease of *Ra*, *Rq* and *Rmax* can be observed independent from the original grinding process that was applied before the finishing process. This illustrates the material removal by the finishing process however does not provide any information regarding the isotropy of the surface as the general roughness decreases in both lateral directions. Examining the division of the mean values of the *Rmax*-parameter of the x- and y-direction, the isotropy of the surface can be assessed. There, to a certain degree also the loss of directionality throughout the finishing process can be monitored as the value approaches “1” throughout the process. When the mean values in both directions are identical, the surface does not feature a preferred texture direction. This represents a perfect isotropic surface. The solidicity ratio (Equation (6.1)) however gives no clear indication for loss of texture direction. In the summary in Figure 6.3, the x- and y-axis are assigned arbitrarily for the *Ra*, *Rq* and *Rmax*

determination, for the other parameters *K* and the ratio of *Rmax*, the smaller parameter value was divided by the larger parameter value.

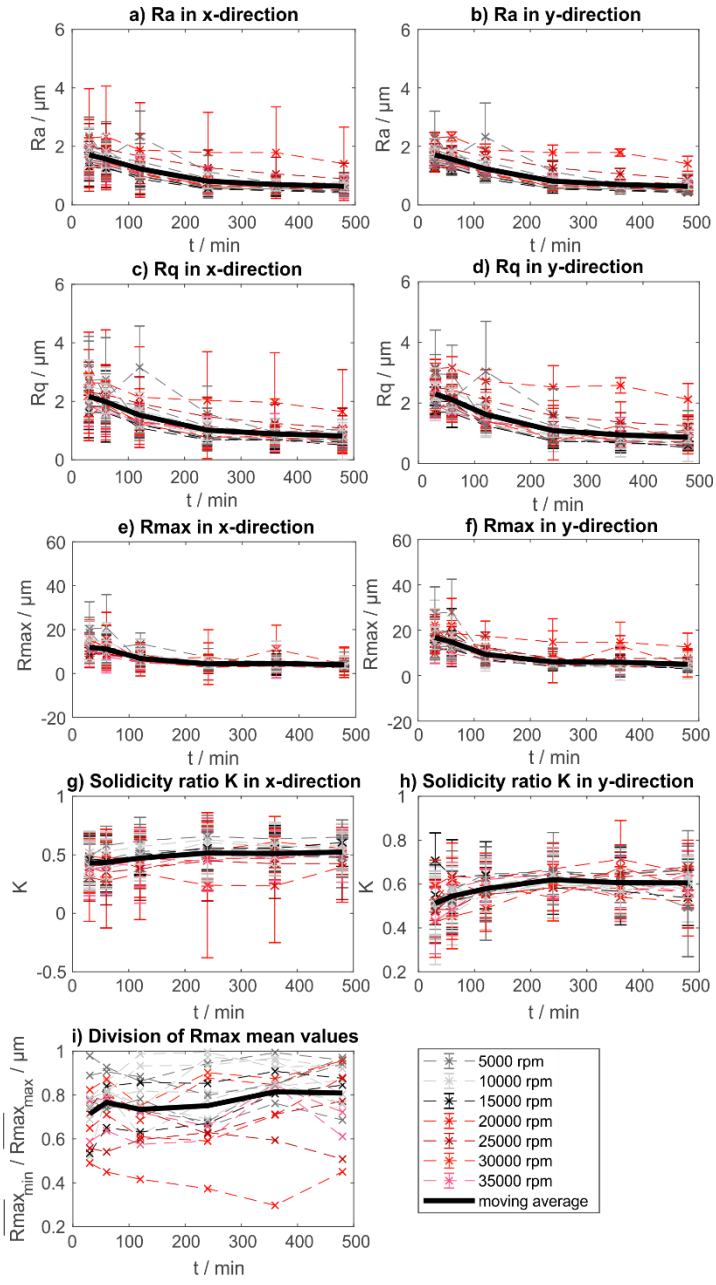

Figure 6.3: Profile parameters and their time-dependent behavior in the vibratory finishing process. The different colors indicate the rotational speed of the grinding process that was applied before the vibratory finishing. All parameters are represented as a function of the time in the vibratory finisher.

6.6.2 Areal Evaluations

The areal surface texture parameters that are related to the surface amplitude show similar results as the profile parameters and decrease through the finishing process. This is indicated in Figure 6.4 and is valid for all parameters *Sa*, *Sq* and *Sz* which are analyzed in order to describe the general decease of roughness in the areal amplitude distribution and the material removal. However, amplitude parameters do not allow conclusions regarding the anisotropy of the surfaces and provide general measure for the decreasing roughness of the surface due to the finishing process which can lead to useful information regarding the manufacturing process.

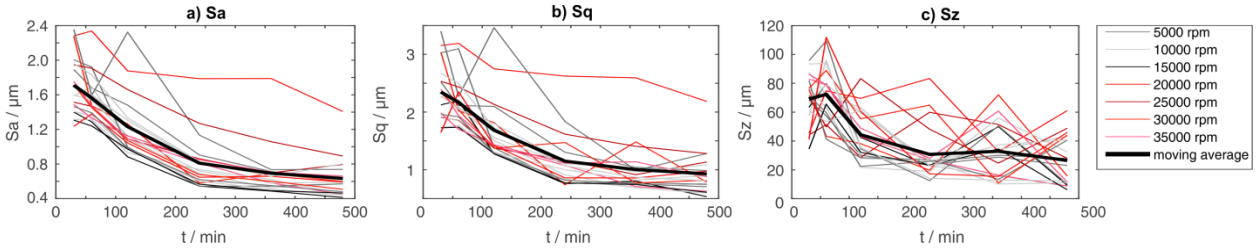

Figure 6.4: Areal amplitude parameters and their time-dependent behavior in the finishing process. The different colors indicate the rotational speed of the grinding process that was applied before the vibratory finishing. All parameters are represented as a function of the time in the vibratory finisher.

For the description of directionality and periodicity the parameters based on the f_{ACF} (Section 3) are examined and shown in Figure 6.5 and Figure 6.6. For many of the examined surfaces here, the autocorrelation length *Sal* increases. This indicates that the deterministic and periodic surface texture caused by the initial grinding process disappears throughout the finishing process. This finishing process leads to a more stochastic and anisotropic surface structure.

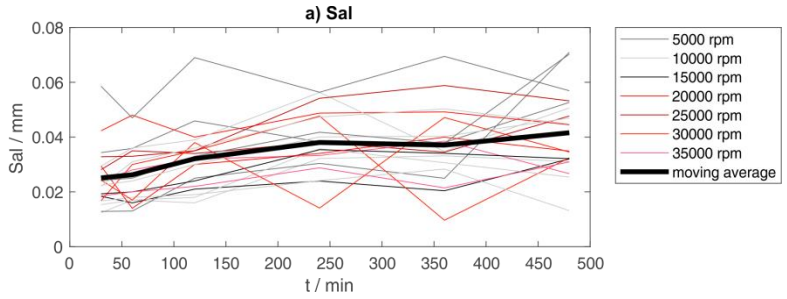

Figure 6.5: Autocorrelation length *Sal* and its time-dependent behavior in the finishing process

When the *Str*-value is examined, a clear trend towards the value of one can be observed for most samples as shown in Figure 6.6. A *Str* value equal to one represents a surface with no texture direction. This is in compliance with the observations made with the autocorrelation length (Fig. 3) and for some profile surface texture parameter evaluations (Fig. 1). The parameter *Str* gives a clear indication of the anisotropy of the surface.

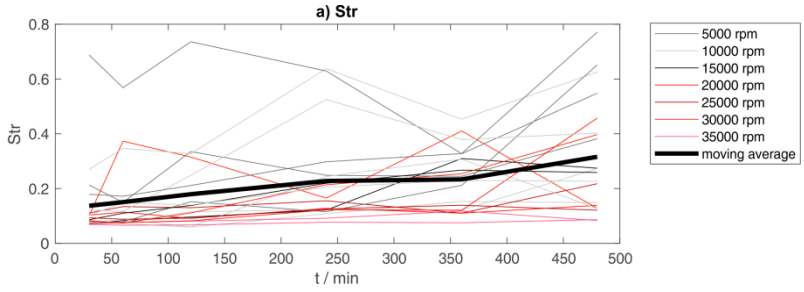

Figure 6.6: Autocorrelation ratio *Str* and its time-dependent behavior in the finishing process

The previous observations based on the roughness parameters can as well be illustrated when the surface topography itself is examined as shown in Figure 6.7. Here, the same extract of the surface topography of a sample, which was ground with 30,000 rpm, is shown after a time of 30, 120, 240 and 480 minutes of the vibratory finishing process. When the topographies are compared, it can be observed that the amplitude of the surface decreases and the surface becomes smoother

throughout the finishing. Also, the loss of directionality can be observationally confirmed as was demonstrated in the parameter values. The sample shown as an example in Figure 6.7 is representative for all other samples in the study.

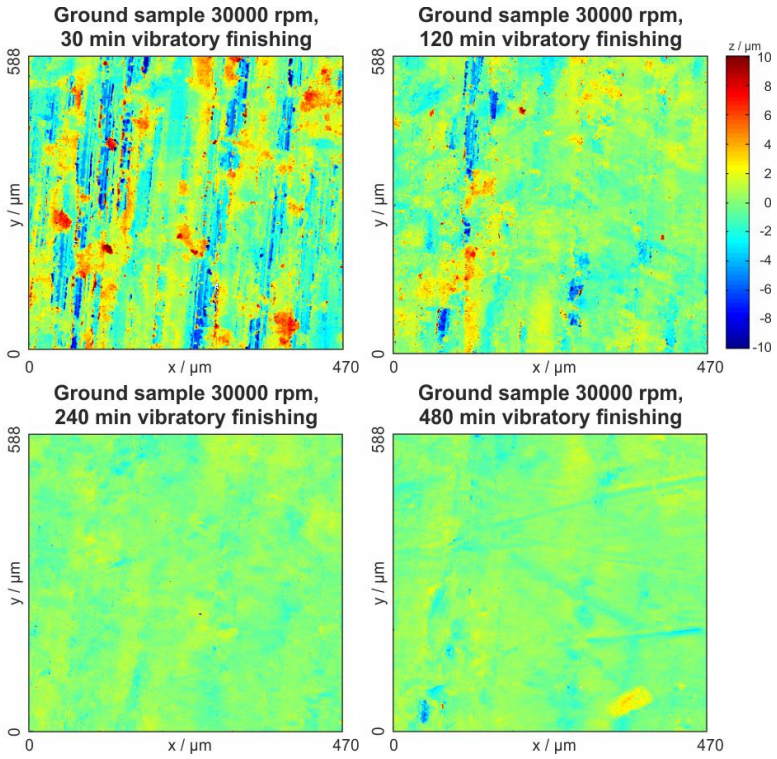

Figure 6.7: Surface topography of a sample which was ground with 30000 rpm after 30, 120, 240, 480 minutes of vibratory finishing; notice after 480 minutes striations can be seen from the abrasive media

When the volume-based parameters are examined in relation to their initial value as shown in Figure 6.8, it can be shown that all four parameters *Vmp*, *Vmc*, *Vvc* and *Vvc* decrease significantly. The peak volume decreases faster than the valley volume. This is however as well only a general indicator for the general decrease of roughness due to finishing process and does not allow any conclusions regarding the anisotropy. The decrease of the volume parameters indicates a material removal due to the finishing process and can thus characterize the general progress of the surface

finishing. After 240 minutes, the change in volume parameters is not as significant anymore which shows that the surface roughness converges to a certain threshold value and additional finishing does not create a smoother surface anymore.

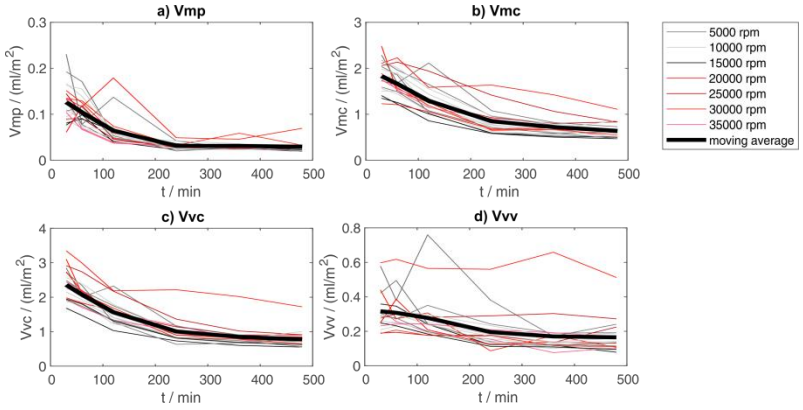

Figure 6.8: Volume-based parameters and their time-dependent behavior in the finishing process

As the volume-based parameters are also calculated based on the areal Abbott-curve, it is expected that a strong correlation to the functional surface texture parameters exists, see e.g. (Franco and Sinatora, 2015). Thus, also the values of *Sk*, *Spk*, *Svk* and the ratios *Svk / Sk* and *Spk / Sk* which describe the ratio between the core roughness and the peaks or valleys respectively can be examined. With the latter the effect of the faster decrease of peaks throughout the finishing process can be confirmed, however also with these parameters only the general decrease of roughness can be observed. The according results for all surface topographies are shown in Figure 6.9.

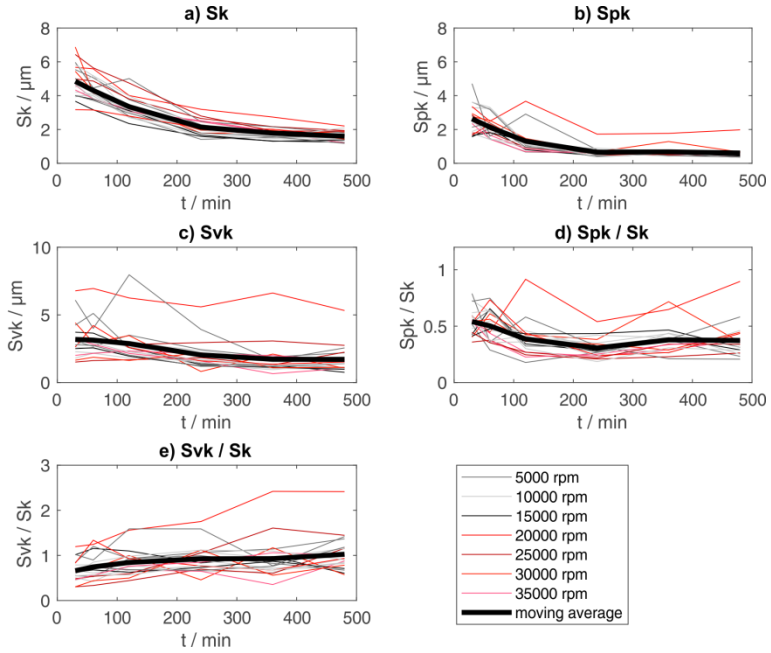

Figure 6.9: Areal functional surface texture parameters and their time-dependent behavior in the finishing process

As a hybrid parameter, *Sdr* was examined. The results are shown in Figure 6.10. Again, this parameter can provide information that the total interfacial surface area decreases throughout the finishing process. However, no information regarding the directionality can be extracted from the results.

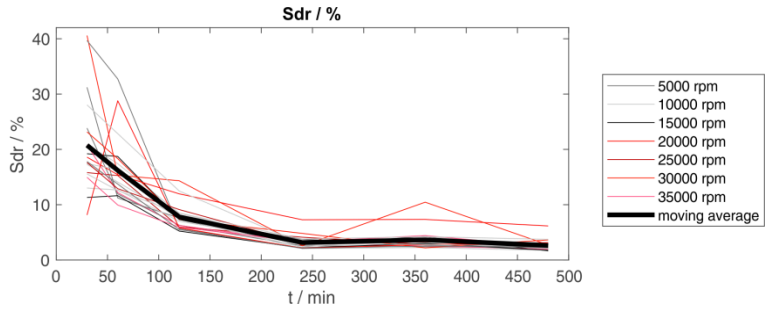

Figure 6.10: Parameter *Sdr* and its time-dependent behavior in the finishing process

Another parameter which can be specifically applied for the evaluation of the directionality is the maximum of the Radon-transform. The corresponding parameter values are imaged as a function of the vibratory finishing time in Figure 6.11. Here, the decrease also indicates that the angle distribution of the surface is becoming more homogenous and the directionality is removed in the course of the finishing process. Thus, this parameter can additionally be identified as a measure for the anisotropy of the surface.

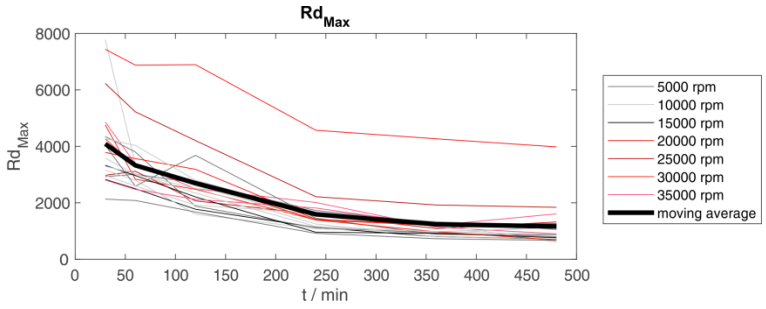

Figure 6.11: Parameter *Rd_{Max}* and its time-dependent behavior in the finishing process

The maximum of the angular spectral density *ASD_{Max}* which serves for the evaluation of the *Str* parameter in ISO 25178-2 was evaluated as another directionality measure. The results are displayed in Figure 6.12. Here, also a decrease of the maximum of the spectrum can be observed which corresponds with the previous observations.

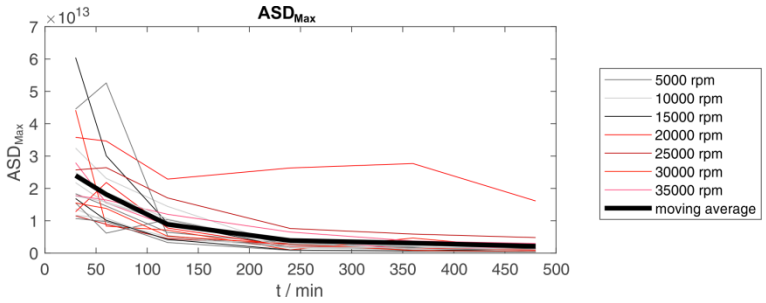

Figure 6.12: Parameter *ASD_{Max}* and its time-dependent behavior in the finishing process

As the absolute values of the described angular spectrum and the radon transform are also influenced by the amplitude values of the surface, within a correlation analysis the different parameters are correlated in order to describe to what extent new information is provided by the different measures.

For most parameters, a stochastic scattering of the individual values could be observed to some extent. However, when the trend of the moving average of all 20 evaluations is determined, for many parameters a clear trend becomes observable - indicating the reproducibility of the results. In order to determine additional information regarding the relation between the various examined areal surface texture parameters, the correlation is evaluated.

6.6.3 Correlation Analysis of areal surface texture parameters

After different areal surface roughness parameters have been evaluated, the correlation between the different parameters is of interest as it was shown that similar information regarding the directionality and the general degree of roughness can for example be found in various parameter evaluations. The correlation analysis of the areal parameters is shown in Table 6.2. The parameters *Str*, ASD_{Max} and Rd_{Max} contained relevant information regarding the anisotropy of the surfaces. Other parameters were solely able to describe the change in the amplitude or the volume removal due to the finishing process.

This correlation analysis leads to the following results: between *Sa* and *Sq* a strong correlation exists, as they are both calculated based on the amplitude distribution of the topography. The

volume parameters are strongly correlated with each other and with *Sa*, *Sq*, *Sk*, *Spk*, *Svk*, *Sdr*. As the parameters *Sk*, and *Spk* are based as well on the Abbott-curve, this correlation is typical. *Svk* is analogously correlated with the volume parameter *Vvv*. The correlation of the functional roughness parameters is in compliance to previous examinations in this field (Pawlus et al., 2009).

Std does also not strongly correlate to any other of the evaluated areal parameter as it describes the preferred angle of the surface which is not related to other properties defined by the surface topography height values. The autocorrelation parameters *Sal* and *Str* do not correlate with other parameters and thus provide new information regarding the periodicity and directionality of the surface texture. However, this also confirms the previous results that quantifying the anisotropy is best possible with *Str*. The value of Rd_{Max} also gives a measure for directionality, however as the parameter is strongly correlated with *Sa* and *Sq* the decrease of the values of Rd_{Max} is mainly caused by the decrease in amplitude not in directionality. Thus it can be concluded that *Str* is the best suitable parameter for an anisotropy analysis.

Table 6.2: Correlation analysis of areal surface texture parameters, red: strong positive or negative correlation, green: no correlation

	Sa	Sq	Sz	Sal	Str	Vmp	Vmc	Vvc	Vvv	Ssk	Sku	Sk	Spk	Svk	Spk / Sk	Svk / Sk	Sdr	Std	RdMax	ASDMax
Sa	1.00	0.98	0.68	-0.11	-0.20	0.87	0.98	0.97	0.84	0.32	-0.26	0.94	0.89	0.81	0.55	0.06	0.81	0.08	0.88	0.79
Sq		1.00	0.73	-0.13	-0.14	0.88	0.93	0.94	0.88	0.20	-0.16	0.89	0.90	0.86	0.62	0.17	0.83	0.11	0.86	0.81
Sz			1.00	-0.48	-0.30	0.73	0.68	0.69	0.49	-0.06	0.15	0.67	0.73	0.46	0.61	-0.03	0.78	-0.02	0.64	0.68
Sal				1.00	0.63	-0.28	-0.17	-0.20	0.14	0.13	-0.24	-0.23	-0.25	0.15	-0.24	0.39	-0.41	0.27	-0.18	-0.35
Str					1.00	-0.16	-0.24	-0.28	0.01	-0.25	0.15	-0.26	-0.17	0.04	-0.04	0.28	-0.25	0.25	-0.36	-0.39
Vmp						1.00	0.85	0.87	0.64	0.28	-0.18	0.86	0.99	0.61	0.76	-0.11	0.90	0.01	0.80	0.73
Vmc							1.00	0.97	0.72	0.36	-0.27	0.97	0.86	0.68	0.46	-0.12	0.82	0.05	0.84	0.75
Vvc								1.00	0.73	0.36	-0.26	0.97	0.89	0.70	0.53	-0.09	0.83	0.02	0.90	0.78
Vvv									1.00	0.14	-0.19	0.62	0.69	0.99	0.55	0.55	0.56	0.18	0.73	0.68
Ssk										1.00	-0.96	0.37	0.28	0.10	0.07	-0.26	0.20	-0.04	0.32	0.20
Sku											1.00	-0.26	-0.18	-0.15	-0.02	0.09	-0.12	-0.02	-0.22	-0.15
Sk												1.00	0.86	0.59	0.43	-0.25	0.83	0.03	0.83	0.72
Spk													1.00	0.67	0.79	-0.04	0.88	0.01	0.83	0.75
Svk														1.00	0.55	0.58	0.53	0.17	0.72	0.66
Spk / Sk															1.00	0.26	0.63	-0.05	0.57	0.55
Svk / Sk																1.00	-0.15	0.19	0.06	0.09
Sdr																	1.00	-0.03	0.70	0.81
Std																		1.00	-0.02	-0.04
RdMax																			1.00	0.79
ASDMax																				1.00

6.7 Conclusions

Abrasive processes have been characterized with numerous approaches but not often with regard to directionality. Surfaces of 304 stainless steel processed by vibratory finishing are examined by applying different profile and areal surface texture parameters. In doing so, besides a general description of the impact of the process on the surface topography, the aspect of directionality was the topic of concern. It was expected that due to the finishing process, the surface will become less isotropic. This was also quantified with the ratio of profile parameters in the different lateral directions. From the areal surface texture parameters, *Str* was best suitable to characterize the anisotropy of the surface. It could be confirmed that the amplitude, functional, volume-based and hybrid parameters were able to generally characterize the impact of the finishing process on the surface, but based on a correlation analysis it was shown that the *Str* parameter is not strongly related to the other examined areal surface texture parameters. Thus, the *Str* parameter was proven to be the most reliable way to characterize the directionality of the examined vibratory finished surfaces. Other directionality measures like the maximum of the angular spectral density or the Radon transform also include effects based on the amplitude distribution.

Chapter 7: Conclusions

Sustainable engineering design and manufacturing is a growing research topic, that has expanded to include more ideas over the years as more people address sustainability challenges. The most recent developments in the field is pushing design of products and businesses into the circular economy concept; which is a growing idea that the economy should not have wastes but instead resources should flow circularly from the output of one process to the input of another process. From a regulatory perspective, extended producer responsibility laws have also been enacted along side the design methodologies, which requires product manufacturers to carry the monitory burden of disposing of their products or to restrict the materials used within their products. The circular economy is a long-term goal for our economy and more broadly to for our world, but there are many steps along the way to achieving that goal. Within this circular economy methodology, reduction of resources is an important consideration in which this dissertation would reside. Addressing energy consumption in manufacturing is a key performance indicator and energy is a key resource that can be addressed though engineering design. Product quality is a factor that may not be purposely overlooked, but is often not incorporated into sustainable methodologies. The combination of energy consumption and product quality helps to meet business needs.

7.1 Summary

The research reported herein was undertaken to advance manufacturing science in grinding machine energy consumption and surface roughness output of those machines. Because there often exists tradeoffs and compromises in engineering, design, and manufacturing, investigations are needed to determine what these tradeoffs are and how they can be quantified. Thus, the objective

of the work reported was to provide a methodology into energy efficient manufacturing and quantifying the tradeoffs in terms of surface roughness.

In whole, this research provided physics-based models of grinding machine tools and abrasive processes that lead to more energy-efficient machine tools design. By identifying the machine tool components, systems, and resulting quality, as set out by the research questions, energy efficient design is addressed from a life-cycle perspective; with focuses on manufacturing and use phase of the machine tools. The manufacturing phase investigated embodied energy of a machine tool's motors, while the use phase investigated energy consumption of a machine tool's motors. The use phase also addressed the effects of compromising on energy consumption, which is the reduced quality impacts on product workpieces. Thus, a trade-off exists between reducing energy consumption in the use phase of a machine tool and the quality output, which could have long-term impacts on energy consumption in the machines created using the created workpieces.

Energy consumption in grinding machines was investigated from several perspectives. First, a method for applying sustainability principles using axiomatic design into machine feed drives was created. Second, a method for assessing the energy consumed in manufacturing a machine tool motor was created to analyze the tradeoffs between using a pump motor and gravity. Third, the energy consumption the startup of a spindle motor was investigated to determine if there exists a minimum, and a method for minimizing the spindles start costs. Fourth, the tradeoff between energy consumption and surface roughness was investigated for a grinding machine tool. Finally, an investigation into the information contained within the areal surface roughness parameters was

performed, this was used to determine what repeat information exists in areal surface roughness parameters.

7.2 Conclusions

Learnings from this research support sustainable machine tool design and workpiece quality as follows: 1) Several studies have employed axiomatic design to design machine tools, the integration of a new sustainability axiom had yet to be accomplished but it can be done. 2) A comprehensive review of life cycle inventory (LCI) models of electric motors was needed; design factors can play a large influence on constituent material composition and the resulting embodied energy. 3) Peak load leveling can be at odds with energy minimization in motor starting; findings indicate that minimized energy consumption occurred near maximum power consumption. 4) A tradeoff exists between grinding machine energy consumption and workpiece surface roughness; this tradeoff is important when deciding if minimizing manufacturing or use phase energy consumption reduces overall energy consumption. 5) Information contained in surface roughness parameters is often repetitive, not all roughness parameters are needed to characterize a surface.

First, the review of studies that applied axiomatic design onto machine tool technology highlighted that the research area needed further investigation. Furthermore, a methodology was developed to incorporate sustainability principles into axiomatic design. Applying different sustainability principles into the axiomatic design methodology could have differing impacts on the objectives of the design. Expanding developed engineering design methodologies to incorporate sustainable principles is critical for the acceptance of sustainability into engineering design curricula and practice.

Second, while many authors have published life cycle assessments and life cycle inventories on electric motors, none had performed a literature review on the subject. Thus, a review the LCI literature for electric motors and an assessment method for electric motor energy consumption was created. Depending on the design criteria of the motor in question, motors can have vastly different embodied energy results, including motor type and size, and the incorporation of rare earth magnets. The creation of the method allows designers to easily compare incorporate embedded energy into motor selection.

Third, when attempting to optimize energy consumption to minimize manufacturing costs, a pareto rule can be employed to identify the most important machines to first optimize energy consumption. The investigation into peak load leveling and energy consumption revealed that either the energy could be minimized or the peak power load could be minimized. The example investigated a fairly small machine tool spindle, but depending on the size of the manufacturing facility performing this optimization could have strong impacts to monthly electricity costs. Furthermore, applying the same technique to motors with much larger loads could result in large electricity cost savings; additionally, the tradeoff between minimizing energy vs peak power becomes more important as motor inertial load rises.

Fourth, an investigatory study was performed to determine if any tradeoff exists between machine tool energy consumption and workpiece surface roughness. The findings indicate that increased energy consumption would result in lower surface roughness. Furthermore, the study also investigated the difference in measured energy consumption between electricity measurement and

force measurement of the grinding spindle. This revealed that electricity consumption can be significantly higher than the process energy, by several hundred percent difference.

Fifth, workpiece quality can be evaluated using roughness parameters, R-value profile parameters, S-value areal parameters, or V-value volume parameters. A study evaluated 20 different areal and volume roughness parameters to determine if the parameters contained repetitive information. Evaluating all of the roughness parameters is likely not necessary as many of the parameters correlated with each other, but depending on the surface and function a smaller group could be evaluated.

7.3 Contributions

The presented work focuses on energy consumption in grinding machines and workpiece surface roughness for sustainable design and manufacturing assessments and has made the following contributions to the community.

Contribution 1: A road map for investigating sustainability using axiomatic design., and an evaluation of energy consumption in a machine tool feed drive was performed. The evaluation allows designers to compare energy consumed for a machine tool during the use phase.

Contribution 2: A review of LCI studies for electric motors was performed and a methodology for evaluating the embodied energy of an electric motor was created. The method enables designers to compare different motor types in terms of manufacturing energy when selecting a motor.

Contribution 3: A method for finding a minimum value for either energy or power, and the impact of electricity costs was presented. This method can be used to evaluate any sized electric motor during a power-on event.

Contribution 4: A study was performed to find any relationship between energy consumption and workpiece surface roughness. The findings showed that a tradeoff exists, lower surface roughness uses more of both process work and electricity.

Contribution 5: A study was performed to determine if surface roughness parameters contain repetitive information. It was found that many are correlated with each other and not all are needed to evaluate workpiece surface quality.

7.4 Opportunities for Future Research

There are several opportunities for future research as a result of this work. First, future work can expand upon the axiomatic design sustainability axioms investigated herein and evaluate multiple different examples and evaluate different sustainability criteria. Second, a machine tool could be designed entirely from the ground up using the sustainability principles applied herein and those explored by other researchers. The work herein evaluated mainly the feed, drive, and motor components of an existing machine tools, whereas a ground up approach could result in novel ideas. Third, this work mainly performed experimental studies to evaluate workpiece surface roughness, a computational approach could follow to enable prediction of workpiece roughness.

Opportunity 1: The sustainable axioms developed for axiomatic design in Chapter 2: were identified form literature as a method to incorporate sustainability into the method of axiomatic design. As part of axiomatic design, the axioms were developed over a number of years and were disproven using case studies and example problems; the same also has to be for the set of sustainability axioms generated in this work. It is possible for a hypothetical axiom to be proven false, but it is not possible to prove an axiom true. Thus, to incorporate sustainability into axiomatic design the axioms need to be evaluated rigorously using a large set of applications.

Opportunity 2: The work presented in Chapters 2, 3 and 4 all present energy-evaluation methods and evaluations of existing grinding machine tools. Taking the approach to design a novel machine tool would present innovations that were not possible to explore herein. This could include applying structural design light weighting principles to a machine tool, evaluating incorporated energy recovery and storage mechanisms within the machine tool, and modeling the machine tool's environment to best optimize the energy consumption of the auxiliary-mechanisms to meet the needs of the process-mechanisms.

Opportunity 3: The surface roughness evaluations and characterization performed in Chapters 5 and 6 are limited in scope to experimental evaluations. Future work in this research area would provide models and methods to predict workpiece surface roughness of a component via computational computer simulation. A specific set and value of surface roughness parameters could be input into a model and result in the required processing steps. The selection and evaluation of surface roughness parameters still requires a knowledgeable expert, but such a system could lower the bar for training and knowledge requirements for engineering designers.

7.5 Last Remarks

The body of work herein makes incremental improvements in sustainable engineering design and manufacturing decision making, and improves understanding in energy efficiency and workpiece quality. By providing methods for evaluating and improving energy consumption in manufacturing, manufacturers, suppliers, designers, OEMs, and other people that participate in the production economy can better determine and communicate the energy impacts of their products and identify tradeoffs between manufacturing phase and use phase impacts. Sustainable production can move forward with the methods described herein to assess energy consumption in manufacturing process at more detailed levels. This work was performed to improve our society and any beneficial impact, no matter how small, is seen as successful progress.

List of Publications and Submitted Manuscripts

1. **Garretson, I.C.**, Peukert, B., Uhlmann, E., Linke, B.S., 2017, "Axiomatic Design of a Sustainable Machine Tool," *Proceedings of the ASME 2017 International Manufacturing Science and Engineering Conference (MSEC)*, June 4-8, Los Angeles, CA, USA. https://doi.org/10.1115/MSEC2017-2874
2. Linke B.S., **Garretson, I.C.**, Torner, F., Seewig, J., 2017, "Grinding Energy Modeling Based on Friction, Plowing and Shearing," *Journal of Manufacturing Science and Engineering.* https://doi.org/10.1115/1.4037239
3. Linke, B.S., **Garretson, I.C**, Fahad M.J., Hafez, M.M., "Integrated Design, Manufacturing and Analysis of Airfoil and Nozzle Shapes in an Undergraduate Course," *Proceedings of the SME 2017 North American Manufacturing Research Conference (NAMRC)*, June 4-8, Los Angeles, CA, USA. https://doi.org/10.1016/j.promfg.2017.07.098
4. Linke, B.S., **Garretson, I.C**, Fahad M.J., Martin, M.L., Hafez, M.M., "Design and Manufacturing of Nozzles and Airfoil Shapes for Compressible Flow Visualizations in a New Engineering Course," *2017 ASEE Annual Conference & Exposition*, Columbus, Ohio. https://peer.asee.org/27938
5. Bernstein W.Z., Subramaniyan A.B., Brodsky, A., **Garretson, I.C.**, Haapala, K.R., Libes, D., Morris, K.C., Pan, R., Prabhu, V., Sarkar, A., Raman, A.S, Wu Z., 2018. Roadmapping the Unit Manufacturing Process Repository: A Collaborative Vision. *Manufacturing Letters.* https://doi.org/10.1016/j.mfglet.2017.12.007
6. Hafez, M., Fahad J., Linke B., **Garretson, I.C.,** 2018, "Hydraulic Analogy and Visualization of Two-Dimensional Compressible Fluid Flows, Part 2 Water Table Experiments," *International Journal of Aerodynamics*. https://doi.org/10.1504/IJAD.2018.089775

7. Voet, H., **Garretson, I.C**., Falk, B., Schmitt, R.H., Linke, B.S., 2018, "Peak Power Load and Energy Costs Using the Example of the Startup of a Grinding Machine," *Procedia CIRP*. *https://doi.org/10.1016/j.procir.2017.11.044*

8. Linke, B.S., Garcia, D.R.., Kamath, A., **Garretson, I.C.** 2019. "Examples of Data-driven Sustainability in Manufacturing," *Procedia CIRP*. https://doi.org/10.1016/j.promfg.2019.04.075

9. Linke, B.S., Martin, L., **Garretson, I.C.,** *2019* "Learning Benefits by Integrating Design, Manufacturing, and Testing in a Course for Compressible Flow Visualizations," *International Journal of Mechanical Engineering Education.* https://doi.org/10.1177%2F0306419019838279

10. **Garretson, I.C.**, Torner, F.M., Seewig, J., Linke, B.S., *2019.* "Comparison of Algorithms for Measuring Water Height of a Water Table," *Journal of Metrology.* *https://doi.org/10.1016/j.measurement.2019.106854*

11. Eifler M., **Garretson I.C.**, Torner, F., Seewig, J., Das, J., Linke B.S., *2019*. "Effects of Vibratory Finishing of 304 Stainless Steel Samples on Areal Roughness Parameters: An Analysis for Anisotropy Parameters," *Journal of Materials Processing Technology*. *https://doi.org/10.1016/j.jmatprotec.2019.116256*

12. **Garretson, I.C.,** Guo, Q., Linke, B.S., *To Be Presented in August 2021* "Design Analysis of a Machine Tool Stand, and Energy Comparison Between Gravity Fed Coolant System and a Pumped System." *Proceedings of the 2021 ASME IDETC/CIE: 26th Design for Manufacturing and the Lifecycle Conference (DFMLC).*

13. **Garretson, I.C.,** Seibt, M., Schmitt, R.H., Linke, B.S., *To be Submitted.* "Energy Consumption and Workpiece Surface Roughness Tradeoff in a Grinding Machine, A Study with Cold Air Coolant." *International Journal of Advanced Manufacturing Technology*
14. Roeth, A.A., **Garretson, I.C.,** Beltz, M., Herbold, T., Schulze-Hagen, M., Quaisser, S., Georgens, A., Reith, D., Slabu, I, Neumann, U.P., Linke, B.S., *To be Submitted.* "Pre-clinical Optimization of Endoscopic Tumor Treatment with Magnetic Nanoparticles by use of 3D Printed Models and Porcine Explants."
15. Reisinger T., **Garretson, I.C.,** Linke, B.S., *To be Submitted,* "Reusable Unit Process Life Cycle Inventory for Manufacturing – Vibratory Finishing." *Production Engineering*

References

ABB, 2018a. Baldor-Reliance CA501: Standard Motor Product Catalogue.

ABB, 2018b. Motion Control Packages: e-Series Motors Product Catalogue.

Altintas, Y., Brecher, C., Weck, M., Witt, S., 2005. Virtual Machine Tool. CIRP Annals 54, 115–138. https://doi.org/10.1016/S0007-8506(07)60022-5

Altintas, Y., Weck, M., 2004. Chatter Stability of Metal Cutting and Grinding. CIRP Annals 53, 619–642. https://doi.org/10.1016/S0007-8506(07)60032-8

Andrada, P., Blanqué, B., Martínez, E., Perat, J.I., Sánchez, J.A., Torrent, M., 2012. Environmental and life cycle cost analysis of one switched reluctance motor drive and two inverter-fed induction motor drives. IET Electr. Power Appl. 6, 390. https://doi.org/10.1049/iet-epa.2011.0320

ANSYS Inc., 2020a. ANSYS Mechanical User Guide.

ANSYS Inc., 2020b. ANSYS Meshing User Guide.

ANSYS Inc., n.d. ANSYS Academic Research Mechanical, Release 19.2 and Release 20.

Apostolos, F., Alexios, P., Georgios, P., Panagiotis, S., George, C., 2013. Energy Efficiency of Manufacturing Processes: A Critical Review. Procedia CIRP, Forty Sixth CIRP Conference on Manufacturing Systems 2013 7, 628–633. https://doi.org/10.1016/j.procir.2013.06.044

Aurich, J.C., Linke, B., Hauschild, M., Carrella, M., Kirsch, B., 2013. Sustainability of abrasive processes. CIRP Annals - Manufacturing Technology 62, 653–672. https://doi.org/10.1016/j.cirp.2013.05.010

Avram, O.I., Xirouchakis, P., 2011. Evaluating the use phase energy requirements of a machine tool system. Journal of Cleaner Production 19, 699–711. https://doi.org/10.1016/j.jclepro.2010.10.010

Azapagic, A., Millington, A., Collett, A., 2006. A Methodology for Integrating Sustainability Considerations into Process Design. Chemical Engineering Research and Design 84, 439–452. https://doi.org/10.1205/cherd05007

Böhner, J., Hamacher, M., Reger, A., Steinhilper, R., 2014. Derivation of Measures for Energy Efficient Machine Design by Evaluating Energy Consumption Data. Procedia CIRP 15, 437–442. https://doi.org/10.1016/j.procir.2014.06.062

Boughanmi, W., Manata, J.P., Roger, D., Jacq, T., Streiff, F., 2012. Life cycle assessment of a three-phase electrical machine in continuous operation. IET Electr. Power Appl. 6, 277. https://doi.org/10.1049/iet-epa.2011.0219

Bovea, M.D., Pérez-Belis, V., 2012. A taxonomy of ecodesign tools for integrating environmental requirements into the product design process. Journal of Cleaner Production 20, 61–71. https://doi.org/10.1016/j.jclepro.2011.07.012

Bräunig, M., Regel, J., Glänzel, J., Putz, M., 2019. Effects of cooling lubricant on the thermal regime in the working space of machine tools. Procedia Manufacturing, Sustainable Manufacturing for Global Circular Economy: Proceedings of the 16th Global Conference on Sustainable Manufacturing 33, 327–334. https://doi.org/10.1016/j.promfg.2019.04.040

Brocker, R., 2015. Relativgeschwindigkeiten und Kontaktkräfte beim ungeführten Vibrationsgleitschleifen. Apprimus Verlag, Aachen.

Brundtland, G.H., 1987. Our Common Future, World Commission on Environment and Development (WCED). Oxford University Press.

Bruzzone, A.A.G., Costa, H.L., Lonardo, P.M., Lucca, D.A., 2008. Advances in engineered surfaces for functional performance. CIRP Annals 57, 750–769. https://doi.org/10.1016/j.cirp.2008.09.003

Cearsolo, X., Cabanes, I., Sánchez, J.A., Pombo, I., Portillo, E., 2016. Dry-dressing for ecological grinding. Journal of Cleaner Production 135, 633–643. https://doi.org/10.1016/j.jclepro.2016.06.117

Chapman, S.J., 1999. Electric Machinery Fundamentals, 3rd ed. MCGraw-Hill.

Chiu, M.C., Chu, C.H., 2012. Review of Sustainable Product Design from Life Cycle Perspectives. INTERNATIONAL JOURNAL OF PRECISION ENGINEERING AND MANUFACTURING 13, 1259–1272.

Chiu, M.C., Kremer, G.E.O., 2011. Investigation of the Applicability of Design for X Tools during Design Concept Evolution: a Literature Review. International Journal of Product Development 13, 132–167. https://doi.org/10.1504/IJPD.2011.038869

Choi, A.C.K., Kaebernick, H., Lai, W.H., 1997. Manufacturing Processes Modelling for Environmental Impact Assessment. Journal of Materials Processing Technology 70, 231–238. https://doi.org/16/S0924-0136(97)00067-8

Choi, H.Z., Lee, S.W., Jeong, H.D., 2001. A comparison of the cooling effects of compressed cold air and coolant for cylindrical grinding with a CBN wheel. Journal of Materials Processing Technology, International symposium on advanced forming and die manufacturing technology 111, 265–268. https://doi.org/10.1016/S0924-0136(01)00531-3

Coblas, D.G., Fatu, A., Maoui, A., Hajjam, M., 2015. Manufacturing textured surfaces: State of art and recent developments. Proceedings of the Institution of Mechanical Engineers, Part J: Journal of Engineering Tribology 229, 3–29. https://doi.org/10.1177/1350650114542242

Dahmus, J.B., Gutowski, T.G., 2004. An Environmental Analysis of Machining, in: ASME 2004 International Mechanical Engineering Congress and Exposition (IMECE2004). Anaheim, CA, pp. 643–652. https://doi.org/10.1115/IMECE2004-62600

Das, J., Linke, B., 2017. Evaluation and systematic selection of significant multi-scale surface roughness parameters (SRPs) as process monitoring index. Journal of Materials Processing Technology 244, 157–165. https://doi.org/10.1016/j.jmatprotec.2017.01.017

Davim, J.P. (Ed.), 2010. Surface integrity in machining. Springer, New York ; London.

de Almeida, A.T., Ferreira, F.J.T.E., Baoming, G., 2014. Beyond Induction Motors—Technology Trends to Move Up Efficiency. IEEE Trans. on Ind. Applicat. 50, 2103–2114. https://doi.org/10.1109/TIA.2013.2288425

De Chiffre, L., Lonardo, P., Trumpold, H., Lucca, D.A., Goch, G., Brown, C.A., Raja, J., Hansen, H.N., 2000. Quantitative Characterisation of Surface Texture. CIRP Annals 49, 635–652. https://doi.org/10.1016/S0007-8506(07)63458-1

De Filippi, A., Ippolito, R., Micheletti, G.F., 1981. NC Machine Tools as Electric Energy Users. CIRP Annals 30, 323–326. https://doi.org/10.1016/S0007-8506(07)60950-0

Deltombe, R., Kubiak, K.J., Bigerelle, M., 2014. How to select the most relevant 3D roughness parameters of a surface: Relevance of 3D roughness parameters. Scanning 36, 150–160. https://doi.org/10.1002/sca.21113

Denkena, B., Reichstein, M., Kramer, N., Jacobsen, J., Jung, M., 2005. Eco- and Energy-Efficient Grinding Processes. Key Engineering Materials 291–292, 39–44. https://doi.org/10.4028/www.scientific.net/KEM.291-292.39

Diaz, N., Choi, S., Helu, M., Chen, Y., Jayanthan, S., Yasui, Y., Kong, D., Pavanaskar, S., Dornfeld, D., 2010. Machine Tool Design and Operation Strategies for Green Manufacturing 7.

DOC, U.D. of C., 2013. NIST Sustainable Manufacturing Indicators Repository [WWW Document]. URL http://www.mel.nist.gov/msid/SMIR/Indicator_Repository.html (accessed 9.24.13).

DOE, U.D. of E., 2010. Manufacturing Energy and Carbon Frootprints (No. 2010 MECS).

Dornfeld, D., Wright, P., 2007. "Technology Wedges" for Implementing Green Manufacturing. Transactions of NAMRI/SME 35.

Duflou, J.R., Kellens, K., Dewulf, W., 2011. Unit Process Impact Assessment for Discrete Part Manufacturing: A State of the Art. CIRP Journal of Manufacturing Science and Technology, Energy-Efficient Product and Process Innovations in Production Engineering 4, 129–135. https://doi.org/10.1016/j.cirpj.2011.01.008

Duflou, J.R., Sutherland, J.W., Dornfeld, D., Herrmann, C., Jeswiet, J., Kara, S., Hauschild, M., Kellens, K., 2012. Towards Energy and Resource Efficient Manufacturing: A Processes and Systems Approach. CIRP Annals - Manufacturing Technology 61, 587–609. https://doi.org/10.1016/j.cirp.2012.05.002

Engelbeen, F., n.d. Plastics - Environmental aspects [WWW Document]. URL http://wgbis.ces.iisc.ernet.in/envis/plasdoc612.html (accessed 3.8.21).

Eurostat, 2017. Consumption of energy - Statistics Explained [WWW Document]. URL http://ec.europa.eu/eurostat/statistics-explained/index.php/Consumption_of_energy (accessed 10.16.16).

Ferreira, F.J.T.E., Fong, J.A.C., de Almeida, A.T., 2011. Ecoanalysis of Variable-Speed Drives for Flow Regulation in Pumping Systems. IEEE Trans. Ind. Electron. 58, 2117–2125. https://doi.org/10.1109/TIE.2010.2057232

Ferreira, F.J.T.E., Leprettre, B., de Almeida, A.T., 2016. Comparison of Protection Requirements in IE2-, IE3-, and IE4-Class Motors. IEEE Trans. on Ind. Applicat. 52, 3603–3610. https://doi.org/10.1109/TIA.2016.2545647

Franco, L.A., Sinatora, A., 2015. 3D surface parameters (ISO 25178-2): Actual meaning of Spk and its relationship to Vmp. Precision Engineering 40, 106–111. https://doi.org/10.1016/j.precisioneng.2014.10.011

Fraunhofer ISE, 2017. Net Installed Electricity Generation Capacity in Germany [WWW Document]. URL https://www.energy-charts.de/power_inst.htm?year=all&period=annual&type=power_inst (accessed 8.21.17).

Garretson, I.C., Mani, M., Leong, S., Lyons, K.W., Haapala, K.R., 2016a. Terminology to support manufacturing process characterization and assessment for sustainable production. Journal of Cleaner Production 139, 986–1000. https://doi.org/10.1016/j.jclepro.2016.08.103

Garretson, I.C., Mani, M., Leong, S., Lyons, K.W., Haapala, K.R., 2016b. Terminology to support manufacturing process characterization and assessment for sustainable production. Journal of Cleaner Production 139, 986–1000. https://doi.org/10.1016/j.jclepro.2016.08.103

Ghemraoui-Lagord, R., Mathieu, L., Brown, C.A., 2011. Defining Safety Objectives During Product Design, in: ICAD2011. Presented at the Sixth International Conference on Axiomatic Design, Daejeon, South Korea.

Gillespie, L., 2007. Mass Finishing Handbook, 1st ed. Industrial Press, New York, NY.

Groover, M.P., 2012. Fundamentals of Modern Manufacturing: Materials, Processes, and Systems, 5th ed. John Wiley & Sons.

Grzesik, W., 2016. Prediction of the Functional Performance of Machined Components Based on Surface Topography: State of the Art. Journal of Materials Engineering and Performance 25, 4460–4468. https://doi.org/10.1007/s11665-016-2293-z

Gutowski, T., Dahmus, J., Thiriez, A., 2006. Electrical Energy Requirements for Manufacturing Processes, in: 13th CIRP International Conference on Life Cycle Engineering. CIRP International, Leuven, Belgium.

Gutowski, T.G., Branham, M.S., Dahmus, J.B., Jones, A.J., Thiriez, A., Sekulic, D.P., 2009. Thermodynamic Analysis of Resources Used in Manufacturing Processes. Environmental Science & Technology 43, 1584–1590. https://doi.org/10.1021/es8016655

Haapala, K.R., Rivera, J.L., Sutherland, J.W., 2008. Application of Life Cycle Assessment Tools to Sustainable Product Design and Manufacturing. International Journal of Innovative Computing, Information and Control 4, 575–589.

Haapala, K.R., Zhao, F., Camelio, J., Sutherland, J.W., Skerlos, S.J., Dornfeld, D.A., Jawahir, I.S., Clarens, A.F., Rickli, J.L., 2013. A Review of Engineering Research in Sustainable Manufacturing. Journal of Manufacturing Science and Engineering 135, 041013-1-041013–16. https://doi.org/10.1115/1.4024040

Hacksteiner, M., Duer, F., Ayatollahi, I., Bleicher, F., 2017. Automatic Assessment of Machine Tool Energy Efficiency and Productivity. Procedia CIRP 62, 317–322. https://doi.org/10.1016/j.procir.2016.06.034

Hacksteiner, M., Peherstorfer, H., Bleicher, F., 2018. Energy efficiency of state-of-the-art grinding processes. Procedia Manufacturing, 15th Global Conference on Sustainable Manufacturing 21, 717–724. https://doi.org/10.1016/j.promfg.2018.02.176

Hahn, Roberts., 1981. The Influence of Threshold Forces on Size, Roundness and Contour Errors in Precision Grinding. CIRP Annals 30, 251–254. https://doi.org/10.1016/S0007-8506(07)60936-6

Hahn, R.S., 1986. Improving performance with force-adaptive grinding. Manuf. eng 97, 73.

Hahn, R.S., 1964. Controlled-Force Grinding—A New Technique for Precision Internal Grinding. J. Eng. Ind 86, 287–293. https://doi.org/10.1115/1.3670536

Hallstedt, S.I., Thompson, A.W., Lindahl, P., 2013. Key elements for implementing a strategic sustainability perspective in the product innovation process. Journal of Cleaner Production 51, 277–288. https://doi.org/10.1016/j.jclepro.2013.01.043

Hashimoto, F., Chaudhari, R.G., Melkote, S.N., 2016. Characteristics and Performance of Surfaces Created by Various Finishing Methods (Invited Paper). Procedia CIRP 45, 1–6. https://doi.org/10.1016/j.procir.2016.02.052

Hashimoto, F., DeBra, D.B., 1996. Modelling and Optimization of Vibratory Finishing Process. CIRP Annals 45, 303–306. https://doi.org/10.1016/S0007-8506(07)63068-6

Heinzel, C., Kolkwitz, B., 2019. The Impact of fluid supply on energy efficiency and process performance in grinding. CIRP Annals 68, 337–340. https://doi.org/10.1016/j.cirp.2019.03.023

Hodge, B.K., 2010. Alternative Energy Systems and Applications. John Wiley & Sons, Hoboken NJ.

Humphrey, S., Papadopoulos, H., Linke, B., Maiyya, S., Vijayaraghavan, A., Schmitt, R., 2014. Power Measurement for Sustainable High-performance Manufacturing Processes. Procedia CIRP, 6th CIRP International Conference on High Performance Cutting, HPC2014 14, 466–471. https://doi.org/10.1016/j.procir.2014.03.041

Inasaki, I., Karpuschewski, B., Lee, H.-S., 2001. Grinding Chatter – Origin and Suppression. CIRP Annals 50, 515–534. https://doi.org/10.1016/S0007-8506(07)62992-8

ISO, 2015a. ISO 16610-20:2015 Geometrical product specifications (GPS) — Filtration — Part 20: Linear profile filters: Basic concepts [WWW Document]. ISO. URL https://www.iso.org/cms/render/live/en/sites/isoorg/contents/data/standard/06/13/61376.html (accessed 4.19.21).

ISO, 2015b. ISO 16610-61: Geometrical product specification (GPS) – Filtration – Part 61: Linear areal filters: Gaussian filters.

ISO, 2012a. ISO 25178-2: Geometrical Product Specifications (GPS) - Surface Texture: Areal - Part 2: Terms, Definitions and Surface Texture Parameters (No. ISO 25178-2:2012).

ISO, 2012b. ISO 25178-3: Geometrical product specifications (GPS) – Surface texture: Areal – Part 3: Specification operators (No. ISO 25178-3:2012).

ISO, 2011. ISO 16610-21:2011 Geometrical product specifications (GPS) — Filtration — Part 21: Linear profile filters: Gaussian filters [WWW Document]. ISO. URL https://www.iso.org/cms/render/live/en/sites/isoorg/contents/data/standard/05/01/50176.html (accessed 4.19.21).

ISO, 2002. ISO/TR 14062:2002 - Environmental management -- Integrating environmental aspects into product design and development [WWW Document]. ISO. URL http://www.iso.org/iso/catalogue_detail?csnumber=33020 (accessed 5.13.16).

ISO, 1997a. ISO 4287:1997 Geometrical Product Specifications (GPS) — Surface texture: Profile method — Terms, definitions and surface texture parameters [WWW Document]. ISO. URL https://www.iso.org/cms/render/live/en/sites/isoorg/contents/data/standard/01/01/10132.html (accessed 4.19.21).

ISO, 1997b. ISO 4287: Geometrical Product Specifications (GPS) – Surface texture: Profile method – Terms, definitions and surface texture parameters (No. ISO 4287:1997).

ISO, 1996a. ISO 13565-2:1996 Geometrical Product Specifications (GPS) — Surface texture: Profile method; Surfaces having stratified functional properties — Part 2: Height characterization using the linear material ratio curve [WWW Document]. ISO. URL https://www.iso.org/cms/render/live/en/sites/isoorg/contents/data/standard/02/22/22280.html (accessed 4.19.21).

ISO, 1996b. ISO 13565-2: Geometrical Product Specifications (GPS) – Surface texture: Profile method; Surfaces having stratified functional properties – Part 2: Height characterization using the linear material ratio curve (No. ISO 13565-2:1996).

Jensen, A.A., Hoffman, L., Moller, B.T., Schmidt, A., 1997. Life Cycle Assessment (LCA), a guide to approaches, experiences and information sources (No. 6), Environmental Issues Series. European Environmental Agency.

Jiang, X.J., Whitehouse, D.J., 2012. Technological shifts in surface metrology. CIRP Annals 61, 815–836. https://doi.org/10.1016/j.cirp.2012.05.009

Jiménez-González, C., Kim, S., Overcash, M., 2000. Methodology for Developing Gate-to-Gate Life Cycle Inventory Information 5, 153–159. https://doi.org/10.1007/BF02978615

Jiménez-González, C., Overcash, M.R., Curzons, A., 2001. Waste Treatment Modules – A Partial Life Cycle Inventory. J. Chem. Technol. Biotechnol. 76, 707–716. https://doi.org/10.1002/jctb.426

Jørgensen, A., Bocq, A., Nazarkina, L., Hauschild, M., 2007. Methodologies for Social Life Cycle Assessment. The International Journal of Life Cycle Assessment 13, 96–103. https://doi.org/10.1065/lca2007.11.367

Jovane, F., Yoshikawa, H., Alting, L., Boër, C.R., Westkamper, E., Williams, D., Tseng, M., Seliger, G., Paci, A.M., 2008. The Incoming Global Technological and Industrial Revolution Towards Competitive Sustainable Manufacturing. CIRP Annals - Manufacturing Technology 57, 641–659. https://doi.org/10.1016/j.cirp.2008.09.010

Kahraman, C., Kaya, İ., Cebi, S., 2009. A comparative analysis for multiattribute selection among renewable energy alternatives using fuzzy axiomatic design and fuzzy analytic hierarchy process. Energy, 11th Conference on Process Integration, Modelling and Optimisation for Energy Saving and Pollution Reduction 34, 1603–1616. https://doi.org/10.1016/j.energy.2009.07.008

Kellens, K., Dewulf, W., Overcash, M., Hauschild, M.Z., Duflou, J.R., 2012a. Methodology for Systematic Analysis and Improvement of Manufacturing Unit Process Life Cycle Inventory (UPLCI) CO2PE! Initiative (cooperative effort on process emissions in manufacturing). Part 1: Methodology Description. Int. J. Life Cycle Assess. 17, 69–78. https://doi.org/10.1007/s11367-011-0340-4

Kellens, K., Dewulf, W., Overcash, M., Hauschild, M.Z., Duflou, J.R., 2012b. Methodology for Systematic Analysis and Improvement of Manufacturing Unit Process Life Cycle Inventory (UPLCI) CO2PE! Initiative (cooperative effort on process emissions in manufacturing). Part 2: Case Studies. Int. J. Life Cycle Assess. 17, 242–251. https://doi.org/10.1007/s11367-011-0352-0

Kim, S.-J., Suh, N.P., Kim, S.-G., 1991. Design of software systems based on axiomatic design. Robotics and Computer-Integrated Manufacturing 8, 243–255. https://doi.org/10.1016/0736-5845(91)90036-R

King, R.I., Hahn, R.S., 1986. Handbook of Modern Grinding Technology. Springer US.

Klocke, F., Kuchle, A., 2009. Manufacturing processes. 2, Grinding, honing, lapping, RWTH edition. Springer, Berlin.

Ko, H.-W., Bazzoli, P., Nisbett, J.A., Ma, L., Bristow, D., Landers, R.G., Chen, Y., Kapoor, S.G., Ferreira, P.M., 2017. Quasistatic Error Modeling and Model Testing for a 5-Axis Machine. Procedia Manufacturing, 45th SME North American Manufacturing Research Conference, NAMRC 45, LA, USA 10, 443–455. https://doi.org/10.1016/j.promfg.2017.07.023

Krolczyk, G.M., Krolczyk, J.B., Maruda, R.W., Legutko, S., Tomaszewski, M., 2016. Metrological changes in surface morphology of high-strength steels in manufacturing processes. Measurement 88, 176–185. https://doi.org/10.1016/j.measurement.2016.03.055

Kulak, O., Cebi, S., Kahraman, C., 2010. Applications of axiomatic design principles: A literature review. Expert Systems with Applications 37, 6705–6717. https://doi.org/10.1016/j.eswa.2010.03.061

Kummailil, J., Geiger, D.J., Hahn President, R.S., Brown, C.A., 2006. Measurement and Analysis of Threshold Forces in Diamond Roll Dressing. Journal of Manufacturing Processes 8, 101–111. https://doi.org/10.1016/S1526-6125(06)80005-8

Kundrak, J., Gyani, K., Bana, V., 2008. Roughness of ground and hard-turned surfaces on the basis of 3D parameters. The International Journal of Advanced Manufacturing Technology 38, 110–119. https://doi.org/10.1007/s00170-007-1086-9

Kwak, J.-S., Sim, S.-B., Jeong, Y.-D., 2006. An analysis of grinding power and surface roughness in external cylindrical grinding of hardened SCM440 steel using the response surface

method. International Journal of Machine Tools and Manufacture 46, 304–312. https://doi.org/10.1016/j.ijmachtools.2005.05.019
Lachenmaier, M., Dehmer, A., Trauth, D., Mattfeld, P., Klocke, F., 2018. Influence of different input parameters on the contact conditions determing the surface integrity of workpieces in an unguided vibratory finishing process. Procedia CIRP 71, 53–58. https://doi.org/10.1016/j.procir.2018.05.022
Lee, D.G., Suh, N.P., 2006. Axiomatic Design and Fabrication of Composite Structures: Applications in Robots, Machine Tools, and Automobiles, Oxford Series on Advanced Manufacturing. Oxford University Press, New York, NY.
Lei, N., 2018. Exair 3204 Vortex Tube Performance. UC Davis, Davis, CA.
Lewandowska, A., Kurczewski, P., 2010. ISO 14062 in theory and practice—ecodesign procedure. Part 1: structure and theory. Int J Life Cycle Assess 15, 769–776. https://doi.org/10.1007/s11367-010-0228-8
Li, M., Cao, G., Zhang, L., 2018. Study on Life Cycle Inventory Analysis of Folding Carton, in: Proceedings of 2018 9th China Academic Conference on Printing and Packaging. Presented at the Advances in Graphic Communication, Printing, and Packaging, Jinan, China.
Li, W., Winter, M., Kara, S., Herrmann, C., 2012. Eco-efficiency of manufacturing processes: A grinding case. CIRP Annals - Manufacturing Technology 61, 59–62. https://doi.org/10.1016/j.cirp.2012.03.029
Li, W., Zein, A., Kara, S., Herrmann, C., 2011a. An Investigation into Fixed Energy Consumption of Machine Tools, in: Hesselbach, J., Herrmann, C. (Eds.), Glocalized Solutions for Sustainability in Manufacturing. Springer Berlin Heidelberg, Berlin, Heidelberg, pp. 268–273.
Li, W., Zein, A., Kara, S., Herrmann, C., 2011b. An Investigation into Fixed Energy Consumption of Machine Tools, in: Hesselbach, J., Herrmann, C. (Eds.), Glocalized Solutions for Sustainability in Manufacturing. Springer Berlin Heidelberg, Berlin, Heidelberg, pp. 268–273.
Li, X., Li, W., Yang, S., Shi, H., 2018. Experimental investigation into the surface integrity and tribological property of AISI 1045 steel specimen for barrel finishing. Procedia CIRP 71, 47–52. https://doi.org/10.1016/j.procir.2018.05.021
Linke, B., Overcash, M., 2017. Reusable unit process life cycle inventory for manufacturing: grinding. Prod. Eng. Res. Devel. 11, 643–653. https://doi.org/10.1007/s11740-017-0768-x
Linke, B.S., Dornfeld, D.A., 2012. Application of axiomatic design principles to identify more sustainable strategies for grinding. Journal of Manufacturing Systems.
Lipsett, R.A., n.d. Ball Screws and Lead Screws - The Real World Difference.
LLNL, L.L.N.L., DOE, U.D. of E., 2018. Estimated U.S. Energy Consumption in 2017 (No. LLNL-MI-410527).
Lozano, R., 2012. Towards better embedding sustainability into companies' systems: an analysis of voluntary corporate initiatives. Journal of Cleaner Production 25, 14–26. https://doi.org/10.1016/j.jclepro.2011.11.060
Luttropp, C., Lagerstedt, J., 2006. EcoDesign and The Ten Golden Rules: generic advice for merging environmental aspects into product development. Journal of Cleaner Production 14, 1396–1408. https://doi.org/10.1016/j.jclepro.2005.11.022

Mani, M., Madan, J., Lee, J.H., Lyons, K.W., Gupta, S.K., 2014. Sustainability Characterization for Manufacturing Processes. International Journal of Production Research 52, 1–18. https://doi.org/10.1080/00207543.2014.886788

McCoy, G.A., Douglass, J.G., 2014. Premium Efficiency Motor Selection and Application Guide: A Guidebook for Industry. United States Department of Energy.

McHenry, M.E., Laughlin, D.E., 2014. Magnetic Properties of Metals and Alloys, in: Physical Metallurgy. Elsevier, pp. 1881–2008. https://doi.org/10.1016/B978-0-444-53770-6.00019-8

Melvin, M., Lee, K.D., Torkaman, A., Nam, J., Chun, J.-H., Saka, N., Suh, N.P., 2001. CH 8.6 Chemical-Mechanical Planarization (CMP) Machine, in: Axiomatic Design: Advances and Applications. Oxford University Press, New York, NY.

Menghi, R., Papetti, A., Germani, M., Marconi, M., 2019. Energy efficiency of manufacturing systems: A review of energy assessment methods and tools. Journal of Cleaner Production 240, 118276. https://doi.org/10.1016/j.jclepro.2019.118276

Michalski, J., 2009. Surface topography of the cylindrical gear tooth flanks after machining. The International Journal of Advanced Manufacturing Technology 43, 513–528. https://doi.org/10.1007/s00170-008-1737-5

Mihelcic, J.R., Crittenden, J.C., Small, M.J., Shonnard, D.R., Hokanson, D.R., Zhang, Q., Chen, H., Sorby, S.A., James, V.U., Sutherland, J.W., Schnoor, J.L., 2003. Sustainability Science and Engineering: The Emergence of a New Metadiscipline. Environmental Science & Technology 37, 5314–5324. https://doi.org/10.1021/es034605h

Miller, T.J.E., 1989. Brushless Permenant-Magnet and Reluctance Motor Drives, Monographs in Electrical and Electronic Engineering. Oxford University Press.

Möhring, H.-C., Brecher, C., Abele, E., Fleischer, J., Bleicher, F., 2015. Materials in machine tool structures. CIRP Annals - Manufacturing Technology 64, 725–748. https://doi.org/10.1016/j.cirp.2015.05.005

Morrison, J.R., Azhar, M., Lee, T., Suh, H., 2013. Axiomatic Design for eco-design: eAD $^{+}$. Journal of Engineering Design 24, 711–737. https://doi.org/10.1080/09544828.2013.822150

Mueller, K.G., Besant, C.B., 1999. Streamlining life cycle analysis: a method, in: Proceedings First International Symposium on Environmentally Conscious Design and Inverse Manufacturing. Presented at the Proceedings First International Symposium on Environmentally Conscious Design and Inverse Manufacturing, IEEE, Tokyo, Japan, pp. 114–119. https://doi.org/10.1109/ECODIM.1999.747593

Mueller, K.G., Lampérth, M.U., Kimura, F., 2004. Parameterised inventories for life cycle assessment: Systematically relating design parameters to the life cycle inventory. Int J LCA 9, 227. https://doi.org/10.1007/BF02978598

Mullany, B., Shahinian, H., Navare, J., Azimi, F., Fleischhauer, E., Tkacik, P., Keanini, R., 2017. The application of computational fluid dynamics to vibratory finishing processes. CIRP Annals 66, 309–312. https://doi.org/10.1016/j.cirp.2017.04.087

Murray, V.R., Zhao, F., Sutherland, J.W., 2012. Life cycle analysis of grinding: a case study of non-cylindrical computer numerical control grinding via a unit-process life cycle inventory approach. Proceedings of the Institution of Mechanical Engineers, Part B: Journal of Engineering Manufacture 226, 1604–1611. https://doi.org/10.1177/0954405412454102

Nawaz, I., Tiwari, G.N., 2006. Embodied energy analysis of photovoltaic (PV) system based on macro- and micro-level. Energy Policy 34, 3144–3152. https://doi.org/10.1016/j.enpol.2005.06.018

Ness, B., Urbel-Piirsalu, E., Olsson, L., Anderberg, S., 2007. Categorizing Tools for Sustainability Assessment. Ecological Economics 60, 498–508.

Nguyen, T., Zhang, L.C., 2003. An assessment of the applicability of cold air and oil mist in surface grinding. Journal of Materials Processing Technology, Proceedings of the 6th Asia Pacific Conference on materials Processing 140, 224–230. https://doi.org/10.1016/S0924-0136(03)00714-3

Nilsson, J.W., Riedel, S., 2008. Electric Circuits, 8th ed. Pearson, Boston.

Nordelfof, A., Grunditz, E., Tillman, A.-M., Thiringer, T., Alatalo, M., 2016. A Scaleable Life Cycle Inventory of an Electrical Automotive Traction Machine (No. 2016:4). Chalmers University of Technology, Gothenburg, Sweden.

Nordelöf, A., Alatalo, M., Söderman, M.L., 2019a. A scalable life cycle inventory of an automotive power electronic inverter unit—part I: design and composition. Int J Life Cycle Assess 24, 78–92. https://doi.org/10.1007/s11367-018-1503-3

Nordelöf, A., Grunditz, E., Lundmark, S., Tillman, A.-M., Alatalo, M., Thiringer, T., 2019b. Life cycle assessment of permanent magnet electric traction motors. Transportation Research Part D: Transport and Environment 67, 263–274. https://doi.org/10.1016/j.trd.2018.11.004

Nordelöf, A., Grunditz, E., Tillman, A.-M., Thiringer, T., Alatalo, M., 2018. A scalable life cycle inventory of an electrical automotive traction machine—Part I: design and composition. Int J Life Cycle Assess 23, 55–69. https://doi.org/10.1007/s11367-017-1308-9

Norgate, T.E., Jahanshahi, S., Rankin, W.J., 2007. Assessing the environmental impact of metal production processes. Journal of Cleaner Production 15, 838–848. https://doi.org/10.1016/j.jclepro.2006.06.018

NRC, U.N.R.C., 1995. Unit Manufacturing Processes: Issues and Opportunities in Research. National Academy of Sciences, Washington, D.C.

NSK, n.d. Selection Guide to NSK Ball Screws.

Orlova, S., Rassõlkin, A., Kallaste, A., Vaimann, T., Belahcen, A., 2016. Lifecycle Analysis of Different Motors from the Standpoint of Environmental Impact. Latvian Journal of Physics and Technical Sciences 53, 37–46. https://doi.org/10.1515/lpts-2016-0042

Overcash, M., Twomey, J., Kalla, D., 2009. Unit Process Life Cycle Inventory for Product Manufacturing Operations, in: ASME International Manufacturing Science and Engineering Conference. ASME, West Lafayette, IN, pp. 49–55. https://doi.org/10.1115/MSEC2009-84065

Pacala, S., Socolow, R., 2004. Stabilization Wedges: Solving the Climate Problem for the Next 50 Years with Current Technologies. Science 305, 968–972. https://doi.org/10.1126/science.1100103

Pacific Gas & Electric, 2017. Tariffs: Industrial/General Service (E-20) [WWW Document]. URL https://www.pge.com/tariffs/electric.shtml (accessed 8.8.17).

Pappalardo, M., Naddeo, A., 2005. Failure mode analysis using axiomatic design and non-probabilistic information. Journal of Materials Processing Technology, AMPT/AMME05 Part 2 164–165, 1423–1429. https://doi.org/10.1016/j.jmatprotec.2005.02.041

Pawlus, P., Cieslak, T., Mathia, T., 2009. The study of cylinder liner plateau honing process. Journal of Materials Processing Technology 209, 6078–6086. https://doi.org/10.1016/j.jmatprotec.2009.04.025

PG&E, 2010. Peak Day Pricing Guide: Event Days and Energy Management Tools and Tips.
PG&E, 2007. Economics of Power Factor Correction in Large Facilities, >400kW.
Popp, R.S.-H., Liebl, C., Zaeh, M.F., 2017. Evaluation of the Energy Flexible Operation of Machine Tool Components. Procedia CIRP 63, 76–81. https://doi.org/10.1016/j.procir.2017.02.037
Priarone, P.C., 2016. Quality-conscious optimization of energy consumption in a grinding process applying sustainability indicators. Int J Adv Manuf Technol 86, 2107–2117. https://doi.org/10.1007/s00170-015-8310-9
Przyklenk, K., Schlatter, M., 1987. Entgraten von Werkstuecken aus Aluminium. Aluminium-Verlag.
Qi, Q., Li, T., Scott, P.J., Jiang, X., 2015. A Correlational Study of Areal Surface Texture Parameters on Some Typical Machined Surfaces. Procedia CIRP 27, 149–154. https://doi.org/10.1016/j.procir.2015.04.058
Ramani, K., Ramanujan, D., Bernstein, W.Z., Zhao, F., Sutherland, J., Handwerker, C., Choi, J.-K., Kim, H., Thurston, D., 2010a. Integrated Sustainable Life Cycle Design: A Review. J. Mech. Des. 132, 091004–1 to 091004–15. https://doi.org/10.1115/1.4002308
Ramani, K., Ramanujan, D., Bernstein, W.Z., Zhao, F., Sutherland, J., Handwerker, C., Choi, J.-K., Kim, H., Thurston, D., 2010b. Integrated Sustainable Life Cycle Design: A Review. J. Mech. Des. 132, 091004-1-091004–15. https://doi.org/10.1115/1.4002308
Reap, J., Roman, F., Duncan, S., Bras, B., 2008. A Survey of Unresolved Problems in Life Cycle Assessment: Part 1: Goal and Scope and Inventory Analysis. The International Journal of Life Cycle Assessment 13, 290–300. https://doi.org/10.1007/s11367-008-0008-x
Reinhart, G., Reinhardt, S., Graßl, M., 2012. Energieflexible Produktionssysteme: Einführungen zur Bewertung der Energieeffizienz von Produktionssystemen.
Ryan, J., 2019. Questions Regarding Vibrations in Machine Design; DMG Mori Machine Tool Designer.
Saberi, A., Rahimi, A.R., Parsa, H., Ashrafijou, M., Rabiei, F., 2016. Improvement of surface grinding process performance of CK45 soft steel by minimum quantity lubrication (MQL) technique using compressed cold air jet from vortex tube. Journal of Cleaner Production 131, 728–738. https://doi.org/10.1016/j.jclepro.2016.04.104
Sacerdotti, F., Griffiths, B.J., Butler, C., Benati, F., 2000. Surface topography in autobody manufacture—the state of the art. Proceedings of the Institution of Mechanical Engineers, Part B: Journal of Engineering Manufacture 214, 811–820. https://doi.org/10.1243/0954405001517883
Sadeghi, L., Mathieu, L., Nicolas, T., Al-Bassit, L., 2013. Toward Design for Safety Part 1: Functional Reverse Engineering Driven by Axiomatic Design, in: ICAD2013. Presented at the Seventh International Conference on Axiomatic Design, Worchester, MA, USA.
Salonitis, K., 2015. Energy efficiency assessment of grinding strategy. International Journal of Energy Sector Management 9, 20–37. https://doi.org/10.1108/IJESM-04-2013-0009
Schmitz, T., 2020. Modal interactions for spindle, holders, and tools. Procedia Manufacturing, 48th SME North American Manufacturing Research Conference, NAMRC 48 48, 457–465. https://doi.org/10.1016/j.promfg.2020.05.069
Schmitz, T., Smith, S., 2020. Machining Dynamics: Frequency Response to Improved Productivity, 2nd ed. Springer.
SDP-SI, n.d. Ball and ACME Lead Screw Technical Information.

Seibt, M.C., 2019. Analysis and Modeling of Embodied and Peak Energy and Product Surface Quality in Grinding (Bachelor's Thesis). RWTH Aachen University, Aachen Germany.
Shabi, L., Weber, Juliane, Weber, Jürgen, 2017. Analysis of the Energy Consumption of Fluidic Systems in Machine Tools. Procedia CIRP 63, 573–579. https://doi.org/10.1016/j.procir.2017.03.348
Shin, M., Azhar, M., Morrison, J.R., Lee, T., Suh, H.W., 2011. On the Use of Axiomatic Design for Ecodesign, in: Proceedings of ICAD 2011. Presented at the ICAD, Daejeon.
Slocum, A.H., 1992. Precision Machine Design. Society of Manufacturing Engineers, Dearborn, Michigan.
Soong, W.L., 2008. Sizing of Electrical Machines. Power Engineering Briefing Note Series 2.
Stiassnie, E., Shpitalni, M., 2007. Incorporating Lifecycle Considerations in Axiomatic Design. CIRP Annals - Manufacturing Technology 56, 1–4. https://doi.org/10.1016/j.cirp.2007.05.002
Suh, N.P., 2001. Axiomatic Design: Advances and Applications. Oxford University Press, New York, NY.
Suh, N.P., Bell, A.C., Gossard, D.C., 1978. On an Axiomatic Approach to Manufacturing and Manufacturing Systems. J. Eng. Ind 100, 127–130. https://doi.org/10.1115/1.3439399
Suwa, H., Samukawa, T., 2016. A New Framework of Energy-Efficient Manufacturing Systems Based on Energy Load Profiles. Procedia CIRP 41, 313–317. https://doi.org/10.1016/j.procir.2015.10.011
Sy, M., Mascle, C., 2011. Product design analysis based on life cycle features. Journal of Engineering Design 22, 387–406. https://doi.org/10.1080/09544820903409899
Tapoglou, N., Mehnen, J., Butans, J., Morar, N.I., 2016. Online on-board Optimization of Cutting Parameter for Energy Efficient CNC Milling. Procedia CIRP 40, 384–389. https://doi.org/10.1016/j.procir.2016.01.072
Tehel, R., Päßler, T., Mihm, M., 2019. Modeling elastic behavior of forming machine components to reduce tool manufacturing time. Procedia Manufacturing, 6th ICAFT – International Conference on Accuracy in Forming Technology 25th SFU – Saxon Conference on Forming Technology6th AutoMetForm – International Lower Silesia – Saxony Conference on Advanced Metal Forming Processes in the Automotive Industry 27, 177–184. https://doi.org/10.1016/j.promfg.2018.12.062
Thomas, T.R., 2014. Roughness and function. Surface Topography: Metrology and Properties 2, 014001. https://doi.org/10.1088/2051-672X/2/1/014001
Thompson, n.d. Thomson BSA Lead and Ball Screws.
Torrent, M., Martínez, E., Andrada, P., 2012. Life cycle analysis on the design of induction motors. Int J Life Cycle Assess 17, 1–8. https://doi.org/10.1007/s11367-011-0332-4
Trung, P.Q., Khun, N.W., Butler, D.L., 2016. Effects of shot peening pressure, media type and double shot peening on the microstructure, mechanical and tribological properties of low-alloy steel. Surface Topography: Metrology and Properties 4, 045001. https://doi.org/10.1088/2051-672X/4/4/045001
Uhlmann, E., Dethlefs, A., Eulitz, A., 2014. Investigation into a geometry-based model for surface roughness prediction in vibratory finishing processes. The International Journal of Advanced Manufacturing Technology 75, 815–823. https://doi.org/10.1007/s00170-014-6194-8
US EIA, 2021. 2018 Manufacturing Energy Consumption Survey, Consumption Results. US Department of Energy, Washington, DC.

US EIA, 2019. Static Sankey Diagram Full Sector Manufacturing (2014 MECS) [WWW Document]. Energy.gov. URL https://www.energy.gov/eere/amo/static-sankey-diagram-full-sector-manufacturing-2014-mecs (accessed 4.21.21).
USEIA, 2016a. EIA - International Energy Outlook 2016: Chapter 7. Industrial Sector Energy Consumption (No. DOE/EIA-0484(2016)). USEIA, Washington, DC.
USEIA, 2016b. EIA - Annual Energy Outlook 2016 (No. DOE/EIA-0383(2016)). USEIA, Washington, DC.
USEIA, 2016c. EIA - Electric Power Annual. USEIA, Washington, DC.
USGS, 2016. Minneral Commodity Summaries: Bauxite and Alumina.
Valivullah, L., Mani, M., Lyons, K.W., Gupta, S.K., 2014. Manufacturing Process Information Models for Sustainable Manufactring, in: ASME 2014 International Manufacturing Science and Engineering Conference Collocated with the JSME 2014 International Conference on Materials and Processing and the 42nd North American Manufacturing Research Conference. ASME, Detroit, Michigan.
Vallet, F., Eynard, B., Millet, D., Mahut, S.G., Tyl, B., Bertoluci, G., 2013. Using eco-design tools: An overview of experts' practices. Design Studies 34, 345–377. https://doi.org/10.1016/j.destud.2012.10.001
van der Voet, E., Salminen, R., Eckelman, M., Norgate, T., Mudd, G., Hisschier, R., de Koning, A., 2013. Environmental risks and challenges of anthropogenic metals flows and cycles. United Nations Environmental Programs.
Vazquez, S., Lukic, S.M., Galvan, E., Franquelo, L.G., Carrasco, J.M., 2010. Energy Storage Systems for Transport and Grid Applications. IEEE Transactions on Industrial Electronics 57, 3881–3895. https://doi.org/10.1109/TIE.2010.2076414
Veltman, A., Pulle, D.W.J., de Doncker, R.W., 2016. Fundamentals of Electrical Drives, 2ed ed. Springer.
Vibra Finish Company, 2018. Vibratory Tumbling Media [WWW Document]. URL http://vibrafinish.com/vibratory-tumbling-media/ (accessed 10.1.18).
Voet, H., Garretson, I.C., Falk, B., Schmitt, R.H., Linke, B.S., 2018. Peak Power Load and Energy Costs Using the Example of the Startup and Idling of a Grinding Machine. Procedia CIRP 69, 324–329. https://doi.org/10.1016/j.procir.2017.11.044
Wallace, D.R., Suh, N.P., 1993. Information-Based Design for Environmental Problem Solving. CIRP Annals-Manufacturing Technology 42, 175–180.
WEG, 2015. WEG Online Motor Catalogue Data.
Wegener, K., Bleicher, F., Krajnik, P., Hoffmeister, H.-W., Brecher, C., 2017. Recent developments in grinding machines. CIRP Annals 66, 779–802. https://doi.org/10.1016/j.cirp.2017.05.006
Whitehouse, D., 2002. Surfaces and Their Measurement, 1st ed. Hermes Penton Ltd, London, England.
Winter, M., Li, W., Kara, S., Herrmann, C., 2014. Determining optimal process parameters to increase the eco-efficiency of grinding processes. Journal of Cleaner Production 66, 644–654. https://doi.org/10.1016/j.jclepro.2013.10.031
Winter, M., Thiede, S., Herrmann, C., 2015. Influence of the cutting fluid on process energy demand and surface roughness in grinding—a technological, environmental and economic examination. Int J Adv Manuf Technol 77, 2005–2017. https://doi.org/10.1007/s00170-014-6557-1
Yaskawa, 2020. SIGMA-7 AC Servo Drives and Motors Technical Supplement.

Yoon, H.-S., Kim, E.-S., Kim, M.-S., Lee, J.-Y., Lee, G.-B., Ahn, S.-H., 2015. Towards greener machine tools – A review on energy saving strategies and technologies. Renewable and Sustainable Energy Reviews 48, 870–891. https://doi.org/10.1016/j.rser.2015.03.100

Zein, A., 2012. Transition Towards Energy Efficient Machine Tools, Sustainable Production, Life Cycle Engineering and Management. Springer Berlin Heidelberg, Berlin, Heidelberg.

Zein, A., Li, W., Herrmann, C., Kara, S., 2011. Energy Efficiency Measures for the Design and Operation of Machine Tools: An Axiomatic Approach, in: Hesselbach, J., Herrmann, C. (Eds.), Glocalized Solutions for Sustainability in Manufacturing. Springer Berlin Heidelberg, pp. 274–279. https://doi.org/10.1007/978-3-642-19692-8_48

Zhou, L., Li, Jianfeng, Li, F., Meng, Q., Li, Jing, Xu, X., 2016. Energy consumption model and energy efficiency of machine tools: a comprehensive literature review. Journal of Cleaner Production 112, 3721–3734. https://doi.org/10.1016/j.jclepro.2015.05.093

Appendix A: Structural Analysis of a Machine Tool Stand and an Energy Analysis of Pump Elimination.

A.1 Abstract

Refurbishing a machine tool can come with uncertainty, the following paper describes several simulations that were undertaken to help realize design requirements. The first requirement was to raise the machine and provide a space underneath for a coolant tank, thus a stand needed to be designed that would both withstand the static load of the machine and minimize vibrational excitation caused during grinding experiments. The second requirement was to validate the tolerances of the machining process and minimize any deflection that would occur during grinding; a dynamic analysis was carried out to do so. Finite element methods (FEM) software was used to perform the simulations. The simulations described here in thus include, a static structural analysis, a modal analysis, and a dynamic structural analysis. These simulations were performed as worst-case scenarios and are not necessarily indicative of regular use. Results indicate that the stand as designed will not transmit any significant harmonic vibrations. Additionally, the results indicate minimal grinding head deflection incurred during grinding from the original design of the machine.

A.2 Nomenclature

F	Force [N]
σ	Normal stress [MPa]
τ	Shear stress [MPa]
t	Time [s]
σ_V	Von Mises stress [MPa]
σ_{xx}	Normal stress in x-direction [MPa]
σ_{yy}	Normal stress in y-direction [MPa]
σ_{zz}	Normal stress in z-direction [MPa]
τ_{xy}	Shear stress from y-directional force on a surface perpendicular to x-axis [MPa]
τ_{yz}	Shear stress from z-directional force on a surface perpendicular to y-axis [MPa]
τ_{xz}	Shear stress from z-directional force on a surface perpendicular to x-axis [MPa]

A.3 Introduction

Machine tool structural design is a combination of static analyses (Ko et al., 2017; Tehel et al., 2019), dynamic and harmonic analyses (Schmitz, 2020) , and thermal analyses (Bräunig et al., 2019). These analyses are represented in literature, and usually need to be carried out together to best represent a machine tool. Altintas et al. (2005) identified that finite element analyses (FEA) is powerful tool that can be utilized to enhance the performance of machine tools while reducing design time. This manuscript investigates the design of a grinding machine tool using Finite Element Analysis (FEA).

The Hahn grinding machine, designed and built by Robert Hahn (King and Hahn, 1986) as a laboratory prototype machine to investigate force controlled grinding and dressing (Hahn, 1964, 1981, 1986; Kummailil et al., 2006). The machine is now used within the Manufacturing and Sustainable Technologies Research lab at UC Davis to perform grinding research on sample coupons and on cylindrical workpieces with external and internal grinding processes; see Figure A.1. It can be equipped with up to two grinding spindles and has a workpiece and dressing spindle. The grinding spindles are mounted on the Z-axis, enabling the grinding wheel to move vertically and spin. The workpiece and dressing spindle is mounted on the X-axis and enables cylindrical workpieces to move horizontally and spin. The machine has no additional axes.

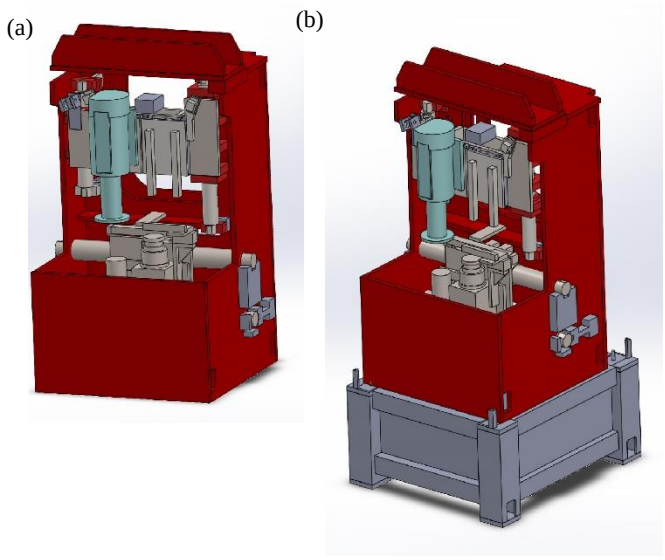

Figure A.1: (a) Hahn grinder machine; (b) Hahn grinder machine on stand; the machine is 0.84 by 0.93 by 1.74 meters; has a 3.73 kW (5 hp) external grinding spindle with 17.8 cm wheels, a 7.5 kW internal grinding spindle (not pictured) with 5.9 cm wheels, and can grind cylindrical workpieces up to 12.7 cm diameter that sit on a belt driven spindle attached with a 4 to 6 gearing to a 2500 rpm 4.8 Nm motor.

The simulations described herein are used to incorporate new features and to validate the accuracy and tolerances of the machine tool as the machine is being refurbished. The first new feature is a modern coolant filtration system.

Section A.4 of this paper describes the design of a stand used to raise the Hahn Grinder to place a coolant tank below the machine. By placing the coolant tank below the machine, gravity can be utilized to move the coolant and eliminate the need for one coolant pump in the machine, and in turn reduce the energy requirements of the grinding machine.

Section A.5 of this paper describes an energy analysis of manufacturing the stand in lieu of a coolant pump motor. This analysis will demonstrate the tradeoff comparison that would need to be made for eliminating a coolant pump and will provide the breakeven time for energy

consumption of the pump vs manufacturing the stand. Finally, Section A.6 discusses the conclusion of the paper and next steps.

A.4 Hahn Grinder Stand Analysis

The section will discuss the simulation and results for the grinding machine tool stand. To verify that the stand will not buckle under the weight of the grinding machine, first a structural analysis is performed. Then to verify that the machine tool will not incur chatter-inducing vibrations, a harmonic vibrational analysis is performed. Finite element methods (FEM) software *Ansys Academic Research Mechanical, Release 19.2* and *Release 20* (ANSYS Inc., n.d.) was used to perform the simulations described herein. As identified by Inasaki et al. (Inasaki et al., 2001) the method utilized here in followed the steps 1) Machine Design, 2) Analysis Method, 3) Analysis Result, 4) Design Evaluation, and 5) Design Improvement.

A.4.1 Static Structural Analysis

Structural steel is the material for Hahn Grinder Stand. The structural steel alloy designation by Ansys represents any steel alloy that would be categorized as structural. For the purposes in this paper, the Ansys alloy properties are close to those of ASTM A36; other alloys from other standards, e.g. JIS, CSA, CEN, ISO, etc. could also apply.

After selecting the material for the model, the contact surfaces were selected with *bonding method*. The bonding method is a good assumption to reflect that the components will be welded together; the ANSYS Mechanical User Manual stated that bonded method prevents any sliding or detachment between two contacting surfaces (ANSYS Inc., 2020a). In this way, a linear analysis

is performed with higher efficiency and low cost of computational power as compared to other joining methods, e.g., a frictional method. The general mesh size of this entire stand model was set to 19 mm (0.75 in), and fine mesh size were set to 6.35 mm (0.25 in) at the high-stress concentration regions as shown in Figure A.1.

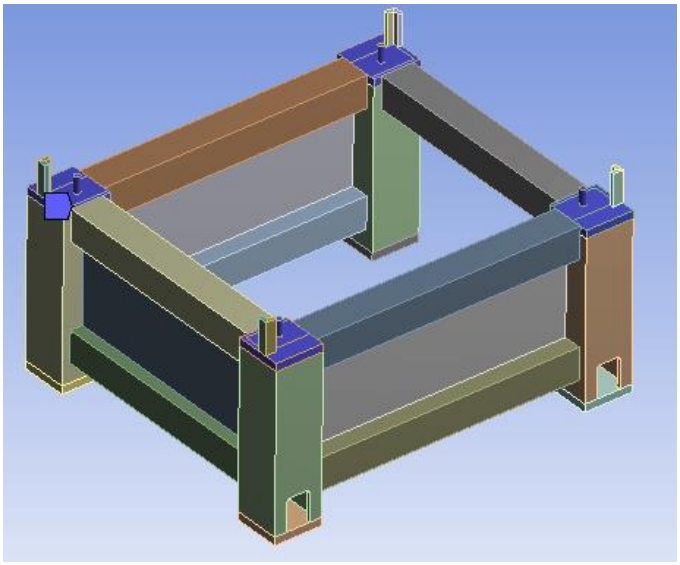

Figure A.2: The stand used for the Hahn Grinder; fine mesh size at critical region colored in blue.

To validate simulation results, the mesh was investigated. The mesh is hex dominant with quad/tri node points applied on each mesh surface. In total, the entire stand has 225,464 nodes and 39,955 elements. The average skewness value is 0.28207 with standard deviation of 0.24038. Figure A.3 shows the element skewness distribution. Based on the cell quality table provided in ANSYS 2020 R2 Meshing Users Guide, the majority of the meshing cells, about 90 percent, are located in the excellent range (0-0.25) and good range (0.25-0.5; and about 10 percent some in the fair range (0.5-0.75) and other ranges (ANSYS Inc., 2020b).

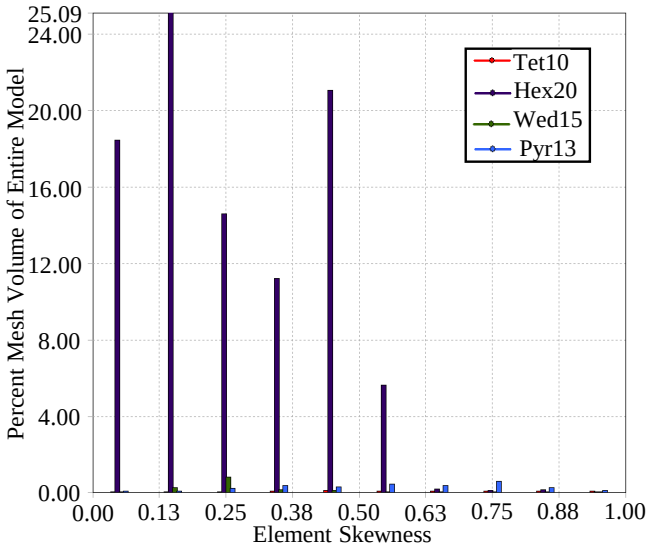

Figure A.3: Skewness distributions among the meshes

The external load is the weight of the Hahn grinder machine and is applied to the top surface at each corner of the stand; identified as the remote force in Figure A.4. As shown in Figure A.4, all the contact surfaces with the machine are colored in red, and the arrow indicates the center of mass of the machine.

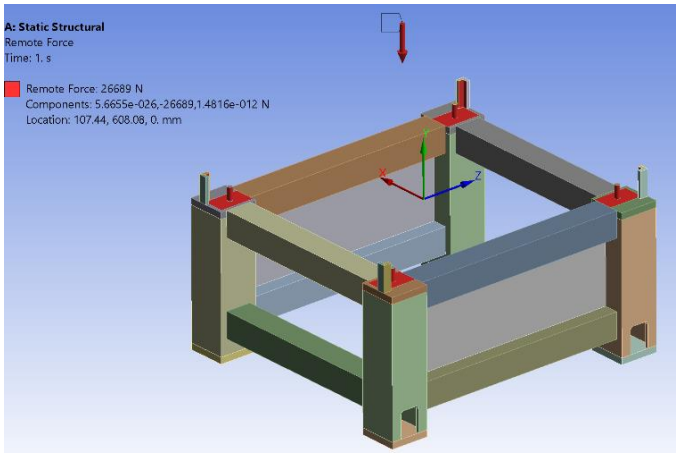

Figure A.4: Remote force setup; this is the mass of the grinding machine and is applied at the center of mass, it is offset from the load surfaces.

The weight of Hahn grinder is 26.7 kN (6000 lbf) in the direction of gravitational force (Y direction in all figures). The fixed support is applied to the bottom surfaces at the same corners as shown in Figure A.5 (a) and Figure A.5 (b). Figure A.5 (b) shows a closer view of the bottom surface, displaying the mounting holes that will mounting the stand to the ground; these holes are selected as the fixed support of this analysis.

The Von Mises stress criterion is used to compute the results of the simulation, and is shown in Eq. (A.1). From the simulation, the maximum deformation is reported to be 0.01 mm (0.00041 in) as shown in Figure A.6. In addition, the maximum stress in the frame is 8.5 MPa (1232.8 psi), and using the yield strength of 250 MPa (36,259 psi), a safety factor of 29.41 is computed using Eq. (A.2).

$$\sigma_V = \sqrt{\frac{1}{2}\left[(\sigma_{xx}-\sigma_{yy})^2(\sigma_{yy}-\sigma_{zz})^2(\sigma_{zz}-\sigma_{xx})^2\right] + 3\left(\tau_{xy}^2+\tau_{yz}^2+\tau_{xz}^2\right)} \quad \text{(A.1)}$$

$$SafetyFactor = \frac{YieldStrength}{MaximumStress} \quad \text{(A.2)}$$

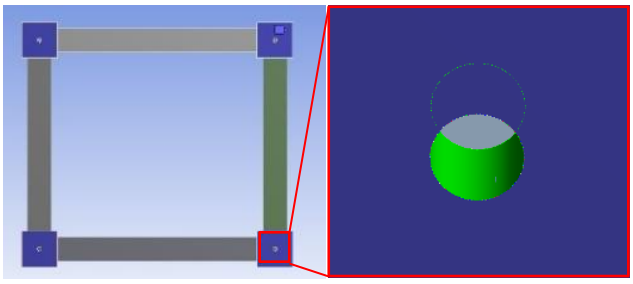

Figure A.5: (a). Fixed support at four corners bottom surface. (b). Fixed support at bolt holes in each bottom plate. The green color indicates the designated attachment point.

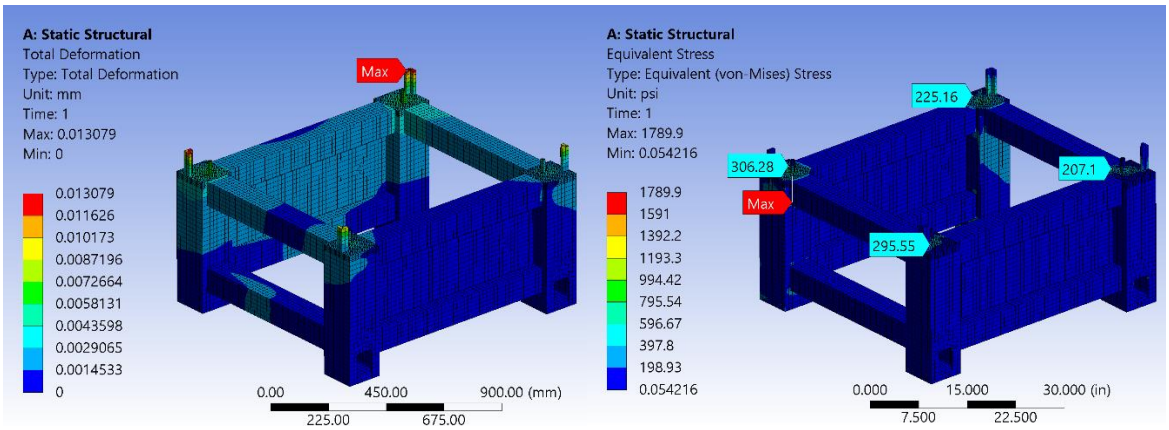

Figure A.6: (left) Deformation distribution on the stand [mm]; (right) Stress distribution at critical regions of the stand [psi].

In Figure A.6, larger stress values can be seen towards the rear of the stand. The grinding machine's center of mass is located towards the rear, and thus places a larger load on the rear stand supports. But of more significance is that a majority of the load is transmitted though the vertical columns of the stand.

A.4.2 Modal Analysis

The stand and grinding machine act as a harmonic oscillator, where the stand is the weight at the end of a flexible beam. Having a higher mass and softer beam would be more prone to harmonic vibrations, thus the stand is investigated to validate that it is stiff enough for the mass of the grinding machine and the vibrations are not excessive. In the modal analysis, first five modes of natural frequency were evaluated, see Figure A.7.

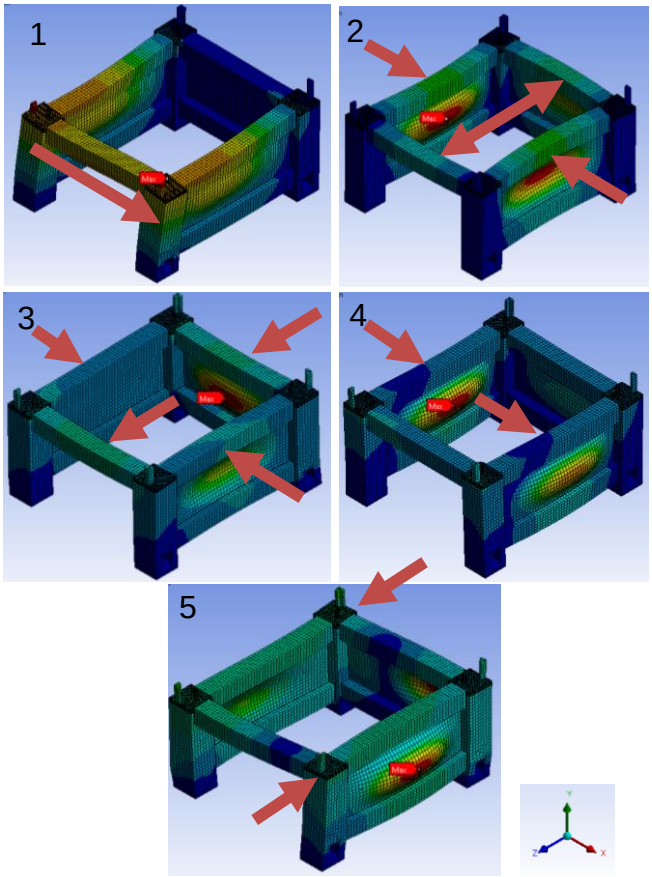

Figure A.7: First five natural frequency modes, with frequencies listed in Table A.2; arrows indicate harmonic oscillation directions.

Based on the interview with a senior mechanical engineer from a machine tool company, first five modes of natural frequency need to be above 50 Hz for the safety purpose (Ryan, 2019). Our goal was increased to exceed 60 Hz to account for the 3600 RPM grinding spindle and the 60 Hz of the US power grid. The machine additionally has 90,000 RPM spindles used for very small internal cylindrical grinding and should produce much less excitation.

Following the method described by Slocum (1992) to avoid a specific fundamental frequency, we want to avoid a combination of two superimposed frequencies. This method calculates the two frequencies to avoid using the harmonic and the fundamental frequencies. The calculation is

described in equations (A.3) and (A.4) (from (Slocum, 1992)); where f_{source} is the complementary frequency, N is the harmonic, and ω_n is the fundamental frequency.

$$f_{source} \neq \left(\frac{2}{N-1}\right)\omega_n \tag{A.3}$$

$$f_{source} \neq \left(\frac{2}{N+1}\right)\omega_n \tag{A.4}$$

Table A.1: Complementary frequencies to avoid the fundamental frequencies of 50 hz and 60 hz.

Fundamental Frequency Harmonic	60 hz		50 hz	
2	40.00	120.00	33.33	100.00
3	30.00	60.00	25.00	50.00
4	24.00	40.00	20.00	33.33
5	20.00	30.00	16.67	25.00
6	17.14	24.00	14.29	20.00
7	15.00	20.00	12.50	16.67
8	13.33	17.14	11.11	14.29
9	12.00	15.00	10.00	12.50
10	10.91	13.33	9.09	11.11

The fixed supports were set to the same location as the static structural analysis. As the result shown in Table A.2, all the five modes had natural frequency passed over 50 Hz with the minimum of 251.02 Hz, which provides a safety factor of 5.02. Figure A.7 are the deformation at each mode. Additionally, note that the first five modes in Table A.2 are much greater than the complementary harmonics in Table A.1. With the knowledge of the nodes here the operator can fine tune the machine to operate to avoid these excitation frequencies.

Table A.2: First five natural frequencies

Mode	Frequency [Hz]
1	251.02
2	334.28
3	378.25
4	385.13
5	449.67

A.4.3 Harmonic Analysis

By implementing the result of modal analysis into the harmonic response analysis, the harmonic response analysis analyzed the vibrational frequency of the stand due to a response force, which in this case is the grinding force. Even though from the modal analysis, the top five natural frequency modes are above 60 Hz. An initial harmonic analysis was run from 0 Hz to 251 Hz, there were no harmonic peaks found in the structure which indicates that range would be a safe operating condition. There is still necessity to monitor the stand's performance due to the harmonic grinding force that exerted in z-direction as shown in Figure A.8 with the frequency of changing direction from 250 Hz to 517 Hz which is shown in Table A.3. In the analysis, we visualize the stress distribution within the frequency range and observed the possible failure due to the excessive stress values from the grinding process.

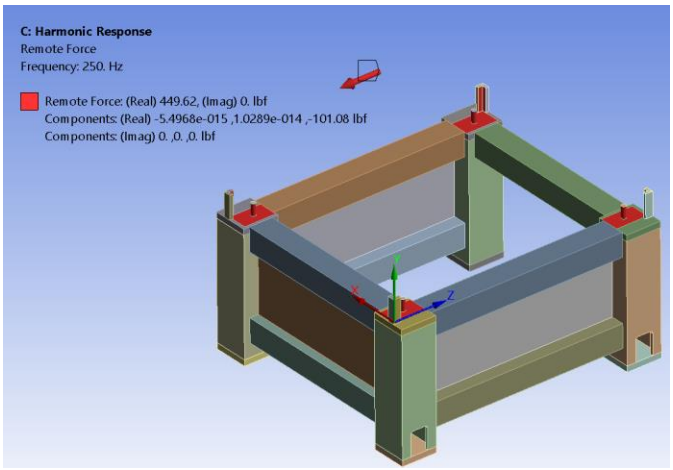

Figure A.8: Response force's location and direction

Table A.3: Boundary Conditions Setup

Frequency Spacing	Linear
Range Minimum	250 Hz
Range Maximum	517 Hz
Solution Intervals	267

The results are shown in Figure A.9, Figure A.10, and Figure A.11 with the normal stress in x-direction, y-direction, and z-direction. Some of the peak points shown in the figures have the frequency that are the same as the natural frequency. The figures illustrate the relationship among the frequency, the normal stress, and force directions. Each peak shown in the figures represents a high normal stress either in the positive or negative direction of the three axes (x, y, and z), and the red force arrow shown in Figure A.9 is the reference of the phase angle in the figures. Physical experiments should be performed in the future to validate the computational analysis result; and would correlate grinding wheel speed, wheel dimensions, and resulting frequencies. The experiment would be carried out using an accelerometer or acoustic emissions sensor to record the acceleration or acoustic emissions during the grinding process; that data could then be correlated with the measuring time to put experimental results in terms of frequency. Based on the comparison result, a specified range of grinding speeds can be determined, which is very helpful for the future users to use this machine.

In Figure A.9, it can be seen that frequencies 330, 390, 450, and 475 Hz are frequencies that would align with the natural frequency and cause high stresses to be induced in the machine tool. In both Figure A.9 and Figure A.11 the 440-frequency value appears to be a state to stability, but all three directions have to be accounted for in unison; and Figure A.10 shows that the 440-frequency is near a point of instability and care would have to be taken to validate that is stable or not using the experimentation described above. All three figures indicate that values below 320 Hz would see lower excitation amplitudes. The phase angle at a positive 180 degrees would cause the stress in the positive z direction, and when at 0 degrees would be negative z direction; the same applies to following figures.

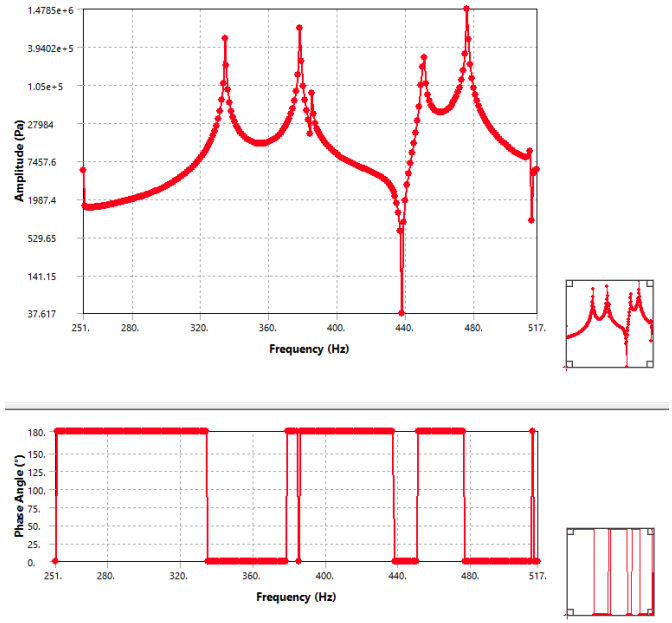

Figure A.9: Normal Stress in x-direction within the frequency from 251 Hz to 517 Hz

Identified by Möring et al. (2015) possible future work would be to investigate filling the steel tube frame legs with sand, foam, concrete or another material to create a composite structure for the potential to enhance the passive vibration damping and increase the modal frequencies; this would require additional simulations. Identified by Altintas and Weck (2004), piezo-actuators could be used for active damping. Additionally, a frequency response function can be generated from data, following the methods in Schmitz and Smith (2020).

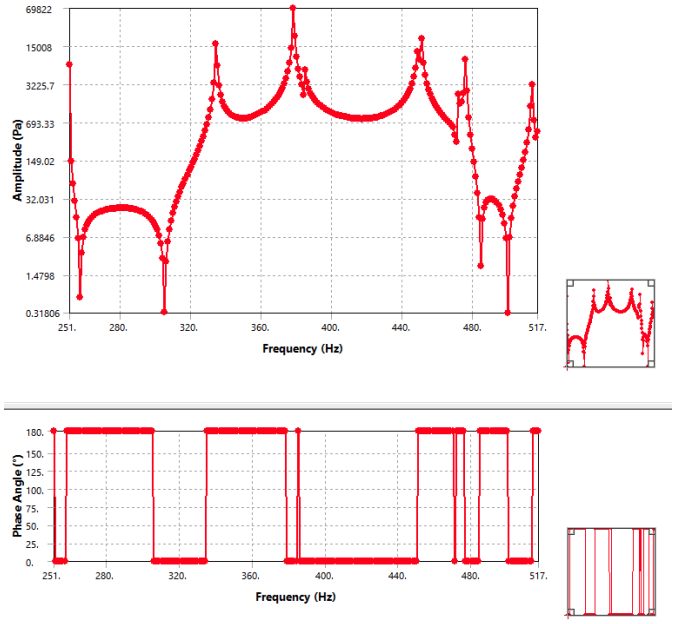

Figure A.10: Normal Stress in y-direction within the frequency from 251 Hz to 517 Hz

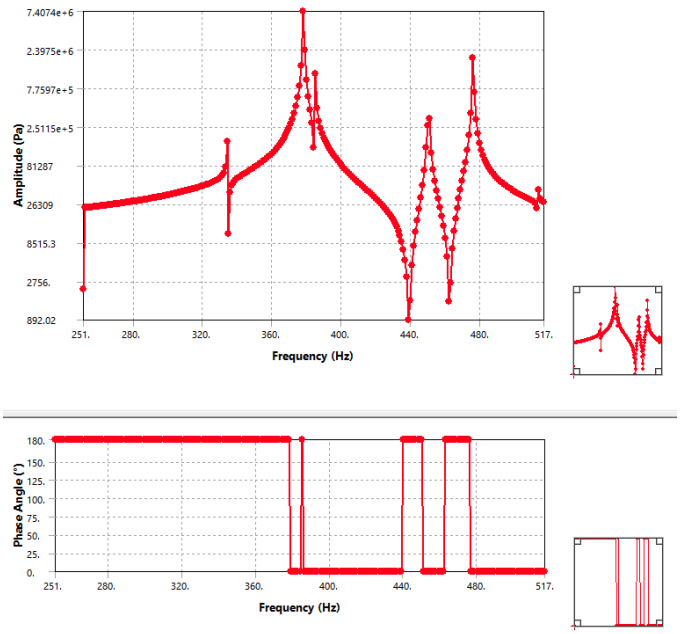

Figure A.11: Normal Stress in z-direction within the frequency from 251 Hz to 517 Hz.

A.5 Energy Analysis of the pump motor

To determine the trade-off in lifecycle energy consumption of a pump motor and a stand, the following theoretical lifecycle energy estimation is undertaken. This LCA estimates energy consumption to produce the materials to manufacture an electric motor. Most of the equations described herein are applicable to 3 phase induction motors and should be assumed unless otherwise noted. Additionally, this section investigates fractional horsepower motors to improve model fitting for these smaller motors, similar steps could be taken for larger motors. The section includes several methods for estimating motor mass, given its dimensions, power, or torque. The section then describes an energy analysis for replacing a pump motor with the stand described in Section A.5.6.

A.5.1 Theoretical Energy Consumption of Motors

The goal in this first step is to estimate the motor mass given a known motor power or torque or from or from the motor volume. The reasoning here is not to provide highly detailed calculations for motor sizing, but rather rule of thumb method for individuals that are not electric motor designers.

A prescriptive sizing method exists, which related motor torque to volume and magnetic shear stress and has been presented by several authors, (Miller, 1989) (p.20-32), (Soong, 2008), and (Veltman et al., 2016) (p. 21-23). Following (Veltman et al., 2016), if r is the radius and *l* is the length of a rotor that holds *n* wires *d* thick, *F* is the resultant force on the rotor, then the torque T_c output by the motor can be seen in Equation (A.5).

$$T_c = rF \approx kBj\pi r^2 l \quad \text{(A.5)}$$

Where the rotor volume $V_r = \pi r^2 l$, k is a constant equal to *2d* (in a simplified example), *B* is the magnetic flux density, and $j = \frac{i}{A}$ is the current density, *i* the current, and *A* the wire cross section area. Magnetic flux density *B* is limited to less than 2.0 T in silicon steel due to a change in reulctance which causes magnetic flux saturation. Current density *j* is limited to less than 10 A/mm^2 due to thermal limtations. The rotor volume can be estimated using this relationship, but unless an understanding of general motor specifications this might proove challenging. Another method does provide an option for estimating motor volume using Equation (A.6) from (Miller, 1989) by calculating the rotor volume using the torque to rotor volume (*TRV*); the TRV is typically 1.4-4 kNm/m^3 for fractional TEFT motors, 15-30 kNm/m^3 for integral TEFC motors, and 20-45 kNm/m^3 for high-performance industrial servos.

$$TRV = \frac{T}{V_r} \tag{A.6}$$

The overall size of an electric motor is directly related to stator volume V_s, which is proportional to rotor volume, as seen in Equation (A.7), where *srs* is a constant in the order of 0.6 (Veltman et al., 2016).

$$V_s \approx \frac{V_r}{srs^2} \tag{A.7}$$

This method described does provide an estimate of the motor volume fairly close to real values (Veltman et al., 2016), but the challenge encountered is a lack of understanding of selecting the correct values (*B, j, TRV,* shear stress, etc.) for the previous equations.

A.5.2 Literature of Fitted Motor Energy Equations

An alternative method is to estimate motor mass from the torque or power using manufacturer data. Motor mass was estimated from motor power by (Mueller and Besant, 1999) in Equation (A.8) and motor mass was estimated from motor torque by (Mueller et al., 2004) in Equation (A.9).

$$M = 0.065 \cdot 0.8^{P} \tag{A.8}$$

$$M = 0.659 + 1.792 \cdot 0.8388^{T} \tag{A.9}$$

The equations from (Mueller and Besant, 1999) and (Mueller et al., 2004) provide estimations of motor mass for four pole induction motors; but more accurate estimates can be made by performing the fits ourselves. Using data from (Ferreira et al., 2016), provided from WEG (WEG, 2015), seen in Figure A.12, Equations (A.10) and (A.11) are fitted from the data below for general purpose 3 phase induction motors. Utilizing a CAD model or disassembling a motor would be more accurate, but this is undertaken assuming that information is not available.

$$M = 13.98 \cdot 0.87^{P} \quad R^2 = 0.98 \tag{A.10}$$

$$T = 6.23P + 1.29 \quad R^2 = 0.99 \tag{A.11}$$

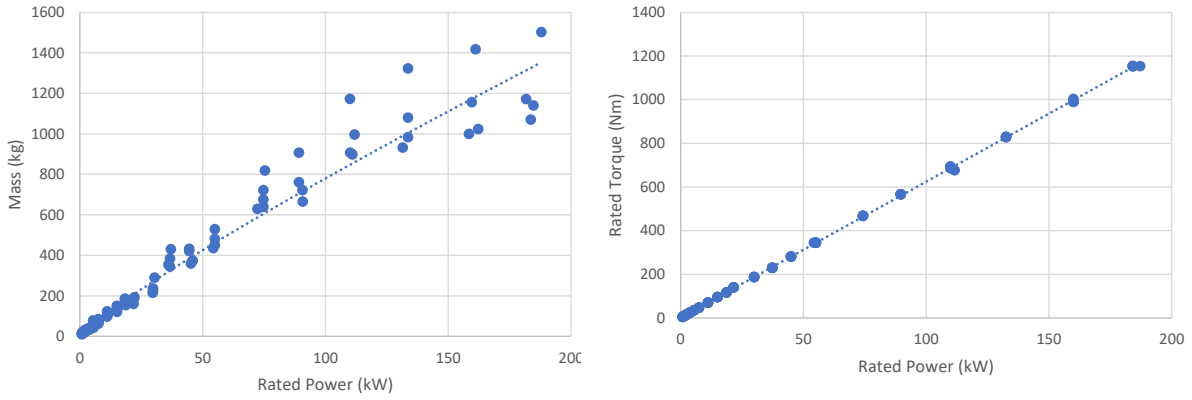

Figure A.12: Motor mass and motor torque from rated power, data from (Ferreira et al., 2016), and (WEG, 2015)

A six kilowatt motor can then be estimated to weight 68.39 and 68.83 using both (Mueller and Besant, 1999) and (Ferreira et al., 2016) respectively. A question arises, if a LCA practitioner has access to the motor, why not look up motor specification with the manufacturer? The reasons are threefold, first some motors are older and exact specifications are not known, or second manufacturers no longer provide information on older models, or third to reduce time spent researching individual components while performing an LCA.

A.5.3 Mass and Power of Fractional HP Jet Pump Motors

Fractional HP jet pump motor masses M were also fitted to power P and length C for the pump comparison to be seen later in the chapter. While the equations from (Mueller and Besant, 1999), (Mueller et al., 2004) or (Ferreira et al., 2016) could be used for this application, since jet pump motors are AC induction machines, a more accurate estimation of mass is made by focusing on the pump motor data from (ABB, 2018a). This data included motor length, but was missing motor volume, thus fitting an equation to mass, power, and motor volume is an opportunity for future work. Figure A.13 shows a visual comparison of the fits of Equations (A.12), (A.13), and (A.14).

$$M = 16.61 \cdot P^{0.388} \quad R^2 = 0.78 \tag{A.12}$$

$$M = 0.056 \cdot P^{0.184} \cdot C^{2.194} \quad R^2 = 0.88 \tag{A.13}$$

$$M = 2.838P + 2.819C - 24.24 \quad R^2 = 0.85 \tag{A.14}$$

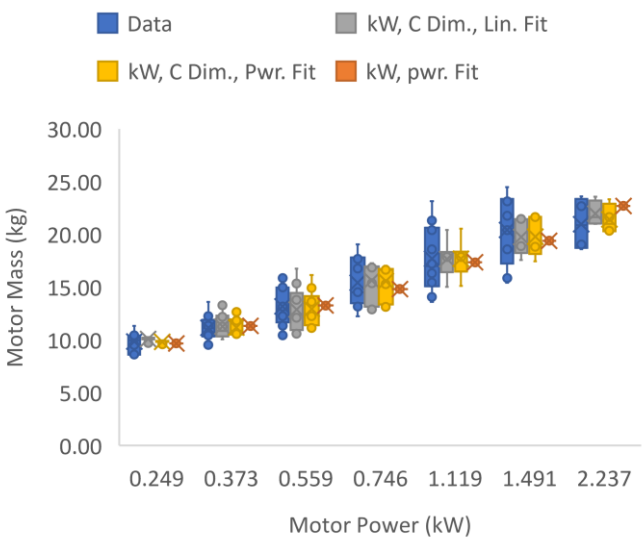

Figure A.13: Fraction HP jet pump motors, data and fitted equations. Data from (ABB, 2018a). Where orange is Eq. (A.12), yellow is Eq. (A.13), and grey is Eq. (A.14).

Figure A.14 provides a map of the relationship between power, length, and motor mass using Equation (A.13).This type of graph can simplify the investigation of motor mass by an LCA practitioner allowing the use of the graph in place of the equation.

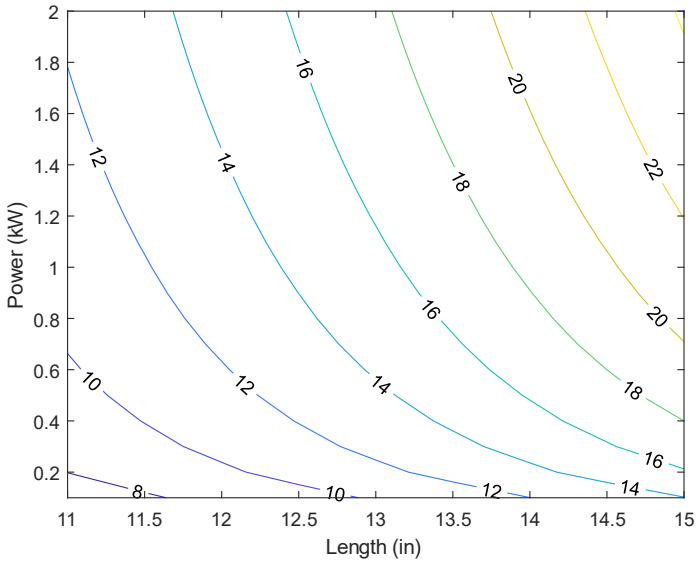

Figure A.14: Mass (kg) of a pump motor given power and length, plotted using Eq. (A.13).

A.5.4 Motor Losses

The McCory and Douglass provides a very straight forward method for motor selection (McCoy and Douglass, 2014). They highlight a key misconception of motor sizing – that downsizing an under-loaded a motor will result in efficiency improvements by selecting a motor that will operate closer to one hundred percent load. Efficiency gains are actually made by replacing an older standard class motor with a more efficient (and modern) premium class motor. This can be seen in Figure A.15[

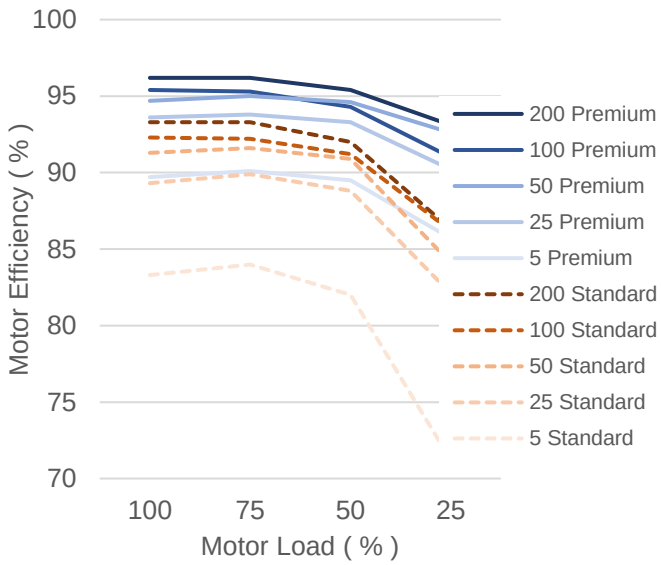

Figure A.15: Motor efficiency (%), load (%), and power (kW) for standard and premium IM motors; data from (McCoy and Douglass, 2014)

A.5.5 Energy to Manufacture a Motor

To estimate the embedded energy within an electric motor, the constituent materials must be known because each different material carries a different embedded energy. If the motor that is being assessed is not available for disassembly, then we must estimate its constituent materials. To do so, a literature review of papers that identify constituent materials was performed and the data extracted can be seen in Table A.4. Of note, the data from each paper has become more detailed in time. The table displays material percentages that sum to 100 for different studies, and it includes several motor types and sizes. Most are induction motors (IM), and additionally synchronous reluctance motors (Syn RM), permanent magnet synchronous reluctance motors (PM Syn RM), permanent magnet synchronous motors (PMSM) are included.

Table A.4: Electric Motor Constituent Material Mass Percentages, data from (Andrada et al., 2012; Ferreira et al., 2011; Mueller et al., 2004)

Source	Mueller 2004	Ferreira 2011	Ferreira 2011	Andrada 2012	Andrada 2012
Motor Type	IM	IM	IM	Eff3 IM	Eff1/IE2 IM
Motor Power	0.1-1000 kW	1.1 kW	11 kW	1.5 kW	1.5 kW
Material	(%)	(%)	(%)	(%)	(%)
Electrical Steel	40%	39.2%	42.6%	40%	42%
Other Steel	10%	10.9%	11.2%	11%	8%
Cast Iron	32%	18.1%	15.4%		
Aluminum		12.3%	10.6%	26%	26%
Copper	9%	9.0%	7.6%	9%	10%
Insulation Material	9%	0.4%	0.2%	0%	0%
Permanent Magnets					
Impregnation Resin		2.2%	1.2%	2%	2%
Paint		0.7%	0.6%	0%	0%
Packing Material		7.3%	10.6%	8%	7%
Plastic				2%	2%
Electronics				1%	1%
Total Percent	100.0%	100.0%	100.0%	100.0%	100.0%

To then determine the energy requirements of a motor, the energy requirements for producing each of the materials shown in Table A.4 are then shown in Table A.5. Of note, the minute difference between electrical steel and other steel. Electrical steel typically is an alloy with low carbon percent and 2 - 4.5 percent silicon; and embrittlement usually occurs at 2 percent silicon added (McHenry and Laughlin, 2014) (p. 1931). The silicon addition improves performance of the motors both reducing losses and improving magnetic softness. Thus, electrical steel was estimated assuming embedded energy of iron/steel at 25 MJ/kg (van der Voet et al., 2013) and metallurgical grade silicon at 72 MJ/kg (Nawaz and Tiwari, 2006). Thus 2 % Si steel would be 26 MJ/kg, 4.5 % Si steel would be 27 MJ/kg, and Sendust (85% Fe, 9% Si, 6% Al) would be 40 MJ/kg.

Table A.5: Energy Requirements for Constituent Materials Used to Evaluate the Example Electric Motor; data from (Engelbeen, n.d.; M. Li et al., 2018; McHenry and Laughlin, 2014; Nawaz and Tiwari, 2006; Nordelfof et al., 2016; Nordelöf et al., 2019a; Norgate et al., 2007; van der Voet et al., 2013)

Material	MJ/kg	Reference
Electrical Steel	27	UNEP 2013, Nawaz 2006, McHenry 2014
Other Steel	23	Norgate 2007
Cast Iron	20	Norgate 2007
Aluminum	211	Norgate 2007
Copper	60	UNEP 2013
Insulation Material	84	Nordelof 2016
Impregnation Resin	23	Nordelof 2016, Calculated
Paint	20	Nordelof 2016, p.65, table 68
Packing Material	13	Li, 2019
Plastic	84	Englebeen, 2007
Electronics	32	Nordelof 2019, Calculated

A.5.6 Case Study

Thus, by estimating motor mass using an equation from Section A.5.3, selecting an appropriate material composition from Table A.4, the energy consumption to manufacture a motor can be estimated usingTable A.5.

An example using a 0.124 kW (⅙ HP) IM motor is used for demonstration here, with a length of 37.78 cm (14.875 in) the mass is estimated using Eq. (A.13) to be 14.25 kg. The energy used to manufacture the motor is estimated in Table A.6. An average of 810 MJ can be used to estimate the total energy to produce the motor from the different reference models. Similar examples can be carried out for a ¼ HP and a ⅛, HP pump motors, as can be seen summarized in Table A.7.

Table A.6: Energy (MJ) to produce a ⅙ hp pump motor

Source	Muller 2004	Ferreira 2011	Ferreira 2011	Andrada 2012	Andrada 2012
Motor Type	IM	IM	IM	Eff3 IM	Eff1/IE2 IM
Material	MJ	MJ	MJ	MJ	MJ
Electrical Steel	154.60	151.35	164.46	153.81	163.40
Other Steel	32.78	35.66	36.81	36.28	27.72
Cast Iron	91.22	51.68	43.81		
Aluminum		370.76	319.95	783.18	776.14
Copper	76.97	76.90	64.70	78.14	85.69
Insulation Material	107.76	4.34	2.83	4.25	4.10
Impregnation Resin		7.19	3.91	7.38	7.11
Paint		2.08	1.70	0.88	0.84
Packing Material		13.73	20.14	14.42	13.88
Plastic				23.70	22.82
Electronics				6.78	6.53
Total Energy	463	714	658	1109	1108

Table A.7: Parameters and Energy to produce three fractional horsepower pump motors

	hp	kW	C Dim. (in)	kg	MJ
Graymills (1/4 hp)	0.25	0.19	14.875	15.36	873
Graymills (1/6 hp)	0.17	0.12	14.875	14.25	810
Flair (1/8 hp)	0.13	0.09	11.75	6.61	458

With the stand made of steel and weighting 377.5 kg, the energy to produce the stand is estimated to be 8682 MJ. A comparison is now made between replacing the three fractional horsepower motors with a stand, as seen in Figure A.16. This compares running the pump motors either continuously or on eight-hour workdays five days per week. Pump energy is estimated using the kilowattage size of the motor, and the breakeven time is calculated by first taking the difference between the energy to manufacture the stand and the pump, and then dividing the difference by the wattage of the motors. Motor efficiency was estimated to be 82.5% using Figure A.15, and are assumed to be standard and operate at 50% load. In this example, a breakeven point can be made either under 2 years or after nearly 12 years and is influence by both the operating schedule and pump size.

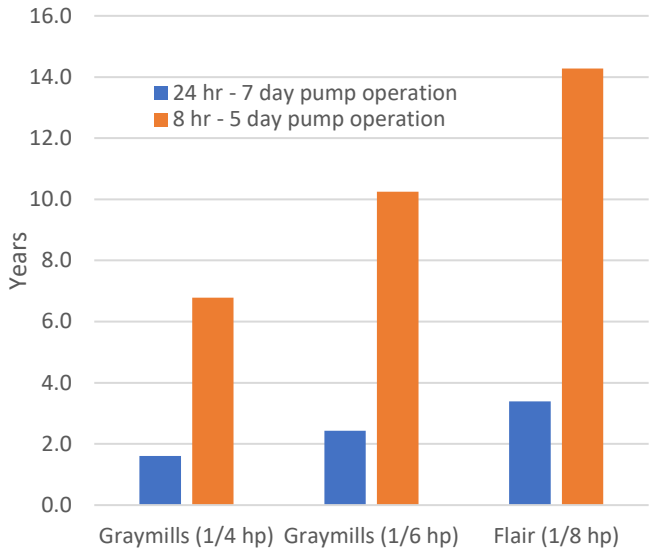

Figure A.16: Breakeven Energy comparison for replacing either A ¼, ⅙, or ⅛ HP fractional horsepower motor with a steel stand; comparison includes manufacturing and operation of each motor and stand.

A.6 Conclusion

A Stand for a grinding machine tool was designed to raise the machine to replace a coolant pump to reduce the energy consumption of the machine. A static and dynamics analysis was performed on the stand to ensure structural load capabilities and minimal vibrational response within possible operating regions. An energy analysis was undertaken for the life cycle of both a pump motor and the machine tool stand to find the energy payback period. Depending on the operating schedule, and size of the pump, replacement could be highly beneficial to reduce energy consumption.

A.7 Acknowledgements

We thank Prof. Christopher Brown at Worcester Polytechnic Institute for donating the Hahn grinding machine to us. We thank Dr. Robert Hahn for his insight into the design of this machine. We thank John Ryan of Atlas Copco for his insight into machine tool design